![Skoltech logo](Skoltech - Skolkovo Institute of Science and Technology)

Thesis Changes Log

Name of Candidate: Anastasiia Merdalimova

PhD Program: Physics

Title of Thesis: Optical sensors based on hollow-core microstructured optical waveguides: 2-in-1 multispectral refractometry and raman spectroscopy

Supervisor: Professor Dmitry Gorin
Co-supervisor: Associate Professor Alexey Yashchenok

The thesis document includes the following changes in answer to the external review process.

Dear Jury Members,

I thank you for your valuable questions. I am pleased to report that I have addressed the queries, please find the responses below. In the enclosed revised version of the thesis, the amendments are marked in yellow.

Yours sincerely,
Anastasiia Merdalimova

Professor Vassili Fedotov:

A list of minor issues to be addressed is attached.

Response: The text with corrections in yellow is presented in the end of the present file, in the renewed thesis manuscript. Also, here are the responses to correction proposals that couldn't be implemented:

Page 1. "Perhaps, it is still be possible to slip the word "towards" in the title, so that it reads "towards 2-in-1 multispectral...". Such a title would reflect what you achieved in a more accurate and less conflicting way, since what you really report in your thesis is a proof-of-concept demonstration... see my other comment further in the text (page 22)."

Response: I agree with you, this would be a perfect title. However, I asked the PhD Office, they responded that it's not possible to change the thesis title after the defence presentation. Anyway, I will take into account the idea with "towards", if one day I need to give name to analogous proof-of-concept demonstrations.

Page 52. "The core of this MOW fibre does not look hollow..."

Response: Now the elaboration is added to 3.2:

"It is worth noting that the core and cladding holes on SEM images in Figure 3-1 possess different intensities. For the left image, The waveguide was mounted vertically. the lighter zone in the center is due to possibility to register secondary electrons emitted by inner walls forming the core capillary. The surrounding cladding capillaries possess much smaller diameter, thus the probability of the electron showing up from them is smaller, hence these cladding capillaries look like darker. The picture on the right shows enlarged image of the side capillaries. To obtain such image, the HC-MOW was tilted by a certain angle, which was enough to eliminate the electrons from the core walls. Therefore, the contrast between hollow zones in the core and cladding capillaries is reduced compared to the left image.

Professor Zeev Zalevsky

1. To better explain the connection between the different chapters;

Response: The corresponding paragraph in the Introduction is enlarged:

"As was mentioned above, the extracellular vesicles are chosen because of their potential to substantially enhance diagnostic approaches. Meanwhile, protein-copolymer complexes and microbubbles made of them are, on the one hand, models of biological solutions, and, on the other hand, the microbubbles are used as ultrasound contrast agents and may benefit from a robust way of their real-time characterization. Furthermore, starting with protein-copolymer complexes instead of extracellular vesicles is practical because obtaining extracellular vesicles is a laborious process: it requires harvesting large amounts of cells *in vitro* or obtaining samples of human biological fluids, followed by a laborious vesicle isolation process. In contrast, the protein BSA is cheap and readily available, and the copolymer used is easy to synthesize. In addition, these protein-copolymer complexes have rich Raman spectra, which is similar to extracellular vesicles, but with higher peak intensities. This makes protein-polymer complexes ideal model analytes for testing and evaluating sensing techniques before applying them to extracellular vesicles."

2. To compute the number of modes excited in the fiber and to explain how it affects the sensitivity of the measurement.

Response: now this information is added to the end of subsection 3.3.1:

"In aspect of mode composition, the HC-MOW used (with a comparatively large hole diameter 240 um, which is important here) may be described as a hollow glass tube[158]. The wave propagation

in this tube is carried out through Bragg reflection from the first wall: the reflection of a single wave at the inner and outer surfaces of the wall and their constructive interference; the other walls do not play a role. The obtained modes in hollow-core waveguides are intrinsically leaky, i.e. they continuously dissipate energy along the transverse direction[159,160,158], and the modal losses scale with the inverse fourth power of core radius[158]. The number of these leaky modes is extremely large. Knowing the number of propagation modes plays an important role for telecommunication fibers of kilometers length, because it largely determines the loss and distortion of the signal: the fundamental mode drops with higher orders due to bends. In hollow-core fibers, in the vicinity of the light input tip, a large number of modes are spread, but losses for high-order modes are high, thus they leak rather quickly (in a few meters)[161]. However, in the present work the waveguide length is just 6 cm. There, it is usually spoken of mode discrimination, i.e. several lower order modes are selected and their losses relative to each other are evaluated, as demonstrated by Zeisberger and Schmidt [158]. The mode with significantly lower losses than the others survives. Technically, the number of supported modes may be calculated from the hollow tube dispersion, which is a standard approximation for hollow fibers of this type.

According to Zheltikov[13],the approximate attenuation coefficient for the mode of the m-th order is

$$\alpha_m \approx \frac{1}{\sqrt{n_2^2 - n_1^2}} \frac{(\lambda m)^2}{d_{core}^3 n_1}, \quad (3\text{-}2)$$

Where dcore is the core diameter.

According to the Equation (3-2), to deplete modes higher than m-th order, the waveguide length L may be chosen considering characteristic attenuation lengths for m and (m+1)th order modes:

$$\frac{1}{\alpha_{m+1}} < L < \frac{1}{\alpha_m}, \quad (3\text{-}3)$$

For the HC-MOW used in the present work, L = 6 cm, d_{core} = 250 um, n_1 = 1 (for air-filled HC-MOW), $n_2 \approx$ 1.45 um. Then, for instance, at λ = 500 nm modes up to 30th order are transmitted without significant losses.

It's always important to excite a fundamental mode with minimum losses, thus the optical beam centering in the core plays a crucial role [162]. Therefore, the objectives in the measurement setup (will be described in the next subsection) are mounted in 3-coordinate stages, and the efficiency of free-space light coupling to the waveguide is provided by maximization of the intensity observed by the spectrometer."

Dr. Dana Cialla-May:

In comparison of Raman and SERS spectra of R6G, the orientation of the molecule towards the metallic surface should be addressed (i.e. surface selection rules).

Response: now the Section 5.2 is enlarged, and in particular surface selection rules are considered:

"According to surface selection rules, molecule vibrations with transition dipoles (and hence bonds) directed tangentially to the metal surface should have decreased amplitude; meanwhile, molecule vibrations with transition dipoles directed perpendicular to the metal surface should have augmented amplitude [194]. On both SERS substrates, the peak at 773 1/cm possesses relatively low SERS enhancement. This peak belongs to out-of-plane (the only one among the observed peaks) bending and methyl group [195]. R6G molecule contains nitrogen, and gold-nitrogen bonding is strong [196], thus the author assumes that the R6G molecule binds to gold surface via nitrogen in such a way that the methyl groups turn to be having a less angle with the gold surface than the xanthene plane."

Professor Nikolay Gippius:

Minor revisions are required following the questions during the discussion.

Response: the questions postulated by the Jury Members are answered above, and the full text with the corrections is provided below.

"

Skoltech

Skolkovo Institute of Science and Technology

Skolkovo Institute of Science and Technology

OPTICAL SENSORS BASED ON

HOLLOW-CORE MICROSTRUCTURED OPTICAL WAVEGUIDES:

2-IN-1 MULTISPECTRAL REFRACTOMETRY AND RAMAN SPECTROSCOPY

Doctoral Thesis

by

ANASTASIIA MERDALIMOVA

DOCTORAL PROGRAM IN PHYSICS

Supervisor

Professor Dmitry Gorin

Co-supervisor

Associate Professor Alexey Yashchenok

Moscow - 2023

I hereby declare that the work presented in this thesis was carried out by myself at Skolkovo Institute of Science and Technology, Moscow, except where due acknowledgement is made, and has not been submitted for any other degree.

Anastasiia Merdalimova (Candidate)

Prof. Dmitry Gorin (Supervisor)

Abstract

Early diagnosis of diseases (such as cancer) based on the analysis of biological fluids is one of the most prioritized topics in modern biomedical research, as it enables a better prognosis for patients. Several objects can be chosen as biomarkers for early diagnosis, such as specific proteins and circulating tumor DNA, circulating tumor cells or the recently discovered extracellular vesicles. Extracellular vesicles are nanosized capsules with a lipid bilayer, which contain proteins and nucleic acids, released by cells and may be found in diverse biological fluids. The disease-specific extracellular vesicles appear in a bloodstream earlier and in higher concentrations than circulating tumor cells, and can provide more multifaceted information about the parental cell than single molecules. Thus, extracellular vesicles are promising biomarkers for early diagnosis.

However, the utilization of extracellular vesicles requires instrumentation for their isolation from biological fluids, and then detection and/or analysis. For that, their complex structure becomes a disadvantage, raising a need for a sensor capable of handling objects of such a type.

Thus, a way towards early diagnosis proposed in this project involves measuring two parameters of extracellular vesicles: the refractive index of their solution as a means of detecting their presence, and Raman spectroscopy for analyzing them as biomarkers.

Both refractometry and Raman spectroscopy may be performed in a convenient way with the help of hollow-core microstructured optical waveguide (HC-MOW). Therefore, the goal of the present project is to explore the opportunities of using a HC-MOW for multifaceted characterization of complex fluids. In particular, the examples of such fluids used in the work are macromolecule structures as model analytes and extracellular vesicles.

HC-MOW features a unique optical structure for light waveguiding, which can be used as a multiwavelength refractive index sensor and Raman scattering sensor.

Previously, those sensing modalities were explored separately, and the goal of the present project has been reached by combining them in a single HC-MOW. Namely, that was done in the following ways: SERS substrate fabrication and the corresponding layer

3

deposition control in HC-MOW; and 2-in-1 multispectral refractometry and Raman spectroscopy for complex macromolecular objects, namely protein-copolymer complexes and microbubbles and, finally, extracellular vesicles.

First, we demonstrate that the use of a 2.5 cm long HC-MOW show markedly improved performance in Raman signal measurements when compared to analyte on a flat surface (2 µL drop), resulting in amplitude enhancement ac. 50 times for R6G and 2.3 times for BSA. Then this fiber-enhanced Raman was combined with other sensing techniques. The first of those was building a SERS substrate in the HC-MOW, providing SERS sensing with additional 10 times amplitude enhancement and layer deposition control during fabrication. However, the developed SERS sensing in HC-MOW didn't demonstrate a significant enhancement compared to previously reported values and turned out to be unstable in liquid solution.

Therefore, the investigation of HC-MOW for multifaceted characterization moved to 2-in-1 multispectral refractometry and Raman spectroscopy. The term "two-in-one" is used to indicate that the approach can be achieved with a single setup.

Tested on BSA and P(VP-AA) aquaeous solitions, refractive index and Raman peak intensities demonstrated linear dependence on analyte concentration on a given range of concentrations used (5-100 mg/mL). The sensitivities of up to $2.9 \cdot 10^8$ RIU·mL/mg for RI and 6.4 arb.u.·mL/mg for Raman spectroscopy of BSA solutions were estimated. Then the approach was transferred to BSA-P(VP-AA) colloidal structures, namely nano-sized complexes and micro-sized bubbles. For microbubbles, as they are highly scattering, an upper detection limit was found, $4 \cdot 10^8$ microbubbles per mL.

These findings pave a way towards possibility of using HC-MOW for biological fluids for diagnostic needs. Moreover, it can be used for the characterization of ultrasound contrast agents in real-time, specifically of protein-copolymer microbubbles and their parent complexes.

Publications

Research articles

1. **A.A. Merdalimova**, P.G. Rudakovskaya, T.I. Ermatov, A.S. Smirnov, S.S. Kosolobov, J.S.Skibina, P.A. Demina, B.N. Khlebtsov, A.M. Yashchenok, D.A. Gorin, SERS Platform Based on Hollow-Core Microstructured Optical Waveguide: Technology of UV-Mediated Gold Nanoparticle Growth. Biosensors, 2022, 12, 19. https://doi.org/10.3390/bios12010019 (IF=5.519, Q1)
   Author's contribution: Research methodology, providing measurements, data analysis, manuscript writing

2. J. Cvjetinovic, **A. A. Merdalimova**, M. A. Kirsanova, P. A. Somov, D. V. Nozdriukhin, A. I. Salimon, A. M. Korsunsky and D. A. Gorin, A SERS platform based on diatomite modified by gold nanoparticles using a combination of layer-by-layer assembly and a freezing-induced loading method. Phys. Chem. Chem. Phys., 2022,24, 8901-8912. https://doi.org/10.1039/d2cp00647b (IF 3.7, Q1)
   Author's contribution: SERS spectroscopy, writing corresponding chapters

3. M.A. Slyusarenko, N.S. Nikiforova, E. I. Sidina, I.V. Nazarova, V.V. Egorov, Y.P. Garmay, **A.A. Merdalimova**, N.P. Yevlampieva, D.A. Gorin, A.V. Malek, Formation and evaluation of a two-phase polymer system in human plasma as a method for extracellular nanovesicle isolation. Polymers (Basel), 2021, 13(3):1–16. https://doi.org/10.3390/polym13030458 (IF=3.426, Q1)
   Author's contribution: Raman spectroscopy, nanoparticle tracking analysis, writing a corresponding paragraph

4. V.Chernyshev, R.Chuprov-Netochin, E.Tsydenzhapova, E.Svirshchevskaya, R.Poltavtseva, **A.Merdalimova**, A.Yashchenok, A.Keshelava, K.Sorokin, V.Keshelava, G.Sukhikh, D.Gorin, S.Leonov, M.Skliar. Asymmetric depth-filtration: A versatile and scalable method forhigh-yield isolation of extracellular vesicles with low contamination. Journal of Extracellular Vesicles, 11, e12256. https://doi.org/10.1002/jev2.12256 (IF 17.3, Q1)
   Author's contribution: Raman spectroscopy, writing a corresponding paragraph

5. **A. Merdalimova**, V. Vorobev, R. Barmin, A.Aleksandrov, D. Terentyeva, T. Estifeeva, S. German, V. Chernyshev, O. Maslov, Y. Skibina, P.Rudakovskaya, D. Gorin, Two-in-One Sensor of Refractive Index and Raman Scattering using Hollow−Core Microstructured Optical Fibers for Colloid Characterization. Colloids and Surfaces B, 2023 (IF 5.8, Q1) Accepted, submission number COLSUB-D-23-02310)
Author's contribution: Research methodology, providing measurements – Raman spectroscopy and refractive index sensing, data analysis, manuscript writing

Review article & book chapter

1. **A.A. Merdalimova**, V.V. Chernyshev, D. Nozdriukhin, P. Rudakovskaya, D. Gorin, A. Yashchenok, Identification and Analysis of Exosomes by Surface-Enhanced Raman Spectroscopy. Applied Sciences-Basel, 9,6,2019, 1135. https://doi.org/10.3390/app9061135 (IF=2.217, Q2)

2. **A. Merdalimova**, V. Vorobev, A. Zanishevskaya, S.Perevoschikov, A.Aleksandrov, P.Rudakovskaya, Y. Skibina, V. Tuchin, D. Gorin, Hollow-core microstructured optical fibers and their applications for biosensing. A chapter in a book "Specialty Optical Fibers", Elsevier, 2023 (under revision)

Patent

1. A. Yashchenok, V. Chernyshev, P. Rudakovskaya, **A. Merdalimova**, V. Shipunova, A. Schulga, S.Deev, D. Gorin. Nano- and microparticles for isolation of specific exosome subpopulations and their analysis. № RU2733884

Participation in scientific conferences

1. <u>**A.Merdalimova**</u>, A.Yashchenok, D.Gorin, "Application of Raman spectroscopy to exosomes: approaches and challenges", European Biosensor Symposium - Digital Seminar Series: Seminar on Raman-based Biosensors, headed by Leibniz Institute of Photonic Technology Jena, Germany, 2021 (oral talk)

2. **<u>A.Merdalimova</u>**, V.Chernyshev, R.Chuprov-Netochin, D.Gorin, "In vitro study of exosome secretion rate by nanoparticle tracking analysis", "Saratov Fall Meeting-2020" - VIII Symposium on Optics & Biophotonics, 2020 (oral talk)

3. **A. Merdalimova**, R. Barmin, V. Vorobev, D. Terentyeva, T. Estifeeva, S. German, V. Chernyshev, O. Maslov, Y. Skibina, P.Rudakovskaya, D. Gorin, Optical Sensors Based on Hollow-Core Microstructured Optical Waveguides, 17th
International conference on Laser Applications in Life Sciences, 2023 (oral talk) – October 15-17th 2023

4. **A. Merdalimova**, R. Barmin, V. Vorobev, D. Terentyeva, T. Estifeeva, S. German, V. Chernyshev, O. Maslov, Y. Skibina, P.Rudakovskaya, D. Gorin, Two-in-One Optical Sensors Based on Hollow-Core Microstructured Optical Waveguides, Dianov's All-Rusian Conference on Fiber Optics 2023 (oral talk) –October 3-6th 2023

Acknowledgements

Table of Contents

List of Abbreviations

AA – acrylic acid

AIBN – 2,2′–azobis (2–methyl propionitrile)

arb.u. – arbitrary units

ARF – Antiresonant Fiber

ARROW - Antiresonant Reflecting Optical Waveguide

AuNP, GNP – Gold Nanoparticles

BBB – Blood-Brain Barrier

BSA – Bovine Serum Albumin

CTC – Circulating Tumor Cells

cfDNA – Cell-Free DNA

ctDNA – Circulating Tumor DNA

DEX - Dextran

DF – Depth Filtration

DNA – Deoxyribonucleic Acid

EF – Enhancement Factor

ENV – Extracellular Nanovesicles

EV – Extracellular Vesicles

HC-MOW – Hollow-Core Microstructured Optical Waveguide

LbL – Layer-by-Layer

LOD – Limit of Detection

LP – Lower Phase

LSPRs - Localized Surface Plasmon Resonances

MB – Microbubble

NP – Nanoparticles

NVP – N–vinyl–2–pyrrolidone

ODT – 1–octadecanethiol

RI – Refractive Index

SEM – Scanning Electron Microscopy

SERS – Surface-Enhanced Raman Scattering

PBG – Photonic Bandgap

PC – Photonic Crystal

PCA – Principal Component Analysis

PCF – Photonic Crystal Fiber

PE – Polyelectrolytes

PEi – Polyethyleneimine

PVP - poly(N−vinylpyrrolidone)

P(VP-AA) − copolymer of poly (N−vinylpyrrolidone−*co*−acrylic acid)

R6G – Rhodamine 6G

TEM – Transmission Electron Microscopy

THPC – Tetrakis-(Hydroxymethyl)-Phosphonium Chloride

UP – Upper Phase

List of Figures

List of Tables

Chapter 1. Introduction

This chapter serves as an introduction to the main fields that intersect with the present thesis, providing a concise background. It highlights the motivation and novelty of the work and reviews the project's goals and associated tasks. Additionally, the chapter elucidates the significance of all subsequent chapters in the context of the overall research endeavor.

Diagnostics at the early stages of diseases, especially cancer, is an important area of research in biomedicine. Biomarkers in biological fluids, such as proteins, circulating tumor cells, and extracellular vesicles (EV) have been investigated as potential indicators for early disease detection[1,2]. Discovered only a few decades ago, EVs are nano-sized structures secreted by all or nearly all mammalian cells. EV are surrounded by a lipid bilayer and contain proteins on their surface and inside; some EV also contain nucleic acids inside. These proteins and nucleic acids provide valuable information about the parent cells EV are released by cells into various biological fluids and can therefore be captured in a liquid biopsy probe and used as biomarkers. [3–6]. Compared to circulating tumor cells, disease-specific EVs appear earlier and at higher concentrations, which makes them promising candidates for early diagnosis[7]. However, given the intricacies of their complex structure, the effective utilization of EVs for diagnostic purposes requires proper instrumentation for their isolation, detection, and analysis[8,9]. Multimodal sensing for multifaceted liquid object characterization may be beneficial not only for EV, but also for other biological objects and complex synthesized structures.

Hollow-core microstructured optical waveguides (HC-MOW) could serve as a framework for such a sensor potentially offering multimodal sensing. HC-MOW [10] are axis-symmetrical structures providing waveguiding via either photonic bandgap or inhibited coupling effect, depending on inner wall thickness[11,12]. The scope of interest in the present work is in the inhibited-coupling HC-MOW. Due to the provided light guiding as in the Fabri-Perot resonator[13], these waveguides may be used in a number of sensing modalities, as shown in Figure 1-1: for multiwavelength refractive index [14], absorption on inner walls[14,15], Raman[16–18] and SERS (Surface-Enhanced Raman

Scattering)[15,19,20] sensing. A number of HC-MOW applications in sensing are known, including sensing of biological objects[21–23], inter alia extracellular vesicles[24].
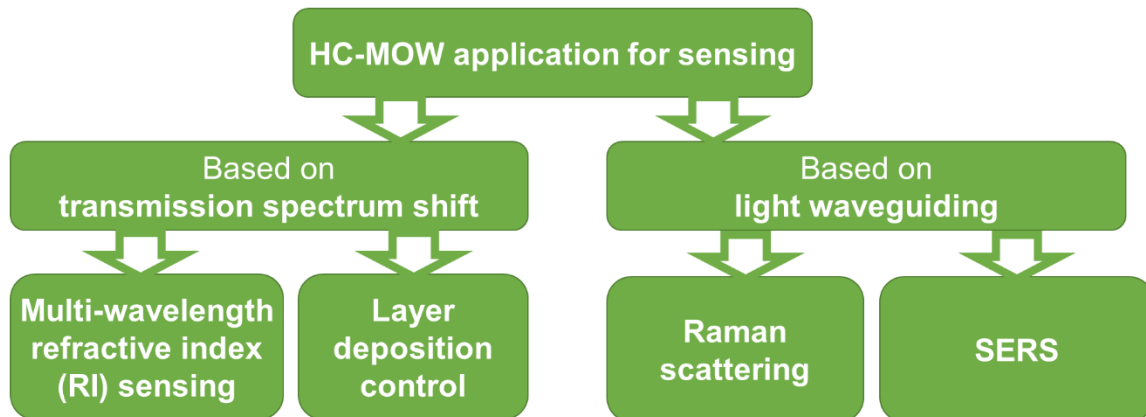
Figure 1-1. Hollow-core microstructured optical waveguides (HC-MOW)
applications for sensing considered in the present work

Previously, the exploitation of these sensing modalities used to be separate. The aim of the present thesis is a proof-of-concept demonstration of 2-in-1 sensing in HC-MOW for multifaceted characterization of complex fluids via combining various sensing modalities.

The novelty of the present research is the following: in order to analyze complex liquid analytes, it is suggested to combine several sensing modalities in HC-MOW in the following two ways:

(i)   SERS substrate fabrication and the corresponding layer deposition control in HC-MOW;

(ii)   two-in-one multispectral refractometry and Raman spectroscopy for complex macromolecular objects, specifically protein-copolymer complexes/microbubbles and extracellular vesicles.

The combination of multispectral refractometry and Raman spectroscopy is referred to as "two-in-one" because it is possible to realize both types of sensing in a single setup. Realizing the two types of sensing in a single setup is merely a technical issue, which will

22

be addressed in future. Still, the term "two-in-one" is used to clarify that the approach can be achieved on a single setup.

As was mentioned above, the extracellular vesicles are chosen because of their potential to substantially enhance diagnostic approaches. Meanwhile, protein-copolymer complexes and microbubbles made of them are, on the one hand, models of biological solutions, and, on the other hand, the microbubbles are used as ultrasound contrast agents and may benefit from a robust way of their real-time characterization. Furthermore, starting with protein-copolymer complexes instead of extracellular vesicles is practical because obtaining extracellular vesicles is a laborious process: it requires harvesting large amounts of cells in vitro or obtaining samples of human biological fluids, followed by a laborious vesicle isolation process. In contrast, the protein BSA is cheap and readily available, and the copolymer used is easy to synthesize. In addition, these protein-copolymer complexes have rich Raman spectra, which is similar to extracellular vesicles, but with higher peak intensities. This makes protein-polymer complexes ideal model analytes for testing and evaluating sensing techniques before applying them to extracellular vesicles.

Thus, the potential of HC−MOW for diagnostic needs is estimated.

Therefore, the project tasks are as follows:

1) To estimate the applicability of the HC-MOW for improved Raman spectroscopy;

2) To implement SERS in HC-MOW, combining the Raman sensing capabilities with layer deposition control;

3) To estimate 2-in-1 refractive index and Raman sensing capabilities for colloidal solutions, namely aquaeous solutions of protein-copolymer complexes and microbubbles (MB);

4) To facilitate the isolation of extracellular vesicles using Raman spectroscopy;

5) To apply the developed 2-in-1 refractive index and Raman sensing for sensing extracellular vesicles.

This set of tasks leads to the following structure of the thesis: Chapter 2 provides literature review on HC-MOW, their current and possible future applications. It also identifies the gap in using HC-MOW for extracellular vesicles sensing. The following chapters are experimental. Chapter 3 describes the methods used in the work. Analytical methods used for sensing in the present work and particular analytes they were applied to are schematically summarized in Figure 1-2. Chapter 4 provides the results of the investigation of Raman scattering in HC-MOW, which benefits from light confinement and waveguiding, resulting in fiber-enhanced Raman spectroscopy (FERS). Raman scattering was initially explored in the case of bulk media, such as solutions of Raman-active dye Rhodamine 6G (R6G) and protein BSA, to demonstrate FERS and compare sensor performance across disparate liquids. Drawing from the results of Chapter 4, the two avenues for combined sensing modalities in HC-MOW are considered. The first is detailed in Chapter 5, which describes the development of SERS substrate in HC-MOW, benefiting both from fiber enhancement and the capability to control layer deposition. The second avenue is considered in Chapter 6 and Chapter 7, which detail two-in-one sensing of multispectral refractive index and Raman scattering of liquids in HC-MOW[25], that is of interest for multicomponent systems with complex spectra. Chapter 6 demonstrates the 2-in-1 sensing of protein-copolymer complexes. Chapter 7 is dedicated to EV, with section

7.1 describing Raman spectroscopy application for extracellular vesicles isolation, while section 7.2 reports the previously introduced 2-in-1 sensing for EV.

Figure 1-2. Combinations of analytical methods and analytes used in the experimental part of the present work
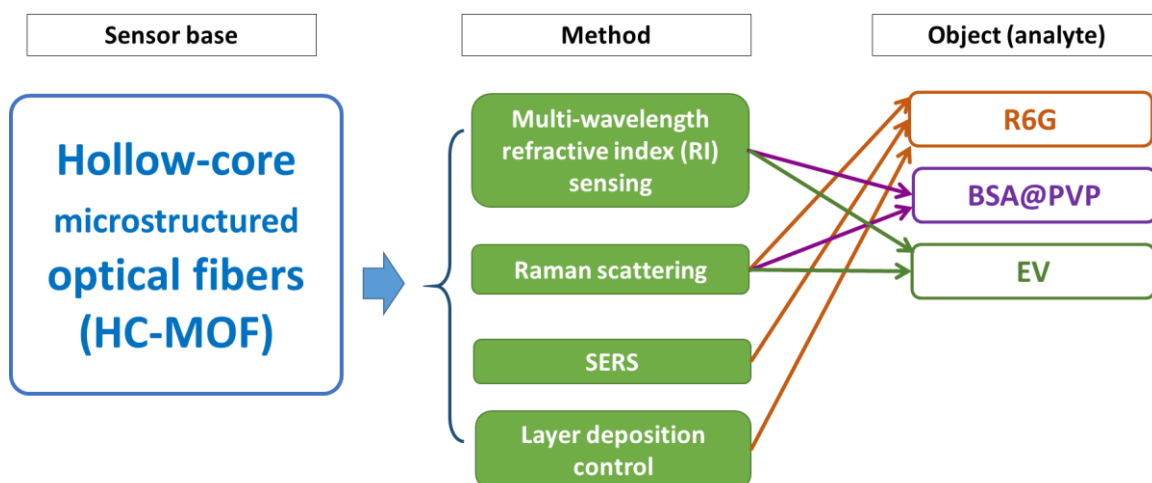
Chapter 2. Literature review

In this Chapter, the background and recent developments of the topics covered by the present thesis are provided. As a conclusion, the problem and the proposed methods of its solution are identified.

2.1. Hollow-core microstructured optical waveguides (HC-MOW)

2.1.1. HC-MOW working principle and classification

Microstructured optical waveguides (MOWs) is a novel class of optical fibers developed in the 1990s. Here, the light is guided through a complex microstructure, which in most cases contains air channels running along the entire waveguide length [26]. According to the structural architecture, MOWs may be classified as solid-core (SC) and hollow-core (HC) MOW. Light guiding in a core of a SC-MOW can be based on conventional total internal reflection, if the core possesses a refractive index (RI) greater than cladding structure. But it is not the case for HC-MOWs, where the core is filled with air, other gas or liquid, which implies a refractive index typically lower than surrounding glass. The propagation of light in the core of HC-MOW depends on the modes allowed in the cladding. These modes in their turn in fact depend on the thickness of the first inner wall and inner structure periodicity. Thus, for walls with thickness up to 150 nm, the mechanism is photonic bandgap (PBG) guiding; otherwise, with greater wall thickness, the mechanism is inhibited coupling (IC) guiding [12,27]. IC waveguides are also referred to as broadband, or anti-resonant waveguides (or anti-resonant fibers, ARF, if applicable). According to their geometrical structure, ARF include, in order of development and optimization: Kagome, negative curvature, single-ring revolver waveguide, conjoined-tube and nested anti-resonant nodeless waveguides [12,21]. Also, chirped HC-MOWs were presented, whose cladding microstructure is formed by several layers of holes, with a certain geometrical arrangement: depending on the wavelength, light experiences reflection in different resonant sections of the cladding. This enables effective localization

of reflection to a particular layer of the structure and thus sharp resonances are removed from multiply resonant single-cell-sized structures[28,29].

Light propagation in photonic crystal fibers can be illustrated by a dispersion (propagation) diagram built on a numeric solution of Maxwell's equations, presented in Figure 2-1 [30]. In this diagram, axes are the dimensionless quantities $\beta\Lambda$ (normalized wave vector along fiber) and $\omega\Lambda/c$ (normalized frequency), where β is an axial wave vector component, Λ is the interhole spacing, ω is light frequency and c is the speed of light in vacuum.
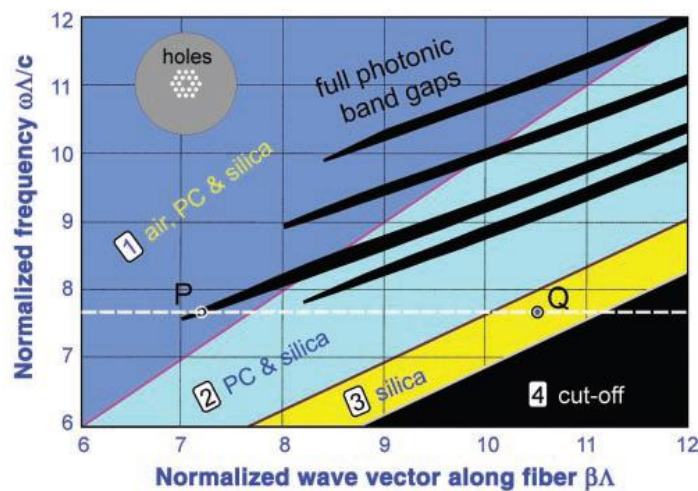
Figure 2-1. Dispersion diagram for a triangular lattice of air channels in silica glass with 45% air-filling fraction, forming a photonic crystal fiber (PCF). In region (1), light is free to propagate in every region of the fiber (air, photonic crystal (PC), and silica). In region (2), propagation is turned off in the air, and, in (3), it is turned off in the air and the PC. In (4), light is evanescent in every region. The black fingers represent the regions where full two-dimensional photonic band gaps exist. Guided modes of a solid-core PCF (see schematic in the top left-hand corner) form at points such as Q, where light is free to travel in the core but unable to penetrate the PC. At point P, light is free to propagate in air but blocked from penetrating the cladding by the photonic bandgap (PBG); these are the conditions required for a hollow-core mode. From P. Russel, 2003 [30]. Reprinted with permission from AAAS.

The diagram in Figure 2-1 shows the ranges of the frequency and axial wave vector components, where light is unable to propagate, or evanescent. When keeping optical frequency constant, the maximum possible value of β is determined by $kn = \omega n/c$, where n is the refractive index of the region under consideration. Light is free to propagate when $\beta < kn$, and is evanescent when $\beta > kn$. For photonic crystal fibers, this diagram represents a band-edge or "finger" plot. In black regions, light is evanescent, including the regions with $\beta < k$ (free light propagation in vacuum), that provides a theoretical foundation for light guidance in a silica-air structure.

Below the working principles for the mentioned above subtypes of hollow-core fibers, namely PBG and AR waveguides, are briefly discussed. They are also illustrated and compared by their modal content in Figure 2-2.
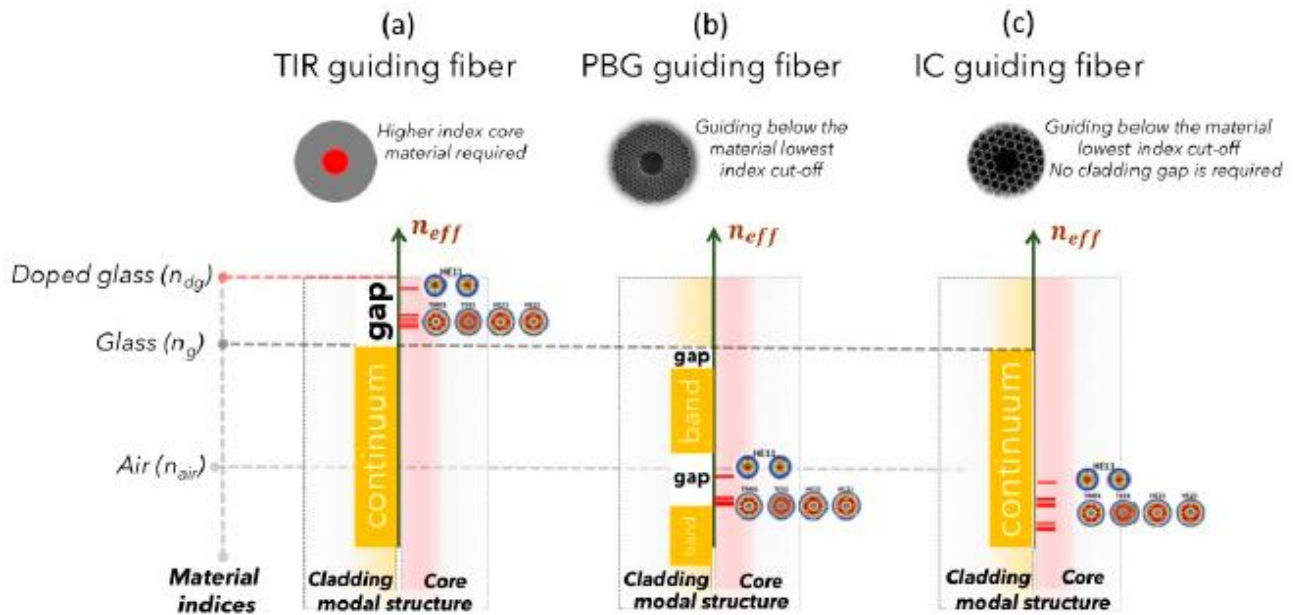
Figure 2-2. Modal content representation of optical waveguide with different guiding mechanisms: (a) total internal reflection; (b) photonic bandgap; (c) antiresonant, or inhibited coupling waveguide. Reproduced from Debord et al.[27]

Photonic bandgap (PBG) waveguide working principle

In the case of PBG, the cladding walls are thin enough (50-150 nm) and not to support modes for a certain range of wavelengths and propagation constants. For those ranges light in the core is unable to couple to cladding modes and can be guided in the core with low losses [31]. To get a PBG HC-MOW, the core geometry and refractive index must be chosen such that at least some of its supported modes are not allowed to propagate in the cladding; in this case, the core modes cannot leak out because there is no cladding mode to couple to [27]. After filling the PBG waveguide with an analyte, the bandgap position shift takes place, with a new wavelength of the bandgap determined by [32]:

$$\lambda' = \lambda_0 \sqrt{\frac{1 - \left(\frac{n_2'}{n_1}\right)^2}{1 - \left(\frac{n_2}{n_1}\right)^2}} \quad , \tag{2-1}$$

where λ_0 is an initial wavelength of the bandgap, n_2 and n_2' are refractive indices of low index (hollow) areas before and after filling, n_1 is refractive index of the walls. Figure 2-3 presents the transmitted power of a broadband supercontinuum light source after passing the PBG waveguide is presented.

However, to provide a broadened PBG transmission, the holes may be filled selectively: the hollow core is filled with a liquid, meanwhile hollow capillaries in the cladding remain air-filled[16]. Such filling configuration is called liquid-core waveguide.

Inhibited coupling waveguide work principle

When inhibited coupling is the light guiding mechanism, the antiresonant reflecting optical waveguide (ARROW) model is commonly used to analytically describe its behavior. The light propagation here is described similar to a Fabri-Perot cavity formed between parallel plates. The dependence of the minima of the transmission spectrum on wall thickness and refractive indices of the walls and core fulfillment is described further in section 3.3.
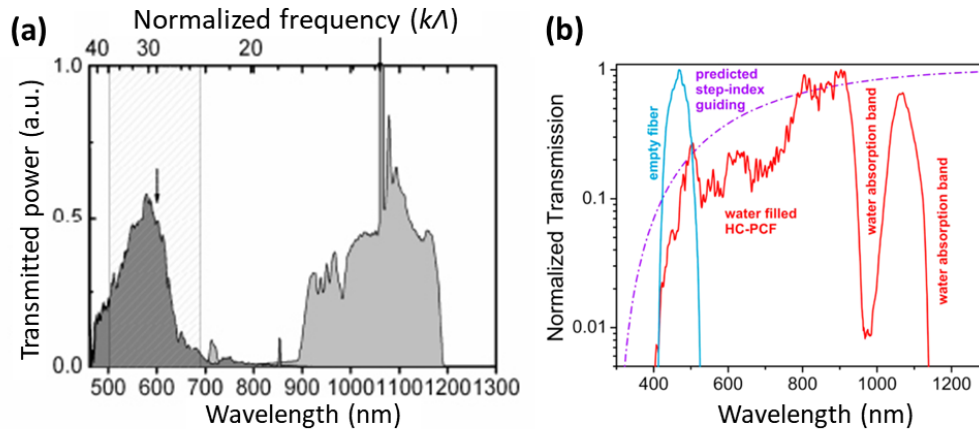
Figure 2-3. (a) Transmitted power spectra of the 1060 nm waveguide using a SC source. The spectra were taken before and after filling the holes of the PBG waveguide with liquid D2O (light and dark grey areas, respectively). The vertical lines define the location of the new shifted bandgaps as predicted by the index scaling law. The arrows mark the position of the respective transmission peaks. Reprinted with permission from [Antonopoulos 10.1364/OE.14.003000] © The Optical Society. (b) Transmission spectra of an empty and liquid-core PBG waveguide. Reprinted with permission from Yan et al. [16]. Copyright 2017 American Chemical Society.

2.1.2. HC-MOW fabrication

The previous subsection described how the spectral properties of microstructured waveguides are determined by the geometry of their cross-section, physical dimensions and material. The complexity of the waveguide geometry, the chosen material, as well as the potential field of application, determine the choice of the fabrication approach. The existing technologies for manufacturing microstructured waveguides can be divided into two classes: one-step and two-step. In the first case, the process allows obtaining a finished fiber in one step directly from the source material (rod of the selected material or melt). Such methods include mold casting, 3D printing, and direct extrusion from a die. Two-step methods involve making a waveguide preform on a macro scale in one of the possible ways and pulling the preform into the waveguide of the desired size. The most popular two-step

30

method is stack-and-draw, and this is exactly the method that was used for fabrication of the HC-MOW utilized in the present work.

In the stack-and-draw method, the capillaries and rods are stacked manually or with a computer-controlled stacking device, if the design allows it, which ensures precise alignment of the tubes and the distance between them. After stacking, this package is pulled into a macro-size preform using a heat source, such as an oven, to soften the material and create tension. A schematic representation of the drawing process is shown in Figure 2-4. As the material is drawn, the tubes fuse together to form a strong structure with air holes. The resulting preform is then re-pulled in a similar fashion to the waveguides of the desired size. This intermediate re-drawing is an important step because it helps to avoid a drastic change in scale from the capillary package to the final waveguide [33].
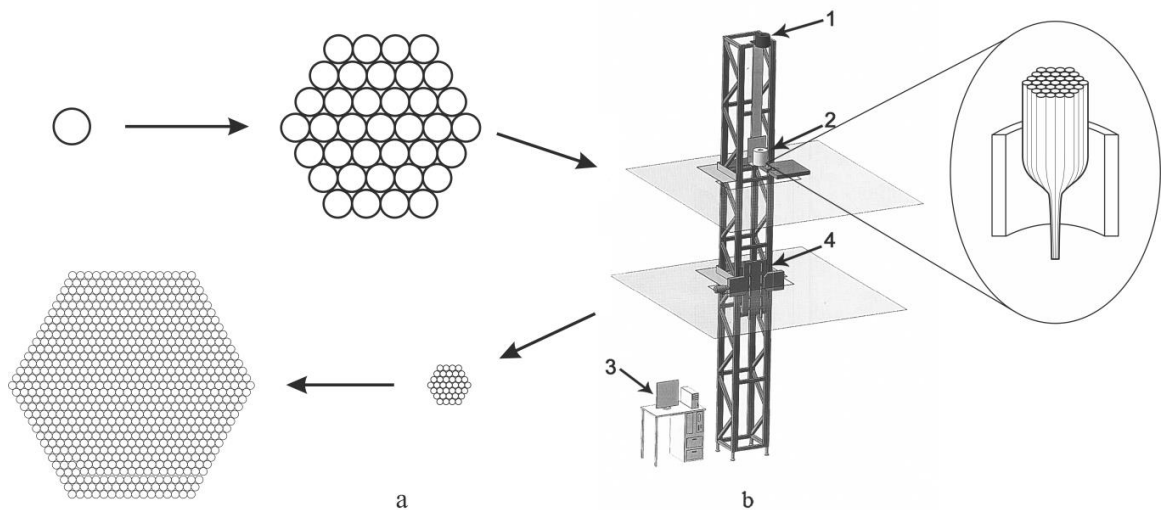
Figure 2-4. Schematic representation of the MOW manufacturing process (a) and MOW drafting unit (b): (1) billet feeding mechanism into the furnace; (2) furnace; (3) computer control; (4) drafting chain mechanism. Adapted from [29]

2.1.3. HC-MOW wall modification

The modification of the walls of MOW can achieved in the following two ways: modification of the inner capillaries and modification of the outer surface [34–38]. These types of modifications are typically achieved using the same methods. However, the

interaction of functional groups occurs either with the guided light or with the evanescent field respectively. Modification is done by attachment of small molecules, or polymers, or nanoparticles to the hollow core fiber wall. One of the main purposes of MOW modification is attachment of antibodies or reactive molecules to the glass surface. Since the majority of them do not typically adhere directly to the glass, it is essential to produce a structure on which the molecules can be bound using chemical or physical functionalization [39,40]. Some of popular methods will be described below.

One of the chemical methods for surface modification is based on electrostatic interaction, typically using charged polymers like polyelectrolytes (PE). One polyelectrolyte or a stack of oppositely charged PE may be used. The latter approach is called the Layer-by-Layer (LbL) assembly method, and it is one of the popular methods for hollow fibers modification. LbL was originally developed for the preparation of nanoscale films [41] and then was adapted for the modification of MOW [14,34,42–44]. Depositing layers of charged polymers like PE from a solution, which follows a LbL process [10,14,34,45], make a good sorption of polymers on the surface. The first PE layer is deposited with a charge that opposes the intrinsic surface charge of the substrate, then the surface is rinsed, and a subsequent PE layer with the opposite charge is deposited. The process can be repeated several times to stack layers on any substrate, resulting in an increased PE functional group density on the sensor surface. Alternatively, a volume-doped polymer layer can be deposited to both create a safeguard coating and functionalize the fiber to the target species. Therefore, LbL functionalization may be provided for a number of purposes.

In addition to chemical modification, sensor molecules can be attached to surfaces via forces other than chemical bonds, the so-called physical modification. Physical functionalization is a term used to describe attaching sensor molecules to the surface through forces other than chemical bonds. Even though physical methods are less reliant on the surface molecules, they can be employed on a broad range of substrates, including metals, polymers, carbon nanotubes, and glass [46–48].

Along with the waveguide modification with molecules, the deposition of nanoparticles opens up wide possibilities for using fibers as high-precision sensors. It can be provided by various chemical methods [49–52] . Nanoparticles adsorbed on the surface may either form self-assembling NP monolayers [53,54] or provide chaotic distribution. NP deposition is a step-by-step process, as an additional linking layer between the fiber wall and nanoparticles is needed. If all bonds present in the resulting multilayer are of chemical type, the structure is strong enough and can be broken ultimately by another chemical reaction. The linking layer may be silanes, such as (3-mercaptopropyl)trimethoxysilane (MPTMS), which ensures uniform distribution of gold or silver nanoparticles [55]. Another type of the linking layer is polyelectrolytes: their charged surface can attach nanoparticles due to electrostatic forces. Nanoparticles can be embedded in a polymer coating adsorbed on the wall and deposited using the LbL method, as was demonstrated for gold [56] and magnetite [43]. In addition to the described methods of NP deposition, the interaction between the wall and nanoparticles can be further enhanced by annealing [19].

Development of layer deposition protocol plays a crucial role in modification outcome. Therefore, the main typical protocol features are reviewed below. In most studies [34–38,42–44,49,57–64], the modification of MOW involves depositing one or more layers of various materials onto their surface. This process usually consists of the following steps, with some possible variations: Firstly, the non-modified empty waveguide is thoroughly cleaned to eliminate any potential contaminants both inside and outside. This cleaning procedure may involve a combination of techniques such as plasma treatment, washing the waveguide interior and/or exterior with DI water or different solutions, and high-temperature heating for a certain duration followed by gradual cooling. As a result, the pretreatment removes any impurities from the fiber surface, breaks existing bonds with organic molecules and/or inorganic materials, and coats the surface with hydroxy groups, which makes further modification easier. Secondly, the MOF surface is activated using a specific substance to facilitate adhesion of the material to be deposited. This is an optional

intermediate step, which may be employed when a more complex chemical modification is required. The final, third, step is the deposition of the functional layer.

In practice, the second and third steps are executed using one of several methods. For instance, when modifying the inner wall of the waveguide, the material solution can be delivered inside using capillary forces [44], which is the simplest experimental option but has the limitation of limited liquid elevation inside the capillary. Alternatively, the whole waveguide can be dipped into various solutions [44], thereby modifying not only the interior but also the outer walls of the MOF. A more complicated approach involves delivering the liquid inside the capillary using a syringe [34,35], which enables filling even relatively long waveguides but lacks precise control over the rate of solution supply into the MOF, potentially affecting the uniformity of the applied layer. Using different types of pumps [14,58,65] for solution pumping through the waveguide allows for the control of the flow rate and adjustment to the required values. To ensure the uniform application of material to the surface, it is recommended to create a sealed, hermetic connection between the waveguide and the tubes used for solution supply, to prevent air bubbles from entering the MOF.

To sum up, wall modification of microstructured optical fibers is provided in most cases with chemical methods, which refers to the process of altering the optical fiber's surface. This is done to integrate additional functionalities into the fiber or enhance its existing properties for various sensing applications. The modification process can involve coating the surface with a functional layer or creating an entirely new structure on it through various chemical techniques like LbL deposition, atomic layer deposition, silanization and others. The chemical wall modification of microstructured optical fibers can provide advanced sensing capabilities such as enhancing the sensitivity, selectivity, and dynamic range of the fiber, making it potential for various tunable applications in the fields of chemical sensing, biosensing, environmental monitoring, and biomedical applications.

2.1.4. HC-MOW applications for sensing

Unique design features of MOW, namely the presence of a hollow core and waveguide envelope channels, lead to specific guiding regimes. This phenomenon possesses great potential for using MOW in sensing systems. The guiding exists when the refractive index of the core is low compared to the effective refractive index of the shell. In a HC-MOW, the light is tightly confined in a low RI core because of the photonic bandgap formed by cladding or on the anti-resonant reflectance, as was discussed in the subsection 2.1.1 [66].

One limitation in terms of the principle of light propagation is the need to contrast the refractive index of the substance filling the core and shell channels of the waveguide with the refractive index of the substance from which the waveguide is made. Since the refractive index of gaseous substances is close to 1, the HC-MOW are readily suitable for sensing gases. At the same time, microstructured waveguides made, for example, of glasses with a high refractive index can be successfully used to create sensors for liquid media.

Microstructured waveguides enable highly efficient interaction between light and analytes in a longitudinal dimension. The use of hollow core waveguides allows trapping the minimum sample volume at very low concentration into a long optical path with tight optical confinement, which has been shown to enhance the analyte-light interaction by orders of magnitude, resulting in improved sensitivity and selectivity of biochemical sensors [67]. The transmission band of the waveguides can be tuned to the required wavelength range by changing the dimensions of the internal microstructure [68].

The waveguides facilitate the interaction between light and fluid/gas or substances carried in the form of fluid/gas (including chemical macromolecules and biomolecules) to generate a specific light response. Then efficient and rapid measurement of biochemical quantities can be achieved via the combination of various sensing mechanisms such as molecular absorption, fluorescence detection, refractive index, Raman scattering [69,70], etc.

Sensors based on HC-MOW offer superior performance and practicality, which makes them an ideal choice for a wide range of sensing applications. They enable enhanced long path analyte-light interaction, are portable, easy to use, and are relatively inexpensive to

produce on a large scale. Furthermore, MOW-based sensors have additional advantages such as ultra-low sample and reagent consumption, which makes them more effective [66,67,69–71]. In addition to biochemical sensing, hollow core microstructured optical waveguides can be widely employed in the sensing of various physical parameters such as temperature, strain, curvature, displacement, liquid level, and mechanical force, fully exploiting the intrinsic structure capabilities.

Refractive index and layer deposition sensing

Liquid sensing, based on the detection of changes in the RI of the measured medium, is one of the most important applications of HC-MOW. This makes it promising for environmental monitoring, food and beverage quality control, and biomedical diagnosis in a label-free and real-time manner. In contrast to conventional waveguides with a solid core, HC-MOW offer a completely hollow core which, when a sample is pumped into it, can enhance the interaction with the guided light in the core region. This enables greater sensitivity and control over the sensing, and potential to avoid cross-sensitivity to other factors by isolating samples from the external environment.

Wang *et al.* [72] proposed a fiber optic refractive index sensor based on the ARROW (anti-resonant reflecting optical waveguide) and mode interference. The experimental results demonstrate a high refractive index sensitivity of 19014.4 nm/RIU for mode interference and a large dynamic range from 0.04 RIU for ARROW.

Chen *et al.* [73] presented a highly sensitive waveguide sensor based on a liquid infiltrated modal interferometer in a hollow-core waveguide is presented. The sensor is specifically designed for refractive index and temperature sensing applications. The sensor shows a spectral shift towards longer wavelengths as the ambient liquid refractive index increases, with a highest sensitivity of 884 nm/RIU achieved around an RI value of 1.448.

Zhao *et al.* [74] proposed a liquid sensing method using a cascade of traditional single-mode fiber (SMF) - hollow-core fiber (HCF) - PCF - SMF structure, which simultaneously forms a reflective Fabry–Perot interferometer and a transmitting Mach–Zander interferometer. The HCF is filled with ethanol, which exhibits sensitivity to temperature

changes. By monitoring the reflection and transmission spectra, simultaneous measurement of temperature and RI changes can be achieved. The sensitivities for temperature and RI are up to 0.454 nm/°C and 178.7 nm/RIU, respectively.

Liu *et al.* [75] introduced an ultra-compact and highly sensitive liquid refractive index sensor employing cascaded Fabry-Perot cavities with an in-fiber mirror inscribed in single-mode fiber (SMF) using femtosecond laser technology. The Vernier effect which yields an ultra-high refractive index sensitivity of -73417.9 nm/RIU.

Zheng *et al.* [76] proposed a new high-linearity liquid sensing method using an analyte-filled defect hollow core Bragg fiber. This method employs a resonance wavelength induced by transverse coupling between core and defect modes to detect changes in RI of the liquid analyte. The sensitivity of 2062 nm/RIU was estimated.

Recently, Alam *et al.* [77] presented a biosensor based on PBG HC-MOW for detecting low-index liquid analytes, with a focus on detecting plasma concentration in blood samples. The sensor possesses an average spectral and amplitude sensitivity of 8928.57 nm/RIU.

Gao *al.* [78] proposed and experimentally demonstrated an optofluidic anti-resonant reflecting guidance in HC-PCF for the precise measurement of liquid RI with a sensitivity of up to 1328 nm/RIU.

Finally, Ermatov et al. [14] uses antiresonant HC-MOW and detects spectral shifts in the transmission spectrum caused by the presence of a bioanalyte, as demonstrated in Figure 2-5. By coating the identical HC-MOW instances with different number of polymer layers, a set of HC-MOW with different minima wavelengths can be obtained. In this case, the refractive index can be measured at up to 42 wavelengths, with a sensitivity of up to ~3000 $nmRIU^{-1}$ and a figure of merit (FOM) reaching 99 RIU^{-1} in the visible and near-infra-red spectral domains. Such approach offers a unique advantage over other optical biosensors, providing simultaneous measurement of a bioanalyte's RI over a wide spectral domain in real-time. The practical performance has been demonstrated by measuring the concentration and RI dispersion of BSA. The accuracy of BSA concentration measurement achieved by the present way matches that of standard tests on albumin.
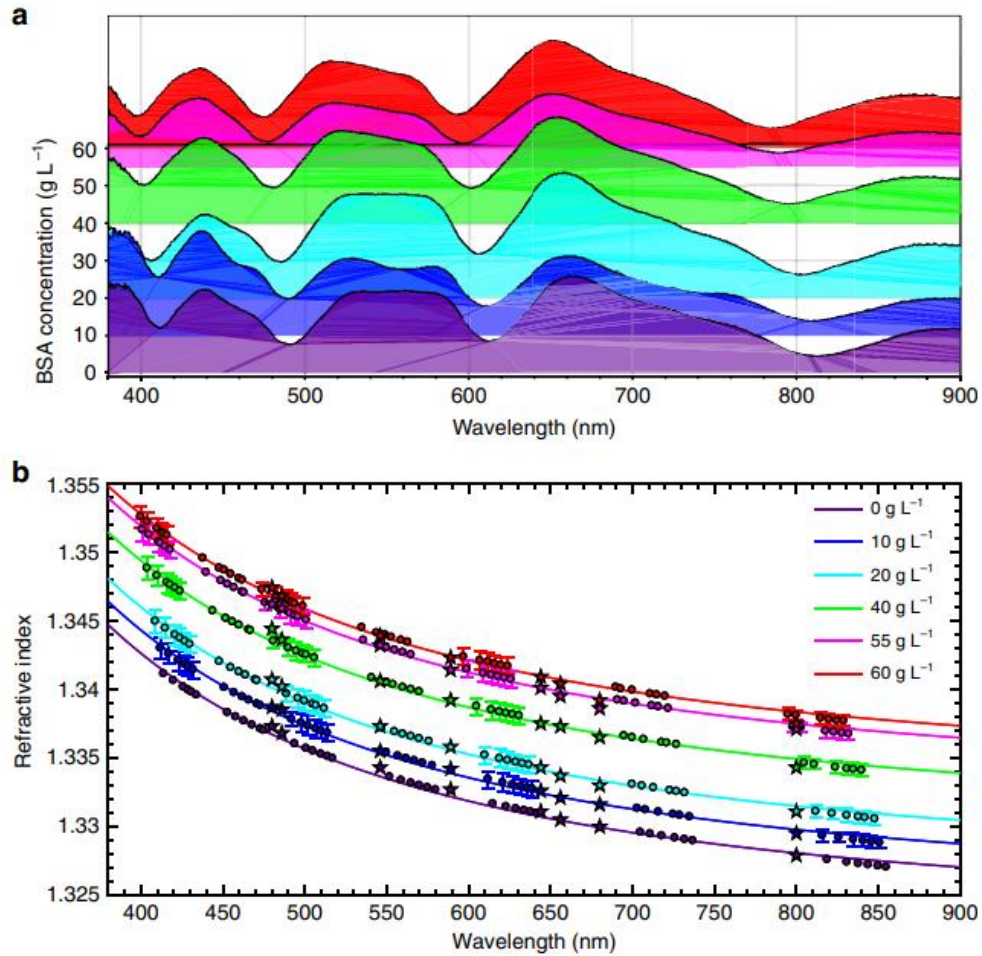
Figure 2-5. Performance of multiple antiresonant HC-MOW for BSA. a) Transmission spectrum evolution with increasing BSA concentration in HC-MOW. b) Optical dispersion of BSA in a water buffer with different concentrations. Coloured points: extracted from the shifts in the minima and the peak centroids of the fiber transmission spectra; solid line: their Sellmeier fits. The stars mark RI measured by the Abbe refractometer, provided for comparison. Reproduced from Ermatov et al. [14].

Raman and surface-enhanced Raman sensing

Raman sensing

Raman spectroscopy is a powerful technique used to analyze the vibrational properties of molecules. Additionally, Raman spectra is unique for every substance (so it is often

38

referred as "fingerprint"), that enables possibility to qualify and quantify substances [79,80], making Raman spectroscopy a great tool for biomedical application [81]. In conventional Raman spectroscopy, a sample is irradiated with a laser, and the scattered light spectum is analyzed to determine the vibrational frequencies of the sample's molecules. However, Raman signal intensity is often weak (as around 1 of 10^7 photons scatters inelastically), making it difficult to detect low concentrations [82].

One of the ways to improve Raman intensity by 1-2 orders is fiber-enhanced Raman spectroscopy (FERS): HC-MOF can enhance the intensity of Raman scattering signal observed by confining the laser light and the gas or liquid sample in a small volume, increasing the light-matter interaction length and guiding the scattered light directly to the detector [17,83]. The reviews by Markin *et al.* [84] and Ding *et al.* [17] comprehensively describe the use of microstructured optical fibers in Raman spectroscopy and demonstrate applicability of both PBG and antiresonant fibers for that. Furthermore, plasmonic nanostructures may be added to HC-MOF to provide surface enhanced Raman scattering (SERS) to improve Raman intensity even more. The variety of approaches to exploiting Raman scattering in a hollow-core fiber is presented in Figure 2-6. A bare HC-MOW enhances observed Raman signal intensity by 1-2 orders of magnitude compared to liquid in a form of a drop on a plain surface or filling a cuvette [85–88], thus providing improved detection sensitivity. Khetani *et al.* [87] explored the dependence of Raman signal amplitude on fiber length, and for the collection configuration aimed at backscattered Raman signal. PBG fiber and heparin-serum analyte got a maximum enhancement of 90 times at 8 cm fiber length. However, these values may be affected by analyte (light absorption, viscosity, surface tension) and fiber (loss) properties. Liquid analytes that were probed via Raman scattering in HC-MOF include e.g. heparin in serum [87], glucose [86], antibiotic moxifloxacin [85].
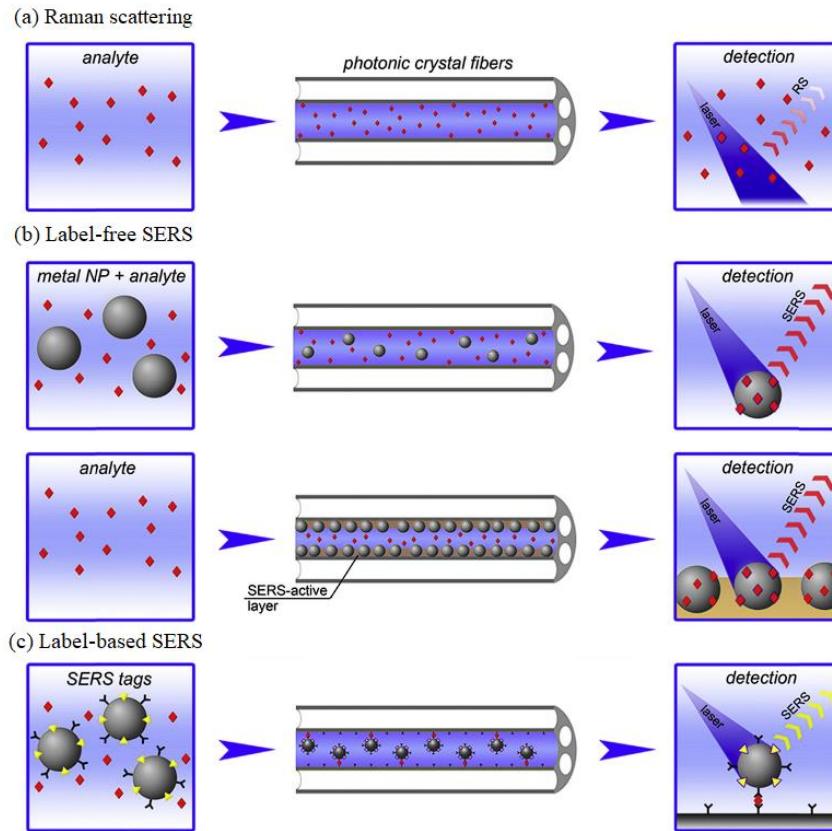
Figure 2-6. Raman and surface-enhanced Raman spectroscopy (SERS) with HC-MOW: (a) Raman scattering; (b) label-free SERS; (c) label-based SERS. Reprinted with adjustments from Markin et al.[18], copyright(2017), with permission from Elsevier.

The simplest way of performing Raman sensing of liquid with HC-MOF is to fill both core and cladding holes with an analyte. However, a PBG fiber has a disadvantage related to a narrow band gap in cladding modes and hence propagating core modes, as the laser and Raman scattering wavelengths should be in this bandgap. To expand its spectral range for Raman sensing, the cladding holes of the HC-MOW may be sealed, so the liquid fills ultimately the hollow core [85,89]. This type of fiber is referred to as liquid-core PCF. Along with liquid substances, HC-MOW is applicable for Raman analysis of gases composition for medical, environmental, industrial, purposes [11,83]. So, the analysis of human breath can disclose health issues such as malabsorption syndrome [90] and detect natural isotopes [91].

Surface-enhanced Raman sensing

However, as Raman scattering is characterized by low signal intensity [82], the bulk fiber enhancement may not be sufficient for detecting low concentration. Besides, multi-component systems (solution, gas) complicate the analysis of results. These difficulties can be overcome by exploiting plasmon resonance in metal nanostructures (typically made of gold or silver), called plasmonic nanostructures, which dramatically enhance Raman signal from molecules in their vicinity by amplifying both incident and inelastically scattered light. Such an amplification technique is referred to as SERS and may result in $10^6 - 10^{11}$ enhancement factor [92]. As demonstrated in Figure 2-6b, plasmonic nanostructures for SERS in HC-MOW may be implemented in a form of solution of nanoparticles (colloids) mixed with an analyte [20,89,93–100]. Methods for wall modification of HC-MOW are discussed in subsection 2.1.3. Plasmonic nanoparticles may be label-free and mixed with the analyte in a non-specific way [20,89,93,95,97–101] or provide targeted binding to particular molecules and contain Raman reporters as labels [102,103].

To gain greater enhancement for SERS in HC-MOW, various research groups implement a number of improvements, such as: in the case of colloidal suspensions of plasmonic nanoparticles, the use of anisotropic nanoparticles (nanorods, nanostars, nanotriangles, etc.) allows higher enhancement compared to spherical nanoparticles [104,105]; tuning the laser excitation wavelength close to the absorption peak of the colloid to excite surface plasmons more efficiently [96]; tuning the laser excitation wavelength in the electronic absorption band of the analyte to achieve several more orders of signal enhancement by engaging resonant Raman scattering [93].

Furthermore, an indirect SERS reporting, or label-based SERS, is demonstrated in Figure 2-6c and may be implemented to overcome a problem of a weak Raman scattering of the analyte or when providing molecule detection in a complex sample such as blood. Indirect SERS reporting assumes colloidal SERS nanoparticles with Raman reporter molecules on their surfaces, possessing a relatively strong Raman signal [84,106]. Simultaneously, these SERS nanoparticles are functionalized with targeting ligands to

molecules of interest. Such complex structures are called SERS nanotags. If the molecules of interest are previously absorbed on the HC-MOF inner wall, then the SERS nanotags will be captured via targeting ligands and provide signal from Raman reporters meaning that the molecules of interest are detected. Dinish et al. firstly demonstrated SERS detection of one cancer protein (EGFR) from a cell lysate [102] and then expanded the approach to multiple detection of three biomarkers using SERS nanotags with different targeting ligands and proteins [103].

2.2. Extracellular vesicles for medical diagnostics

2.2.1. Biomarkers for medical diagnostics

The accurate detection and diagnosis of cancer at the very early stages of its progression is of high importance as it increases the probability of achieving a successful treatment. Recently, liquid biopsy has emerged as a minimally invasive approach, which can potentially be used in medicine for early diagnosis and monitoring of patient's health. This approach is based on the reliable detection of tumor markers circulating in biological fluids using various techniques. Recently, identification and quantification of circulating tumor cells (CTC), circulating tumor DNA (ctDNA), and extracellular vesicles (their subtype called exosomes) have attracted particular attention for early cancer detection. Their size and time of appearance are compared in Figure 2-7.
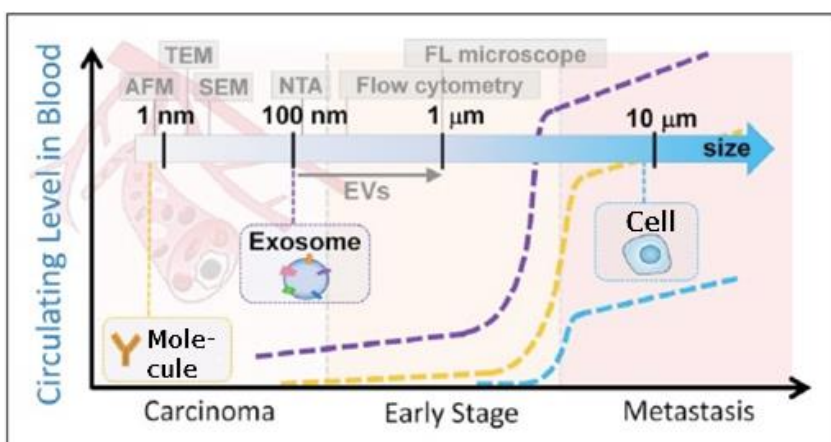
Figure 2-7. Markers for diagnostics. Adapted from He et al.[7]

CTC is one of liquid biopsy methods with relatively high specificity that allows performing in vitro examination by cell culturing as well as phenotypic and genotypic analysis. On the other hand, CTC's complex heterogeneity, low abundance (1–10 cells/10 mL of peripheral blood of cancer patients [7]), and difficulty to develop an enrichment technology in order to achieve a high limit of detection (LOD) present a challenge for CTC to be a single, universal, and reliable approach for cancer diagnostics in its early stages. Quantification and analysis of ctDNA present in cancer patient's blood is another liquid biopsy method that can become a supplement to conventional biopsies due to its high sensitivity and easy access to genomic information of the patient. Access to such information allows the selection of the most appropriate treatment and to monitor its effectiveness in real-time. In addition, it was shown that ctDNA levels often correlate with tumor burden [107]. However, ctDNA has a short half-life in blood (~2 h) [108] and can interfere with cell-free DNA (cfDNA) that is not related to the tumor [109]. Similar to CTC, current FDA-approved ctDNA assays have low LOD at ~25 copies/mL [110] making its detection and ability to obtain a detailed molecular profile a difficult task. Although detection of CTC and ctDNA can become highly effective approaches for cancer diagnosis, the mentioned challenges impact the feasibility of their implementation for diagnosis especially at the initial stage of cancer. In this respect, analysis of EV and specifically their subtype exosomes circulating in the patient's body is an innovative and promising method for the diagnosis of cancer and solving the most important problems of sensitivity, specificity, and reliability of currently available diagnostic methods.

2.2.2. Extracellular vesicles for diagnostics

Extracellular vesicles are nano- and microsized objects with a lipid bilayer produced by biological cells. Due to their biogenesis, EV may be divided into three subtypes, as demonstrated in Figure 2-8: microvesicles (ectosomes), which are produced by direct outward budding of the cell membrane; exosomes, which are produced by firstly inward budding of the cell surface region, then they are processed inside the cell and finally

43

released outside; and finally apoptotic bodies, which are the result of cell fragmentation after death [5].
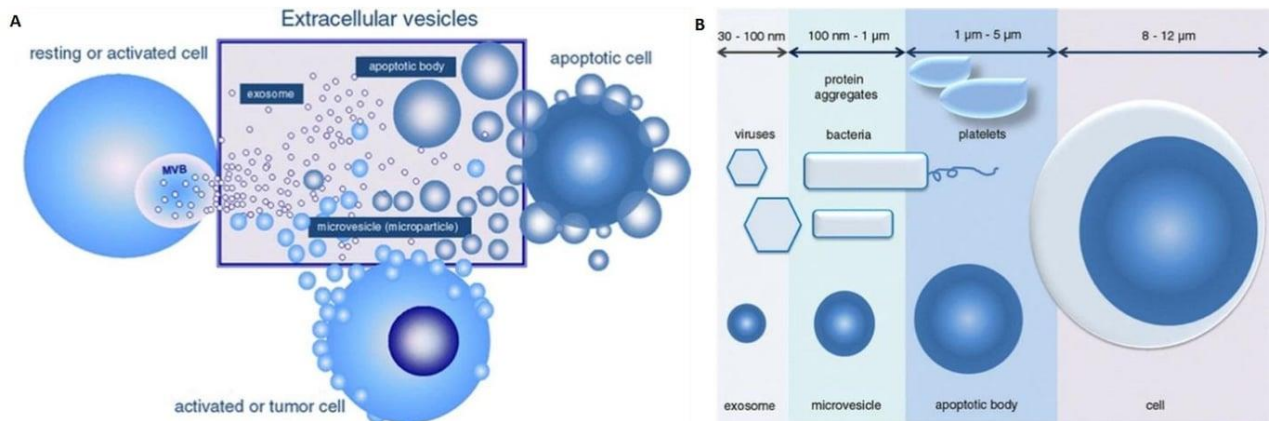
Figure 2-8. Types of extracellular vesicles: (a) role in communication, (b) size ranges. Adapted from Zhao et al.[111] Licensed under CC BY-NC-ND 4.0.

Due to a multistage process of exosome formation inside the cell, represented in Figure 2-9, exosomes are the EV that are most enriched with cellular footprint, such as the variety of proteins and nucleic acids. Therefore, exosomes are the most informative about the parental cells and hence represent the most interest for diagnostics. However, the isolation of only exosomal fraction from the EV solution is intricate due to ectosomes with intersecting size distribution. Therefore, sometimes an overall fraction of EV with sizes in the range 40-160 (200) nm is referred to as exosomes, although this is not technically correct and it should be referred to as extracellular nanovesicles (ENV) [112].

ENV are a minor component of plasma. Their quantitative and qualitative patterns are still poorly understood, but the emerging biological significance of ENVs is attracting growing scientific interest. It is now assumed that the population of circulating vesicles mediates the interaction of anatomically distant cells [113], and this population is extremely heterogeneous [114]. There are a number of ENV concentration estiomations.
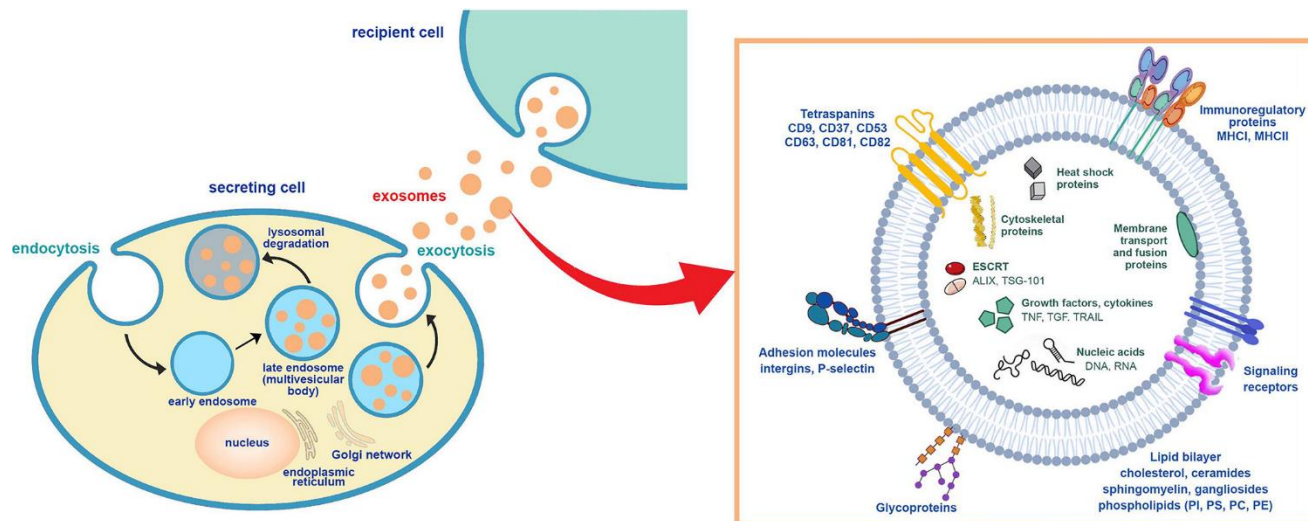
Figure 2-9. Exosome biogenesis. Reproduced from Tenchov et al.[3] Licensed under CC BY-NC-ND 4.0.

The most popular way of EV concentration estimation ways, nanoparticle tracking analysis (NTA), demonstrates that EV concentration in plasma varies from 10^{11} to 10^{12} particles per mL [115]. When ENVs were isolated by the standard ultracentrifugation procedure, the concentration of plasma ENVs differed by 2–3 orders of magnitude [115,116]. Such obvious discrepancies in the quantification of plasma ENVs may reflect the imperfection of both the isolation methods and the calculation technologies. The isolation of nanovesicles from plasma is indeed a nontrivial task, which has led to the development of many methods [117,118]. The current approaches can be generally divided into two main groups: methods based on specific physical properties of ENVs and methods based on the chemical characteristics of the vesicular membrane. The first group of methods includes ultracentrifugation as a "gold standard" [119], with various modifications (speed, time, gradient density medium) and ultrafiltration. More advanced approaches are based on microfluidic effects and nanoparticle flow fractionation phenomena [120]. The second group of methods is based on more or less specific binding of the components of the vesicular membrane with various ligands, including protamines , aptamers [121], antibodies [122], etc. This interaction leads either to the "fixation" of vesicles to a solid matrix or to the formation of multi-vesicular complexes, which are easily

45

precipitated by low-speed centrifugation. The first group of methods makes it possible to obtain fairly pure ENV preparations from plasma, but these methods are relatively laborious and associated with losses of vesicles during the isolation process. The methods of the second group have one common drawback—there is no known vesicular marker that would be presented exclusively on ENVs and on all ENVs. Therefore, ENVs isolated by any of the affinity methods represent a certain fraction.

2.2.3. Target extracellular vesicles detection using SERS spectroscopy

As was mentioned in subsection 2.1.4, Raman scattering can provide "fingerprint" information about unique molecular vibrations, that represents great interest in sample analysis. But there is a problem that typically for extracellular vesicles Raman scattering is too weak to provide readable spectra. Therefore, usually SERS technique is used, and also Raman reporters may be introduced to distinguish particular surface proteins via immunolabeling. Depending on if these reporters used or not, the used SERS is referred as label-free or labeled. Below the author focuses on approaches to analyze SERS spectra to distinguish between EV of different origin (produced by specific cell lines or cancer vs healthy ones)[123].

Label-free SERS

Direct analysis of SERS spectra implies identification of specific bands that differ for EV of different origin. For instance, Dong et al.[124] identified that EV of cancer patients demonstrated higher intensity of the Raman peak at 1087 1/cm, which corresponds to protein phosphorylation. However, still low peak intensity and overall EV SERS spectrum complexity make most researchers to use more advanced approaches for spectra analysis. The most popular is principal component analysis (PCA), where each wavenumber in a spectrum is considered as a dimension, thus a spectrum is a highly-dimensional field (as typically SERS spectrum is recorded on around 1000 wavenumbers), and then dimensionality reduction is implemented, building a few new coordinates in directions of the most variables variance in the highly dimensional field. These new coordinates are

called principal components. Principal components variations may indicate differences between EVs of different origin quite well, even for EV taken from serum, as demonstrated Russo et al. for blood malignant tumors[125]. However, PCA is a method of dimensionality reduction. For proper classification, it should be combined with classification algorithms, such as linear discriminant analysis[126,127]. Otherwise, another method of dimensionality reduction can be used, combined with classification algorithm: partial least squares discriminant analysis, multivariate curve resolution alternating least squares [128]. Also, deep learning models can be applied, and they tend to show the best values of sensitivity and specificity [129,130]

Labeled SERS

Generally, a SERS tag consists of three main parts: a targeting ligand (antibody, aptamers) to provide specificity and discriminate EV of a certain origin via specific proteins; a Raman reporter for a bright signal; SERS substrate to enhance the Raman signal from the reporter [123]. Thus, one label indicates the presence of only one protein. But multiple SERS tags with different targeting ligands and Raman reporters may provide multiplex classification or phenotyping[131,132]. The labeled SERS method for EV can be accompanied with immunoaaginity isolation using surfaces or magnetic beads with another targeting ligands. Thus, so called sandwich structures are built, when a single EV is isolated by capturing one protein on its surface, and is detected by a SERS tag bound to another surface protein[133–136].

2.3. Protein-copolymer microbubbles (MB)

2.3.1. Microbubbles as ultrasound contrast agents

Ultrasound is a widely-used imaging technique performed routinely in clinics, providing a cheap and non-invasive method of diagnostics[137,138]. However, poor image quality, namely contrast, limits ultrasound applications[139]. The solution is to use special contrast agents. According to physics staying behind the ultrasound imaging, the desired contrast agents should provide strong response to acoustic waves[140]. Therefore, gas-

47

filled structures, namely microbubbles, became the most popular ultrasound contrast agents, providing up to 1000 times sensitivity increase[141–143].

Microbubble shells can be made of lipids, proteins, or polymers. Shell composition primarily affects MB performance regarding storage stability, circulation time, and stimuli response. A lipid shell is relatively soft and thin, therefore MB made of them provide optimal oscillation and strong contrast profile, the gas can leak easily, shortening MB stability. Polymeric shells are harder and thicker, that improves their stability but reduces the contrast provided. A protein shell possesses intermediary properties[144–146].

2.3.2. Protein-copolymer structures

As described in the previous subsection, different shell materials lead to different properties of resulting MB. Aiming to expand MB properties, an idea of combination of two materials comes, such as making a hybrid protein-copolymer shell. To the author's knowledge, the group of P.Rudakovskaya in Gorin's Lab, Skoltech, are the first and the only authors who reported about protein-polymer MB[147]. Albumin is the most popular protein both and human blood and for pharmaceutics production. Bovine serum albumin, or BSA, is a low-cost reagent and is mostly identical to human serum albumin contained in human blood. It makes BSA a suitable biocompatible material for in vivo injection, including building MB contrast agents[148,149]. Meanwhile, Poly-N-vinylpyrrolidone (PVP) is a popular polymer in medicine and cosmetology due to its non-toxicity, ability to be excreted by the kidneys (up to 25 kDa) and chemical stability. PVP can be used as a stabilizer, film former and thickener[150]. In order to stabilize PVP, negative electrokinetic potential on its surface is needed[151]. This can be achieved by acrylic acid residues introduction to PVP main chain, giving birth to PVP-AA, and binding to proteins is enabled using ionic forces, with biocompatibility and hemocompatibility preserved. Therefore, BSA@P(VP-AA) MB were developed, taking advantages of both protein and polymer MB and demonstrating improved properties, such as increased concentration, acoustic response and stability.

2.3.3. Microbubbles and extracellular vesicles comparison

Both MB and EV are biocompatible spherical objects. MB are synthesized objects, averaging 1-5 µm in size, while EV are natural particles released by cells, and range from 0.04 to 1µm in size. Both types are encased in a shell: EV have a lipid bilayer while MBs may be surrounded by a shell made of lipids, protein, polymer, or a hybrid protein-polymer. The internal environment of EV is liquid and MB is filled with gas[152].

Considering their applications, both EV and MB are explored for diagnostic and therapeutic purposes. Extracellular vesicles (EVs) are naturally occurring in the body and serve as intercellular signal carriers. They are found in various biological fluids and hold the potential for liquid biopsy diagnostics[3,5]. Microbubbles (MBs) can be injected into large vessels or body cavities for in vivo imaging as ultrasound contrast agents[144,153]. Both MBs and EVs can also serve as effective drug carriers for targeted drug delivery. One of the primary impediments to drug delivery is penetrating the brain due to the blood-brain barrier (BBB). Nevertheless, extracellular vesicles (EV) are able to breach the BBB by default, while microbubbles (MB) require focused ultrasound facilitation[154–156].

Regarding composition, natural EV contain proteins on their surface (some of them are targeting ones) and inside, and may additionally contain nucleic acids inside. After conducting diagnostic analysis, EVs can be further functionalized with reporting molecules, including fluorescent dyes (for fluorescent microscopy or dot blotting) or Raman reporters (for multiclass classification)[1,9]. MBs can also be functionalized with magnetic resonance or other additional contrast agents for multimodal in vivo imaging. In case of acting as drug carriers, both EV and MB can be loaded with the desired drug[144,145].

Considering protein-copolymer MB introduced in subsection 2.3.2, there's one more resemblance: both MB and EV are multicomponent systems containing large molecules, that leads to rich Raman spectra. But in MB and corresponding complexes as precedessors, both protein and copolymer concentrations are ones or tens mg/mL, while EV are typically hanled with concentrations max. 10^{11} 1/mL, that corresponds to less concentrations of

proteins and lipids (around tens µg/mL). Thus, protein-copolymer MB are expected to provide greater Raman peak intensities.

2.4. Summary

The provided literature review demonstrated that HC-MOW can support IC guiding, which is most suited for sensing of liquids and gases because of numerous spectral ranges with high transmission. Multimodal sensing can be organized based on a combination of several techniques: a multi-wavelength refractive index sensor, a sensor with layer deposition control, a fiber-enhanced Raman scattering sensor, a SERS sensor. Combining several sensing modalities could allow for multifaceted characterization of complex fluids. The examples of such fluids are macromolecule structures, including biomarkers, among which EV represent the most interest.

Among the variety of biological markers present in liquid biopsy, recently discovered EV released by cells, especially their nanosized fraction, hold great interest for early diagnosis. The reasons for this is that a single EV contains a number of proteins and nucleic acids from its parental cell; moreover, in case of cancer, EV appear in blood earlier and in higher concentrations than currently exploited biomarkers (CTC and ctDNA).

There is another multicomponent structure that resembles EV in some properties, and this is microbubbles. Compared to natural origin of EV, MB are of synthetic origin and therefore may be easily obtained in necessary quantities. As well as EV, protein-copolymer MB are multicomponent systems providing rich Raman spectrum, but the concentrations of constituents are higher and thus Raman spectra of MB or their precedessor complexes should possess greater Raman intensity. Therefore, protein-copolymer structures (complexes and MB) may be used as training model samples for a system aiming to analyze Raman spectra of EV.

The problem postulated in this work is a lack of simple methods to characterize (detect and analyze) macromolecule colloidal structures, such as EV.

To address this problem, the aim of the present research work was to explore the full potential of HC-MOW in detecting EV by developing multifaceted liquid sensing

50

approaches. This will be accomplished by first testing a model dye in HC-MOW, followed by macromolecular nano- and microsized protein-copolymer structures, and ultimately EV.

Chapter 3. Research Methodology

In this Chapter, the methods used in the present work are described in detail.

3.1. Nanoscale visualization using SEM

SEM observations of HC-MOW and planar substrates were carried out without a metal coating using JEOL JSM-7200F FE-SEM. The hollow-core microstructured waveguides (HC-MOWs) were analyzed at 30 keV accelerating voltage using SE-detector. For the observation of the SERS-active substrates on glass slides, a beam deceleration function and charge-free scanning mode was used. To reduce the charging phenomenon the beam was decelerated in the vicinity of the specimen to 1.5 keV (gentle-beam mode). To use the low acceleration voltage the sample was biased to 2.0 kV. SEM images were taken by using an upper detector operating in the backscattered electron mode.

3.2. HC-MOW description

The HC-MOW used in the present thesis is provided by the company "Nanostructured Glass Technology LLC". The waveguide material is borosilicate glass. The geometrical structure is observed on SEM images (taken according to section 3.1) presented in Figure 3-1. The HC-MOW possesses a hollow core with 240 µm diameter and three rows of smaller capillaries around. The first wall thickness is 1.8 µm, which is estimated both by SEM imaging and from the Equation 3-1 for a bare HC-MOW.

The structures used for the study have a diameter of 240 µm of the central capillary and a thickness of the first wall of $1.8 - 2$ µm. The main part of the light is ~ 87 % guided inside the central capillary and approximately ~13 % in the first layer of adjacent capillaries.
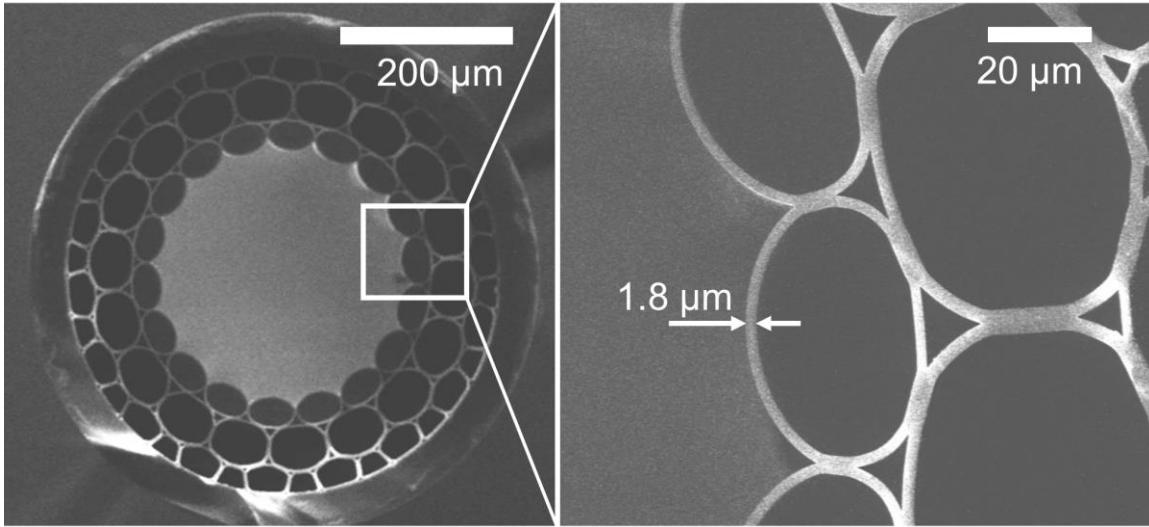
Figure 3-1. Scanning electron microscopy (SEM) image of Hollow−Core Microstructured Optical Waveguide (HC−MOW) tip.

It is worth noting that the core and cladding holes on SEM images in Figure 3-1 possess different intensities. For the left image, The waveguide was mounted vertically. the lighter zone in the center is due to possibility to register secondary electrons emitted by inner walls forming the core capillary. The surrounding cladding capillaries possess much smaller diameter, thus the probability of the electron showing up from them is smaller, hence these cladding capillaries look like darker. The picture on the right shows enlarged image of the side capillaries. To obtain such image, the HC-MOW was tilted by a certain angle, which was enough to eliminate the electrons from the core walls. Therefore, the contrast between hollow zones in the core and cladding capillaries is reduced compared to the left image.

3.3. HC-MOW transmission spectroscopy

3.3.1. Transmission properties of HC-MOW

The light propagation in HC-MOW is described similar to a Fabri-Perot cavity formed between parallel plates. Its transmission spectrum possesses minima whose positions are described by the following equation[13,157]:

$$\lambda_{jmin} = \frac{2d}{j} \sqrt{n_2^2 - n_1^2} \ , \qquad (3\text{-}1)$$

where j is an integer describing the capillary mode order ($j = 1, 2, 3, \ldots$), n_1 indicates RI of an analyte filling the capillaries, n_2 is the RI of the waveguide material, and d describes the waveguide wall (closest to the core) thickness. Transmission spectrum of an empty bare typical HC-MOW used in the present work is illustrated in Figure 3-2.
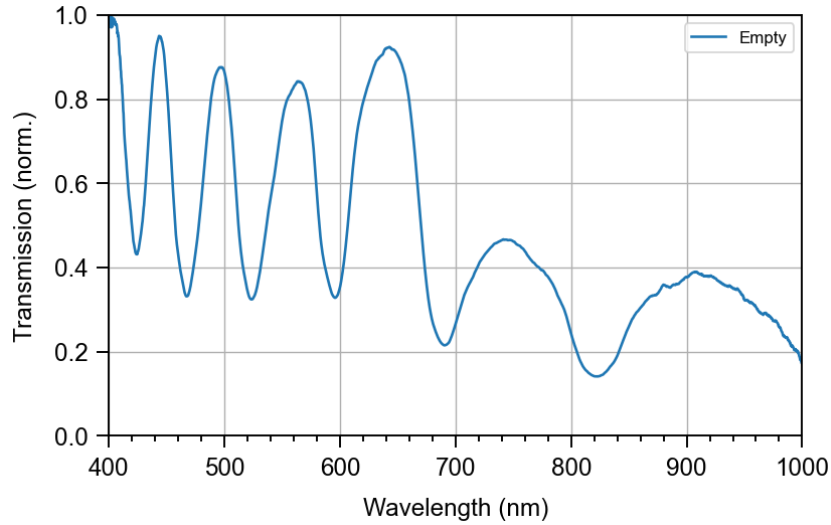
Figure 3-2. Transmission spectrum of a bare empty HC-MOW

The Equation (3-1) indicates that the transmission spectrum of the waveguide can be influenced by changing d, or, when MOW is already manufactured, by depositing various layers on the capillary walls. Moreover, the RI of the substance inside the waveguide can also affect its transmission spectrum. These characteristics make microstructured optical waveguides suitable for measuring the refractive index of liquid substances introduced to its core[14].

The formation of nanocoating leads to an increase in the effective thickness of capillary walls and shifts in the waveguide transmission windows and transmission minima towards longer wavelengths [14]. Also, feeding the HC-MOW with the analyte possessing the RI higher than water's one leads to spectrum shift towards shorted wavelengths.

In aspect of mode composition, the HC-MOW used (with a comparatively large hole diameter 240 um, which is important here) may be described as a hollow glass tube[158]. The wave propagation in this tube is carried out through Bragg reflection from the first wall: the reflection of a single wave at the inner and outer surfaces of the wall and their constructive interference; the other walls do not play a role. The obtained modes in hollow-core waveguides are intrinsically leaky, i.e. they continuously dissipate energy along the transverse direction[159,160,158], and the the modal losses scale with the inverse fourth power of core radius[158]. The number of these modes is extremely large. Knowing the number of modes plays an important role for telecommunication fibers of kilometers length, because it largely determines the loss and distortion of the signal: the fundamental mode drops with higher orders due to bends. In hollow-core fibers, in the vicinity of the light input tip, a large number of modes are spread, but losses for high-order modes are high, thus they leak rather quickly (in a few meters)[161]. However, in the present work the waveguide length is just 6 cm. There, it is usually spoken of mode discrimination, i.e. several lower order modes are selected and their losses relative to each other are evaluated, as demonstrated by Zeisberger and Schmidt [158]. The mode with significantly lower losses than the others survives. Technically, the number of supported modes may be calculated from the hollow tube dispersion, which is a standard approximation for hollow fibers of this type.

According to Zheltikov[13],the approximate attenuation coefficient for the mode of the m-th order is

$$\alpha_m \approx \frac{1}{\sqrt{n_2^2 - n_1^2}} \frac{(\lambda m)^2}{d_{core}^3 n_1}, \tag{3-2}$$

Where d_{core} is the core diameter.

According to the Equation (3-2), to deplete modes higher than m-th order, the waveguide length L may be chosen considering characteristic attenuation lengths for m and (m+1)th order modes:

$$\frac{1}{\alpha_{m+1}} < L < \frac{1}{\alpha_m}, \tag{3-3}$$

For the HC-MOW used in the present work, $L = 6$ cm, $d_{core} = 250$ um, $n_1 = 1$ (for air-filled HC-MOW), $n_2 \approx 1.45$ um. Then, for instance, at $\lambda = 500$ nm modes up to 30th order are transmitted without significant losses.

It's always important to excite a fundamental mode with minimum losses, thus the optical beam centering in the core plays a crucial role [162]. Therefore, the objectives in the measurement setup (will be described in the next subsection) are mounted in 3-coordinate stages, and the efficiency of free-space light coupling to the waveguide is provided by maximization of the intensity observed by the spectrometer.

3.3.2. Measurement setup

To estimate analyte RI or coating thickness in HC-MOW, optical transmission of the waveguide was measured on a custom-built setup described in [14] and presented in Figure 3-3. The HC−MOW is held horizontally by two liquid cells, providing hermetic clamping and thus enabling liquid analyte flow produced by a peristaltic pump with 50 µL/min flow rate. The optical setup includes a halogen lamp as a broadband light source, whose illumination is focused on the HC−MOW end. The liquid cells have transparent borosilicate glass windows to allow visible light transmission.

The output light of a broadband halogen lamp (Thorlabs SLS201L, 360–2600 nm) was initially collimated (Thorlabs F220SMA-532) and then focused by a 10× objective (Olympus) to the HC-MOW input. A focal spot diameter was less than HC-MOW core diameter (250 µm), that was clearly visually observed during the optical system alignment. The other two 10× objectives (Olympus) was used to collect the transmitted light, which was further guided to a compact CCD spectrometer (Thorlabs CCS100) operating in the extended wavelength region (200–1000 nm). All of the transmission spectra were initially normalized to the spectrum of the lamp and then to its maximum value. To estimate analyte RI or coating thickness, the positions of minima were calculated using a centroid function, as described by Equation 3-1.
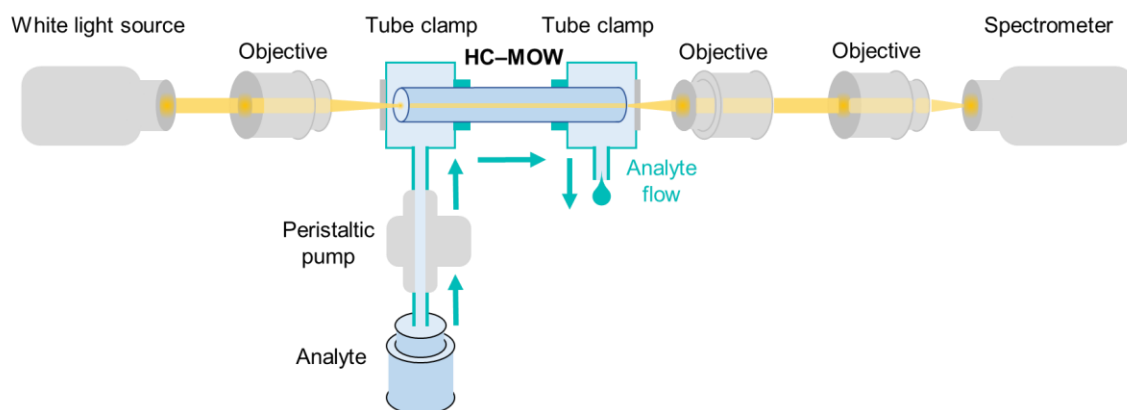
Figure 3-3. A setup for transmission measurement and RI sensing in a HC−MOW.

3.3.3. Refractive index calculation based on HC-MOW

As was described in the Equation (3-1), the RI of the solution inside the HC−MOW can be determined from the position of the minimum in the transmission spectrum of the filled waveguide, the thickness of the glass, its RI, and the capillary mode order. The exact measurements and data manipulation needed for RI extraction are provided below.

Firstly, the glass thickness is determined from the transmission spectrum of an air−filled HC−MOW. Local minima and their positions are located on the spectra, after which, using the least squares method, the thickness of the waveguide walls can be determined. The RI of glass at different wavelengths, *i.e.,* dispersion curve for waveguide glass was obtained from Noskov *et al.*[163].

Furthermore, based on the measured HC−MOW transmission spectra filled with different solutions, the positions of the local minimum can be found, and from the ratio of their wavelengths, the capillary modes order (*i.e., j*) is obtained for each of the tracked minima. Thus, this procedure provided us with the entire set of required data within the model for determination of the RI of the solution filling the HC−MOW. The wavelength positions corresponding to transmission minima are determined and named *min 1, min 2, min 3*, corresponding to wavelength ranges around 500, 600, 800 nm, which in their turn refer to capillary mode orders 5, 4, 3, respectively. Thus, RI values for these wavelengths are calculated according to Equation (3-1). For each minimum, RI dependence on concentration is approximated with a linear regression. For all three minima, R^2 values and

p−values are calculated to check if the dependence on concentration may be considered as linear and statistically significant for all three regions.

To evaluate RI sensing performance, RI sensitivity (RIS) is estimated, which is the ratio of the change in sensor output (in this case, the shift of the resonance wavelength) to the variation in RI of the analyte. The following equation defines RIS value as an analytical dependence of the derivative of the minimum's wavelength with respect to the refractive index of analyte:

$$RIS = \frac{\partial \lambda_{jmin}}{\partial n_1} = \frac{\partial \left(\frac{2d}{j}\sqrt{n_2^2 - n_1^2}\right)}{\partial n_1} = -\frac{2n_1 d}{j\sqrt{n_2^2 - n_1^2}} \qquad (3\text{-}4)$$

For each initial minimum position, it is possible to obtain RI of the material inside HC−MOW responsible for the shift in the location of the minimum:

$$n_1(\lambda_0, \delta\lambda) = n_1(\lambda_0) + \frac{\partial n_1}{\partial \lambda}\delta\lambda \qquad (3\text{-}5)$$

This approach allows to calculate the RI of the material inside the waveguide knowing the experimental shift in the spectrum, or, in other words, to predict what spectral shift expected in experimental measurements with a material of known refractive index. From this point of view, the lower limit of detection is determined by the experimental measurement error, which should be less than the expected spectral shift.

3.4. Confocal Raman microscopy

3.4.1. Principles of Raman effect

At high power density, light interacting with molecules is able to provide new spectral components in scattering. Frequency shifts between the incident and these scattered components correspond to transitions between vibrational (and in less extent rotational) levels of the molecules, and are called Raman shifts. The energy conservation law is completely kept, as one can see in the Equation 3-4 and in the Yablonsky diagram in Figure 3-4.

$$\hbar\omega_{inc} = \hbar\omega_S + \hbar\omega_R \qquad\qquad (3\text{-}6)$$
$$\hbar\omega_{inc} + \hbar\omega_R = \hbar\omega_{aS}$$

where $\hbar = 1.05 \cdot 10^{-34}$ J·s is a reduced Planck constant, ω_{inc}, ω_R are angular frequencies of the incident light and Raman shift (that corresponds to particular vibrational/rotational frequency in the molecule), and ω_S, ω_{aS} are the angular frequencies of the observed scattered light, namely its Stokes and anti-Stokes components, respectively. The Stokes component takes place when the molecule initially was on its vibrational ground state, and after scattering process it got additional energy and is in excited state. In this state, when another incident photon is scattered, it turns the molecule back to the ground level, and the scattered photon is blue-shifted and gives Anti-stokes component.
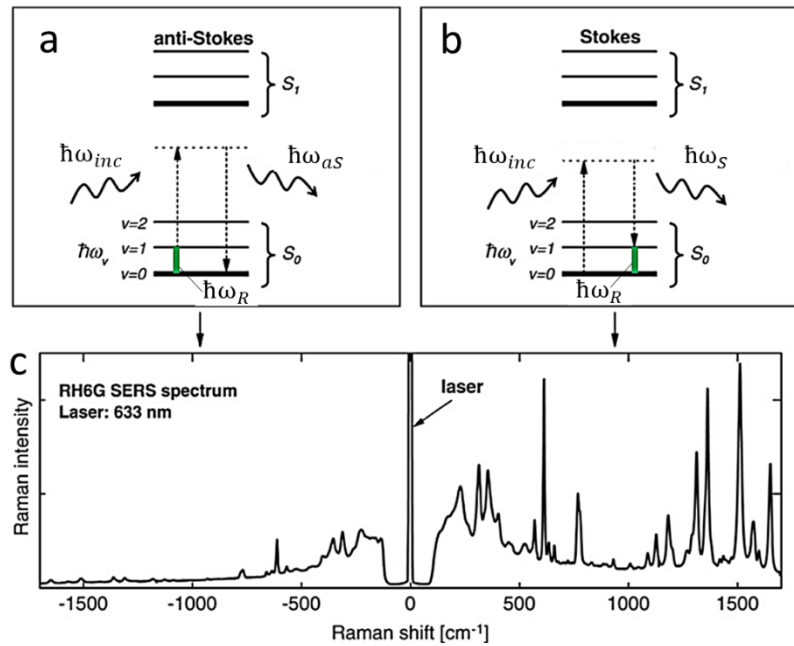
Figure 3-4. (a-b) Simplified Jablonski diagrams for anti-Stokes (a) and Stokes (b)

components of Raman scattering. (c)Surface-enhanced Raman spectrum of Rhodamine

6G. Reproduced with permission from Le Ru et al.[164] Copyright © 2009 Elsevier B.V.

It's worth noting that the dotted virtual energy state in *Figure 3-4*a,b doesn't have a real physical meaning and is drawn here just to facilitate quantum-mechanical understanding. For that purpose the scattering process is broken down into two steps and

viewed as the combination of the incident photon coming and spontaneous emission, but actually absorption doesn't happen.

To understand the origin of Raman scattering, an insight into light interaction with matter is needed, namely the optical polarizability theory, where the simplest and satisfactory for many cases is the Lorentz model. The interaction of an electromagnetic wave (only real part is taken for simplicity)

$$E_{inc} = Re[E_0 exp(-\omega_{inc}t)] = E_0 cos(\omega_{inc}t) \quad (3\text{-}7)$$

with the molecules is described by polarizability α, which is the ability of a molecule to acquire an induced electric dipole moment (distortion of charge distribution) when it is placed in an external electric field. In a linear model of the medium, there is an assumption that the molecule is in ground state, in its minimum of total energy and atoms are static. Then, linear polarizability is entirely determined by electronic structure of the molecule and is determined as follows:

$$\alpha_L(\omega_{inc}) = \frac{e^2/m}{\omega_p^2 - \omega_{inc}^2 - i\Gamma\omega_p} \quad (3\text{-}8)$$

where e is the electronic charge, m is the effective mass of the electrons, ω_p is plasma frequency.

The induced dipole demonstrated scattering ultimately on the incident wavelength:

$$\vec{p}(\omega_{inc}) = \alpha_L(\omega_{inc}) \cdot \vec{E}_{inc}(\omega_{inc}) = \alpha_L(\omega_{inc}) \cdot E_0 cos(\omega_{inc}t) \quad (3\text{-}9)$$

Meanwhile, in a nonlinear model, explaining Raman effect, atoms are able to vibrate with frequencies ω_v, with restoring forces q due to interaction with neighboring atoms, that leads to polarizability modulation with these vibrational frequencies (in approximation of low perturbations), and a new component in the induced dipole:

$$q = q_v cos(\omega_v t) \quad (3\text{-}10)$$

$$\alpha_R(\omega_{inc},\omega_v) = \alpha_L(\omega_{inc}) + q(\omega_v) \cdot \frac{\partial\alpha}{\partial q}\bigg|_{q=0} + \cdots$$

This leads to the new component in the induced dipole:

$$\vec{p}(\omega_{inc},\omega_\mathrm{v}) = \alpha_R(\omega_{inc},\omega_\mathrm{v}) \cdot \vec{E}inc(\omega_{inc}) = \qquad\qquad (3\text{-}11)$$

$$= \alpha_L(\omega_{inc}) \cdot E_0 cos(\omega_{inc}t) +$$

$$+ \frac{q_\mathrm{v}}{2} \cdot \frac{\partial \alpha}{\partial q}\Big|_{q=0} \cdot E_0 \left\{ cos[(\omega_{inc} + \omega_\mathrm{v})t] + cos[(\omega_{inc} - \omega_\mathrm{v})t] \right\}$$

Therefore, the frequencies $(\omega_{inc} + \omega)_\mathrm{v}$ and $(\omega_{inc} - \omega_\mathrm{v})$ are the new components in the scattered light (compared to incident one) and represent Raman scattering.

It is worth noting that for Raman scattering effect, polarizability change due to vibrational motion should take place. Molecules with certain symmetry, especially small ones, may have vibrational modes extinguishing each other, thus Raman scattering won't be observed. Meanwhile, polar groups are prone to Raman effect. Large molecules are more polarizable, therefore Raman is popular for organic molecules.

3.4.2. Raman measurements

For all samples, Raman measurements were carried out using Raman spectrometer LabRAM HR Evolution (HORIBA France SAS, France), with a diffraction grating 600 lines/mm, 633 nm laser. The detector used is a nitrogen-cooled Symphony OE. All spectra were corrected for baseline using built-in Labspec 6 software.

3.4.3. Raman measurements of EV in a drop

For Raman measurements of EV in a drop, in addition to described in subsection 3.4.2, a 50x objective was used and 6 mW laser power at objective output. A small drop ($\sim$1 μl) of a plasma EV sample was pipetted on a fused quartz surface and dried at room temperature. The analyte concentration was increased by placing the second drop in the exact location and drying. Three spectra were accumulated and averaged. Each of them was taken with a 50-s exposure time for EV isolated by depth filtration, or 50/120s exposure time with normalization for EV isolated by a two-phase polymer system.

3.4.4. Experimental setup for Raman measurements in HC-MOW

The experimental setup for Raman and SERS measurements in HC-MOW is demonstrated in Figure 3-5. The HC−MOW is fixed vertically by a waveguide clip. The

waveguide bottom end is dipped in the liquid that fills the cavities inside via capillary forces. The 10x Olympus MPlan objective of Raman spectrometer is focused on the liquid surface the center of in the top waveguide end, with 12 mW laser power. Raman signal is collected in a backscattering mode. The data are presented as mean ± standard deviation: for that, 5 measurements of the same liquid sample were taken for averaging, with de novo focusing for each measurement. Each of these independent measurements was also internally averaged to 3 accumulations by Raman spectrometer software.
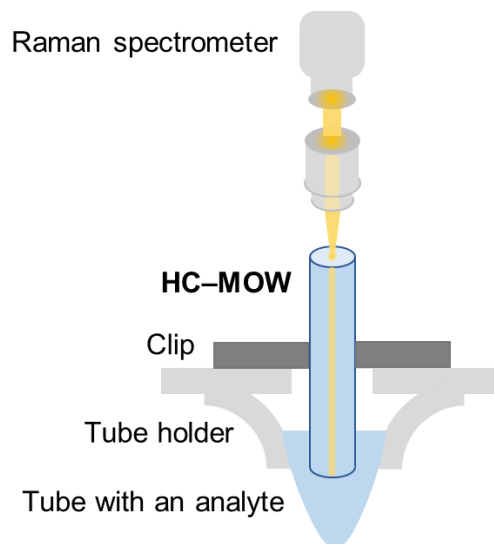
Figure 3-5. A setup for Raman scattering measurement in a HC−MOW. The bottom end of HC−MOW is dipped into a liquid analyte, so the liquid fills the whole waveguide, and the objective of the Raman spectrometer is focused to the liquid surface on the top waveguide tip.

3.5. SERS substrates fabrication

3.5.1. Principles of SERS

An important disadvantage of Raman spectroscopy for wide applications is the weakness of Raman signal. SERS allows to overcome it by introducing metal nanostructures, which allow enhance the signal by several orders. This happens due to free conduction electrons in metals, these electrons form free-electron plasma, have no restoring

force ($\omega_0 = 0$) and move in a background of fixed positive ions. When the metal nanostructure is placed in the electromagnetic field, the optical response of plasma determines the optical response of the <mark>nanostructure</mark>. Local dielectric function for a real metal is

$$\varepsilon(\omega) = \varepsilon_b(\omega) - \varepsilon_\infty \frac{\omega_p^2}{\omega^2 + i\gamma_o\omega} \tag{3-12}$$

where ε_b corresponds to inter-band transitions, ε_b stands for intra-band transitions, γ_o is a damping term meaning collision rate of free electrons with the crystal impurities.

Linking the dielectric function to experimental optical constants, expressions for the refractive index $n(\omega)$ and excinction coefficient $\kappa(\omega)$ can be obtained:

$$\varepsilon(\omega) = \big(n(\omega) + i\kappa(\omega)\big)^2 = n^2 + \kappa^2 + i \cdot 2n\kappa$$

$$\Rightarrow \ n(\omega) = \sqrt{\frac{Re(\varepsilon) + |\varepsilon|}{2}} \tag{3-13}$$

$$\kappa(\omega) = \frac{Im(\varepsilon)}{\sqrt{2}\sqrt{Re(\varepsilon) + |\varepsilon|}}$$

The corresponding values of real and imaginary parts of the dielectric function of real metals are demonstrated in Figure 3-6.
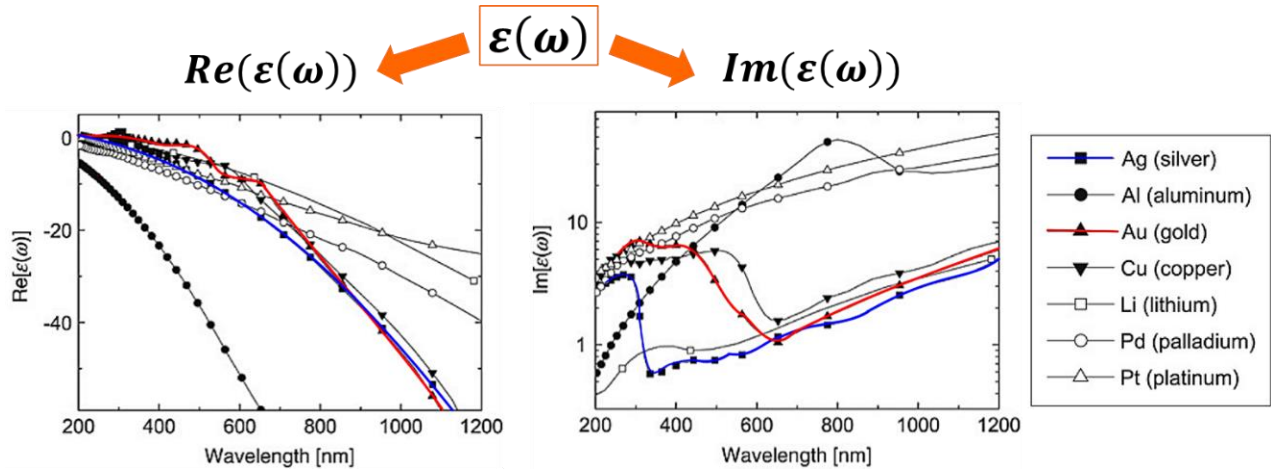
Figure 3-6. Real and imaginary parts of the dielectric function for different metals.
Reproduced with permission from Le Ru et al. [164] Copyright © 2009 Elsevier B.V.

Plasmonic nanostructures are characterized by their dimensions, which are considerably smaller than the wavelength of the incident light. These nanostructures support collective electronic oscillations called localized surface plasmons (LSPs) when excited by light under specific conditions of frequency and polarization that satisfy the resonance criteria. Detailed discussions of these resonance conditions can be found in [164–166]. At resonance, LSPs manifest as sharp spectral features in the nanostructures' optical response, known as localized surface plasmon resonances (LSPRs). These resonances lead to pronounced local electromagnetic field enhancement, particularly on the metal nanoparticle surface, which is the principle behind SERS. This enhancement occurs in the near-field region and is predominant on the nanoparticle's surface.

As a simplest example, a complex electric field E_{In} inside the sphere could be estimated:

$$E_{In} = \frac{3\varepsilon_m}{\varepsilon(\omega)+2\varepsilon_m}E_{inc} \tag{3-14}$$

where ε_m is a dielectric function of the medium and E_{inc} is incident electric field. Similar local field enhancement exist for other geometries and configurations, but providing slightly different coefficient between E_{In} and E_{inc}.

Continuing the example with a nanosphere in (3-11), E_{In} may be infinitely large if

$$Re\big(\varepsilon(\omega)\big) \approx -2\varepsilon_m$$
$$Im\big(\varepsilon(\omega)\big) \approx 0 \tag{3-15}$$

In practice, the first condition, for a generalization of material choice for SERS, is substituted by

$$-20 \leq Re(\varepsilon(\omega)) \leq -1 \tag{3-16}$$

Thus, the metals may be chosen by comparing their real and imaginary parts of the dielectic constant, as presented in Figure 3-6.

But for real-life applications, other aspects also should be taken into account, such as: inertious for chemical reaction, especially with water (therefore, e.g. lithium is not suitable); availability; ease of manipulation, nanostructures fabrication; toxicity, etc. Thus,

gold is preferred at wavelength larger that 600 nm. However, silver is used in the whole visible range and around.

3.5.2. Gold nanoparticles synthesis

THPC AuNP seeds

AuNP seeds, which are an aqueous solution of AuNPs with tetrakis-(hydroxymethyl)-phosphonium chloride (THPC) as simultaneously a reducing agent and stabilizing ligand, were provided by Dr.Khlebtsov and Saratov State Universrity. AuNP were synthesized as described previously [167], with gold concentration 1 mg/mL. Briefly, a glass vessel was filled with 45.5mL of distilled water. Then, under continuous stirring, portions of aqueous solutions of sodium hydroxide (0.2 M, 1.5 mL), the reducing agent THPC (1 mL of a solution of 1.2 mL of 80% aqueous solution diluted to 100 mL with water), and the metal salt chloroauric acid (2 mL of dark-aged stock solution, 25 mM) were added. The interval between THPC and chloroauric acid is 2 minutes. In a result, orange-brown gold hydrosol was obtained. Three months passed between the seed preparation and their utilization in the current experiment, therefore their size increased due to Ostwald ripening.

Citrate AuNP

Larger AuNP stabilized by citrate in an aqueous solution were synthesized with gold concentration 0.2 mg/mL by a modified Turkevich method [168]. Briefly, 150 mL water solution containing gold tetrachloraurate (III) ($HAuCl_4$, Sigma Aldrich) at concentration 1 mg/mL was slowly heated with rigorous stirring to boiling. Subsequently, an excess of citrate solution (25 mL 1% aquaeous solution, $Na_3C_6H_5O_7$, Sigma Aldrich) is added to the mixture. Through the application of heat, nucleation of gold nanoparticles occurs, followed by their growth in size. Citrate ions work both as reductors and stabilizers. Nanoparticle size and concentration have a functional dependence on citrate ions concentration.

3.5.3. Gold nanoparticles size distribution characterization

Both types of AuNPs were imaged by transmission electron microscopy (TEM) and their size distribution was estimated using dynamic light scattering (DLS).

TEM images were taken on a Zeiss M912 Omega transmission electron microscope (Carl Zeiss Microscopy GmbH, Oberkochen, Germany) at an operating voltage of 300 kV.

DLS analysis was provided on Zetasizer Nano ZS (Malvern Panalytical), with 3 measurements for each sample.

3.5.4. Gold nanostructure formation on planar slides

Firstly, SERS substrates on planar microscope slides were fabricated. SERS subsrates made of two types of AuNPs were compared by the SERS enhancement produced: small AuNPs (gold seeds) stabilized with THPC and larger AuNPs stabilized with citrate, synthesized as described in the previous subsection.

Three types of SERS substrates were fabricated, as illustrated in Figure 3-7: bare glass
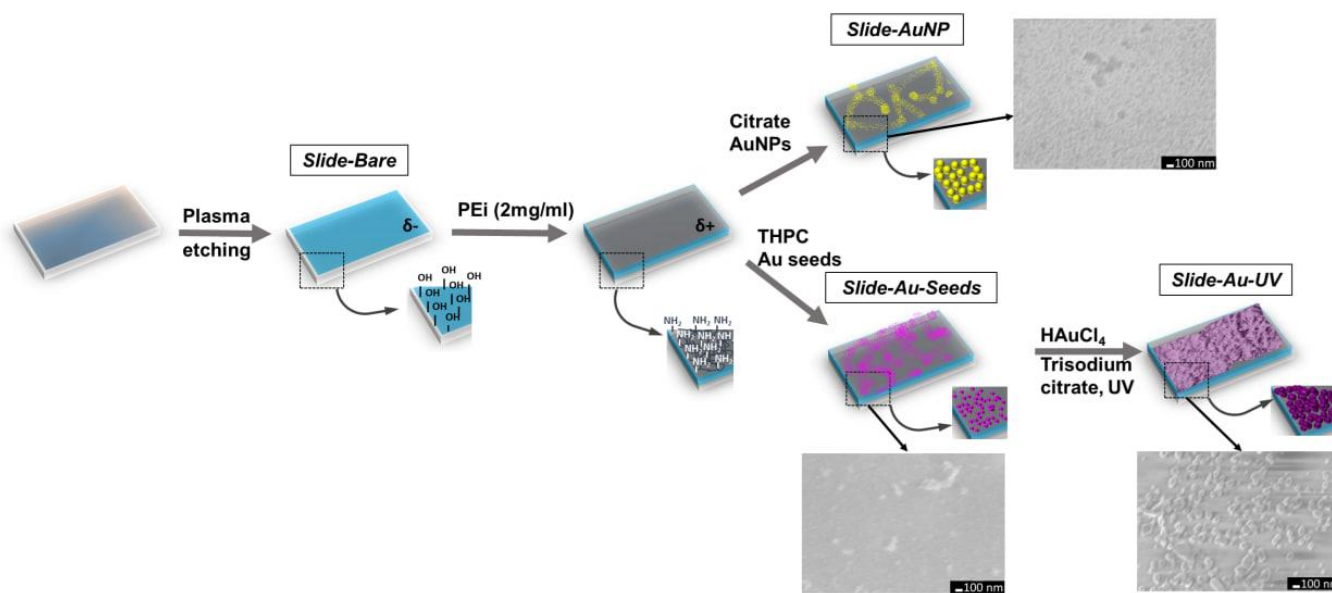
Figure 3-7. Gold nanostructure formation on planar slides.
Pictures incorporated are the corresponding SEM images.

66

slide (sample Slide-Bare); glass slide functionalized with PEi and citrate-stabilized AuNPs (sample Slide-AuNP); glass slide functionalized with PEi and UV-mediated chloroauric acid reduction on gold seeds (sample Slide-Au-UV).

Initially, microscope borosilicate glass slides were taken and etched with oxygen plasma to clean the surface and to obtain hydroxyl groups on the glass surface. Then slides were covered with Polyethyleneimine (PEi, MW 750,000, Sigma Aldrich) to induce a positive surface charge which is necessary for further efficient electrostatic absorption. Then two types of negatively charged AuNPs (stabilized with citrate and with THPC) were adsorbed on slides by incubation and thus samples Slide-AuNP and Slide-Au-Seeds (the intermediary result of the two-step process) were obtained, respectively. The last step was Slide-Au-Seeds improvement to Slide-Au-UV by UV-mediated reduction of HAuCl4 in citrate presence. For that, Camelion LH26-FS 26W light bulb was used as a UV source, with an emission spectrum centered at 365 nm. Samples were placed approximately 3 cm under the vertically mounted bulb, so that power density on the sample measured at 365 nm was 4.3 mW/cm^2. Slides were covered with an approximately 2 mm layer of a mixture of 0.01% chloroauric acid and 0.01% trisodium citrate in 2:1 v/v and irradiated by a UV lamp for 15 min, and then finally gently washed with water.

3.5.5. Gold nanostructure formation in HC-MOW

The fabrication of SERS-active HC-MOW samples is illustrated in Figure 3-8. Similar to the process used for SERS substrate fabrication on microscope slides, firstly HC-MOWs were first treated with oxygen plasma to clean their surfaces and to place hydroxyl groups on waveguide walls. Then HC-MOWs were functionalized with PEi using a peristaltic pump (Schenchen) to obtain a positive surface charge which is necessary for further efficient electrostatic absorption: PEi at concentration 2 mg/mL was delivered for 7 min at a speed of 150 mL/min. Afterward, HC-MOW was washed for 2 min by deionized water and dried with air flow using a syringe; then, an hour later, the transmission spectrum was measured. Following this, THPC AuNP seeds at concentration 0.1 mg/mL (10x diluted from the initial value), providing volume fraction 0.5%, were deposited overnight (14 h) at

67

a speed of 150 µL/min using the same pumping system. Afterward, HC-MOW was washed for 2 min with deionized water and dried with air flow using a syringe. Thus, the sample MOW-Au-Seeds was obtained then, an hour later, the transmission spectrum was measured.

The last step was to obtain MOW-Au-UV by UV-mediated reduction of HAuCl4 in citrate presence on the surface of MOW-Au-Seeds. HC-MOW was filled with a mixture of 1% chloroauric acid and 1% trisodium citrate in 2:1 v/v and irradiated by a UV lamp for 2 h, being left in a vial with the solution to avoid drying. Finally, HC-MOW was dried at 50 $^{\circ}$C overnight and washed with water, then dried with air flow using a syringe, and an hour later, the transmission spectrum was measured.
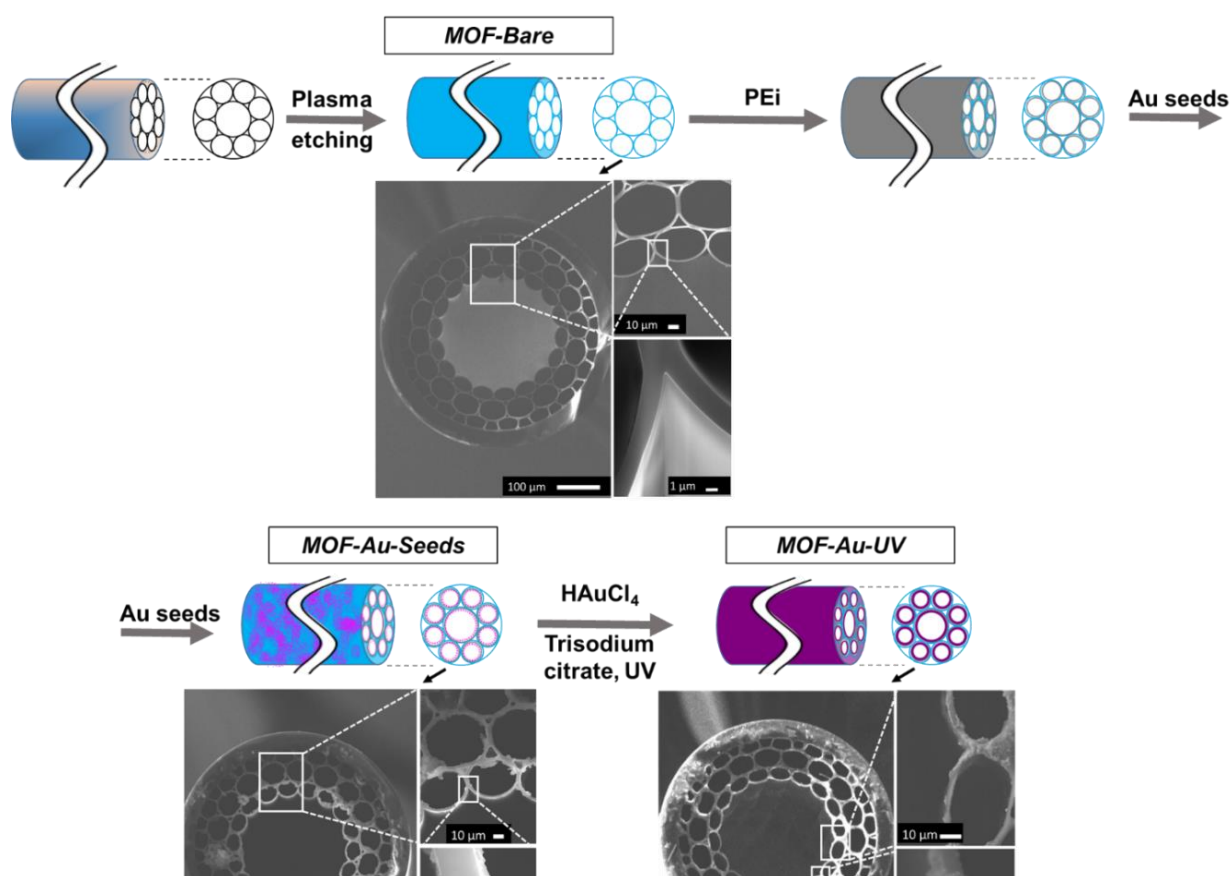
Figure 3-8. The fabrication process of SERS-active HC-MOW with corresponding SEM images incorporated.

3.6. BSA@P(VP-AA) structures

3.6.1. BSA@P(VP-AA) synthesis

The components needed for synthesis are the following: BSA, N−vinyl−2−pyrrolidone (NVP), acrylic acid (AA), 2,2′−azobis (2−methyl propionitrile) (AIBN), 1−octadecanethiol (ODT) are all purchased from Sigma−Aldrich (Germany). 1,4−dioxane is purchased from Chimmed (Russia).

The copolymer of poly (N−vinylpyrrolidone−*co*−acrylic acid), labeled as P(VP−AA) throughout the manuscript, is synthesized similarly to Estifeeva et al.[147]. Briefly, NVP and AA are dissolved in 1,4−dioxane with desired amounts, AIBN and ODT are added to the mixture, followed by sealing the vial and keeping it for 3 h at 70 °C. After the synthesis, a copolymer is purified by dialysis with the membrane cut−off 0.5 kDa and freeze−dried. The same set of methods is used to assess the properties of the resulting amphiphilic copolymer as in[147,169,170]. The P(VP−AA) copolymer used in the present work shows a molecular weight of 18 kDa with 9.7 mol %. of AA units randomly distributed in the chain structure.

The synthesis route of BSA@P(VP−AA) complexes and MB is presented in Figure 3-9 and similar to the previous report [147]. Briefly, initial compounds are dissolved in aqueous solution with desired protein: copolymer ratios of 3:1, 5:1, and 10:1 and at the total mass concentration of 50 mg/mL to produce complexes (BSA@P(VP−AA) [3:1], BSA@P(VP−AA) [5:1], and BSA@P(VP−AA) [10:1], respectively). Next, each complex solution with protein: copolymer mass ratios of 3:1, 5:1, and 10:1, that equals to molar
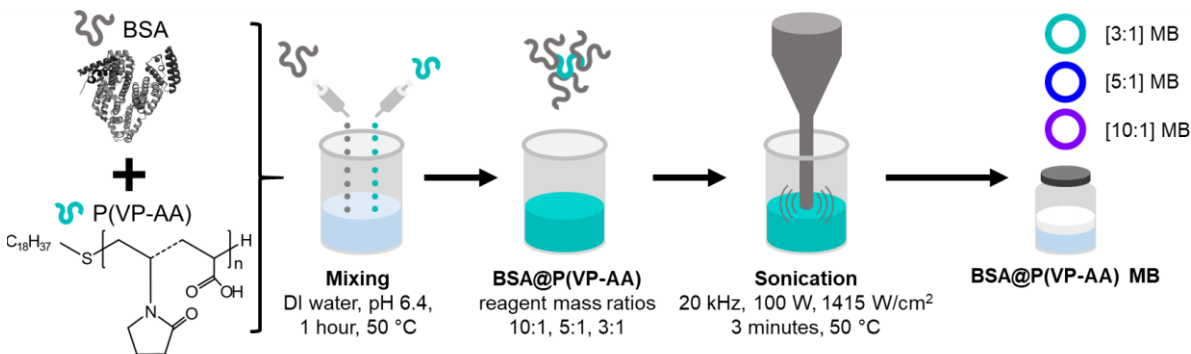
Figure 3-9. Synthesis of BSA@P(VP−AA) complexes and microbubbles

ratios 1:1.5, 1:1, 2.3:1 is sonicated to produce MB (labeled as [3:1] MB, [5:1] MB, and [10:1] MB, respectively).

The mass concentration of 50 mg/mL is the most preferred one for stable BSA based MB synthesis[171]. Therefore, all complexes and MB used in the present work are produced at the total mass concentration of 50 mg/mL as the optimal concentration for MB synthesis.

3.6.2. Extinction spectroscopy

Extinction spectra are obtained on a spectrophotometer Infinite M Nano+ (Tecan Trading AG, Switzerland) dual−mode reader. The extinction spectra are measured at room temperature (25 ± 1 °C), with a 2 nm step and a 9 nm bandwidth, within the wavelength range of 230 – 900 nm.

3.7. Extracellular vesicles isolation

3.7.1. Asymmetric depth filtration for EV from plasma

Plasma samples

Biological samples (blood, urine and Wharton's jelly of umbilical cords) were collected with written informed consent from healthy donors (Protocol № 8 approved on 3 September 2020, by the Institutional Ethical Commission of the FSBI 'National Medical Research Center for Obstetrics, Gynecology and Perinatology named after Academician V.I. Kulakov' of the Ministry of Healthcare of the Russian Federation). Blood was drawn into EDTA-treated tubes (VACUETTE K2E K2EDTA, Greiner Bio-one, Austria). Cells were removed by centrifugation for 10 min at 1000×g and 4∘C. The supernatant was centrifuged again (2000×g and 4∘C) to remove platelets and obtain plasma. The collected urine was purified by discarding the pellet precipitated by 30-min centrifugation at 4500×g and 4∘C. The samples were aliquoted (1.5 ml of plasma and 15 ml of urine) and stored in Eppendorf tubes (Hamburg, Germany) at –20∘C until use.

EV isolation process

The method described here implements asymmetric depth filtration (DF), in which EVs are immobilized on the surface and within the depth of the filter, while small (e.g., lipid) particles, proteins and other solubilized components of plasma, urine and cell culture medium elute with the flow. EVs accumulate inside and on the surface of the filter and are later recovered by reversing the direction of the carrier flow.

The DF membrane was fabricated by dry casting a mixture of cellulose acetates of different acetyl numbers following a similar approach to the one described by Sossna et al. [172]. The pores narrow with depth into the membrane ($\sim$20-μm thick) and terminate with much smaller exit apertures. When a sample flows in the forward direction through surface 1, EV are retained inside narrowing and tortuous pores. The immobilized EVs may then be cleansed by the forward flow of a washing buffer to reduce contamination. The reverse flow of resuspending buffer flown in the opposite direction through surface 2 recovers the immobilized EVs from the membrane for downstream applications.

This study used centrifugal forces to drive forward and reverse flows across the membrane. A disk of DF medium, 22 mm in diameter, was held inside a cylindrical acrylic cartridge (19/25 mm ID/OD) designed to fit inside a standard 50 ml centrifuge tube.

The sample measured in the present thesis was EV in PBS buffer isolated by the described protocol, with concentration $(3 \pm 0.4) \cdot 10^{11}$ particles per mL.

3.7.2. Two-phase polymer system for EV isolation from plasma

Plasma samples

Plasma was obtained fromn healthy donors in the blood transfusion department of N.N. Petrov NMRC of Oncology. Blood was collected in a BD Vacutainer spray-coated ethylenediaminetetraacetic acid (EDTA) tubes, and plasma was immediately separated from the blood, aliquoted, and stored at 80C. Before use, plasma was slowly thawed at +4C. In order to remove cells, cellular detritus and large protein complex plasma was centrifuged: 300g—10 min, 2000g—20 min, 10,000g—40 min.

Polymer components

The components explored for the method development were the following: dextran 20 kDa (Serva, Heidelberg, Germany), dextran 200 kDa (Serva, Heidelberg, Germany), dextran 450–650 kDa (Sigma-Aldrich, St. Louis, MO, USA), PEG 6 kDa (Serva, Heidelberg, Germany), PEG 15 kDa (Loba Chemi, Mumbai, India), PEG 20 kDa (Loba Chemi, Mumbai, India), PEG 35 kDa (Sigma-Aldrich, St. Louis, MO, USA).

ENV Isolation by Differential Centrifugation

The plasma (1.5 mL) cleared from cellular debris and large protein complexes was mixed with phosphate buffered saline (PBS) in a ratio 1:1. ENVs were sedimented by ultracentrifugation according to the classical procedure [8], with minor modifications using an Optima XPN 80 ultracentrifuge (rotor 70.1 Ti/k-factor 36). Briefly, the 50% plasma solution (3 mL) was centrifuged at 110,000g for 2 h, the supernatant was removed, and the precipitate was dissolved in PBS (3 mL). The solution was centrifuged again at 110,000g for 2 h. The supernatant was removed, and the pellet was dissolved in 500μL of PBS.

ENV Isolation by a Two-Phase Polymer System

The polymers, PEG and dextran, were dissolved in plasma (1.5 mL) at the desired concentration. In parallel, the same quantities of polymers were dissolved in PBS (1.5 mL) to prepare aqueous mixture herein referred to as protein-depleting solution (PDS). Two tubes containing plasma and PDS were centrifuged at 1000 g for 10 min to speed up partition of polymer solutions into lower phase (LP1) and upper phase (UP1). To deplete LP1 with plasma protein, the upper phase (UP1) was replaced by PDS, and solutions were mixed and re-separated into LP2 and UP2 by centrifugation at 1000g for 10 min. To see the effect of the third re-separation, this procedure was repeated twice.

The sample measured in the present thesis was EV in PBS buffer isolated by the described protocol, with max concentration $3.2 \cdot 10^{11}$ particles per mL.

3.7.3. EV isolation from cell cultures

The protocol for EV isolation from cell culture medium by ultrafiltration was estimated by Chernyshev et al [173]. SKOV3 and 22rv1 cells were cultured in DMEM media with 10 % fetal bovine serum (FBS), 5 % L-Glutamine, 1 % sodium pyruvate, 1 % penicillin/streptomycin and 0.1 % gentamicin. Flasks with an area of ∼175 cm2 of each cell line were brought to a 90–100 % confluence and culture medium replaced with a medium lacking FBS 48 h before collecting for sEV isolation. The culture medium was transferred to a clean tube after 48 h and centrifuged at 300×g to remove dead cells that could be present in the suspension. The samples were then frozen and stored at −20 °C in clean 50 ml Eppendorf tubes. EVs were isolated by ultrafiltration (UF). Cell culture medium (∼70 mL volume per cell line) was centrifuged at 3000×g to remove aggregates. Purification and concentration of EVs was done by using Amicon™ Ultra Centrifugal 100 kDa UF filters. After concentrating the cell culture medium to 500 µL the tube used for filtration was filled with 1x DPBS and centrifuged again. The final samples containing purified EVs with about 500 µL volume each were used for characterization.

3.7.4. EV concentration estimation

For EV concentration estimation for all isolation methods, nanoparticle tracking analysis is used. The measurements were carried out with a Nanosight NS300 analyzer (Malvern Panalytical, Malvern, UK). The spectra were processed using Nanosight NTA 3.2 Software. Camera level: 14, shutter slider: 1259, slider gain: 366. Dilutions were made so that approximately 30–50 particles were observed in the field of view during video capture, corresponding to concentrations between ∼ 4×10^8 and 8×10^8 particles per mL. Each sample was pumped through the analyzer observation chamber to make 4–5 measurements at different microvolumes. Each measurement lasted 60 s, which corresponded to 1498 frames.

Chapter 4. Application of HC-MOW for Raman spectroscopy of liquid samples

In this chapter, the application of HC-MOW in Raman spectroscopy is described. For that, the analytes in the form of aquaeous solutions of two molecules were taken: a relatively small organic molecule R6G (479 Da[174]) and a much larger biological molecule BSA(66.5 kDa[175]).

This chapter is a combination of the material published by the author in two research articles:

a) In part with R6G, [88]**A.A. Merdalimova**, P.G. Rudakovskaya, T.I. Ermatov, A.S. Smirnov, S.S. Kosolobov, J.S.Skibina, P.A. Demina, B.N. Khlebtsov, A.M. Yashchenok, D.A. Gorin, SERS Platform Based on Hollow-Core Microstructured Optical Waveguide: Technology of UV-Mediated Gold Nanoparticle Growth. Biosensors, 2022, 12, 19. https://doi.org/10.3390/bios12010019 (IF=5.519, Q1). All Raman measurements and data curation was provided by the thesis author. [88]

b) A part with BSA, [169]**A. Merdalimova**, V. Vorobev, R. Barmin, A.Aleksandrov, D. Terentyeva, T. Estifeeva, S. German, V. Chernyshev, O. Maslov, Y. Skibina, P.Rudakovskaya, D. Gorin, Two-in-One Sensor of Refractive Index and Raman Scattering using Hollow−Core Microstructured Optical Fibers for Colloid Characterization. Colloids Surfaces B, 2023 (accepted, submission number COLSUB-D-23-02310). Raman measurement supervision and all data curation were provided by the thesis author, supported with measurements implemented by Artem Aleksandrov. [176]

4.1. Measuring Raman spectra of R6G solutions

Firstly, Raman spectra of 0.2 mM R6G aquaeous solution in a drop placed on a planar borosilicate glass substrate and in the HC-MOW were compared. The spectra are demonstrated in Figure 4-1. One may conclude that using HC-MOW enhances Raman intensity: R6G with concentration 0.2 mM is distinguishable using HC-MOW, while it wasn't on planar slides. If to calculate "waveguide analytical enhancement factor", taking into account signal amplitudes and concentrations, the formula is as follows:

$$EF = \frac{\frac{I_w}{c_w}}{\frac{I_{drop}}{c_{drop}}},$$ (4-1)

where I_w and I_{drop} are intensities of the same Raman peak of the analyte measured in a HC-MOW and in a drop, respectively, while c_w and c_{drop} correspond to their concentrations.

According to Equation (4-1), 50x enhancement for R6G was obtained. This may be explained by a larger effective volume of the analyte participating in Raman scattering due to waveguiding properties of HC-MOW. Meanwhile, the large height of liquid analyte in HC-MOW is provided by a sample volume of around 1.1 µL in the hollow core.
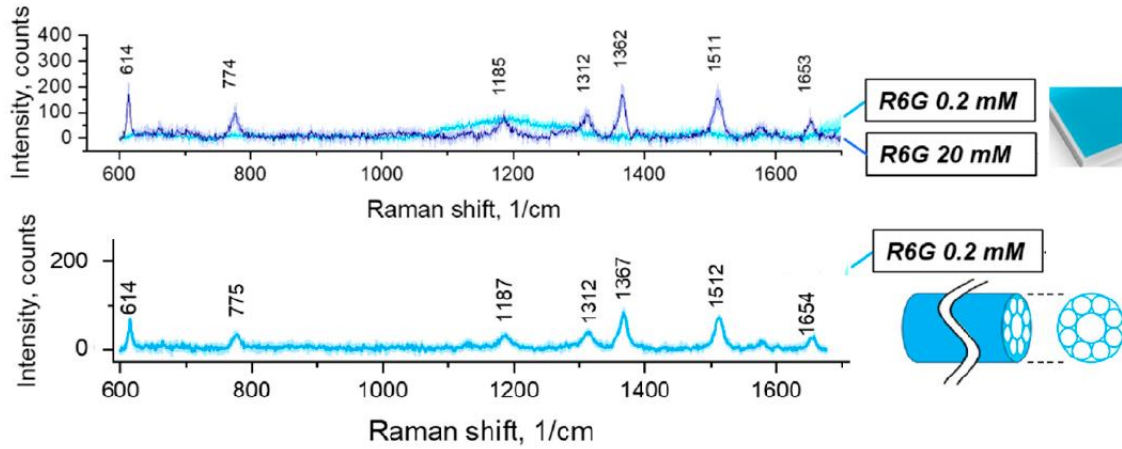
Figure 4-1. Raman spectrum of Rhodamine 6G (R6G) on a drop on a planar substrate and in the HC-MOW.

4.2. Measuring Raman spectra of BSA solutions

Another analyte taken to test HC-MOW performance is BSA protein, which is one of the simplest and popular model biological analytes. An aquaeous solution of BSA with the range of concentrations 5 – 100 mg/mL was taken. Compared to R6G, BSA possesses much greater molecular weight, and at concentrations applicable for optical sensing and close to physiological values (dozens of mg/mL) BSA is more dense and possesses greater refractive index, viscosity and is prone to drying on air, obtaining a crust on the surface.

75

Therefore, it is interesting to estimate HC-MOW performance for Raman sensing for such a different analyte and compare the results.

Unlike R6G, EF for BSA was extracted from the dependence of Raman peak intensity on BSA concentration. Such an approach was chosen to account for the greater variability of Raman peak intensities of BSA. The latter resulted from more active and irregular drying, which occurs directly during the signal acquisition.

Figure 4-2a demonstrates Raman spectra of BSA measured in the HC−MOW as presented in Figure 3-5. The registered Raman spectra peaks and their assignments according to the literature are presented in Table 4-1. A number of works referenced in the table confirm that the observed spectra belong to the protein. In selecting the peak that is best for simple univariate tracing, without additional peak shape fitting, the preferred one should possess a relatively high amplitude to avoid errors from noise. No nonlinear dependencies of the peak intensity on concentration should be known. Additionally, a narrow shape is preferred to avoid amplitude distortion during software-based background correction. Finally, a peak should not possess a spectral overlap with other peaks which don't meet the previous requirements. Based on these criteria, the peak at 1004 cm^{-1} was chosen, corresponding to phenylalanine ring breathing mode[177,178]. The dependence of the peak intensity on the BSA concentration and its linear approximation (later its choice is justified) is demonstrated in Figure 4-2b; the spectra from similar measurements in a bulk solution (in a 0.5µL tube) and a drop on a planar substrate are demonstrated in Figure 4-2c,d. The use of linear fitting was justified by the known linear dependence of Raman intensity on concentration (which is proportional to number of particles)[179].

It is worth noting that for the 1004 cm^{-1} peak intensities in cases of bulk solutions and drops (Figure 4-2c,d) no signal increase was detected until the concentration of BSA reached 20 mg/mL. ANOVA (Analysis of Variance) and further post-hoc testing (Tukey's
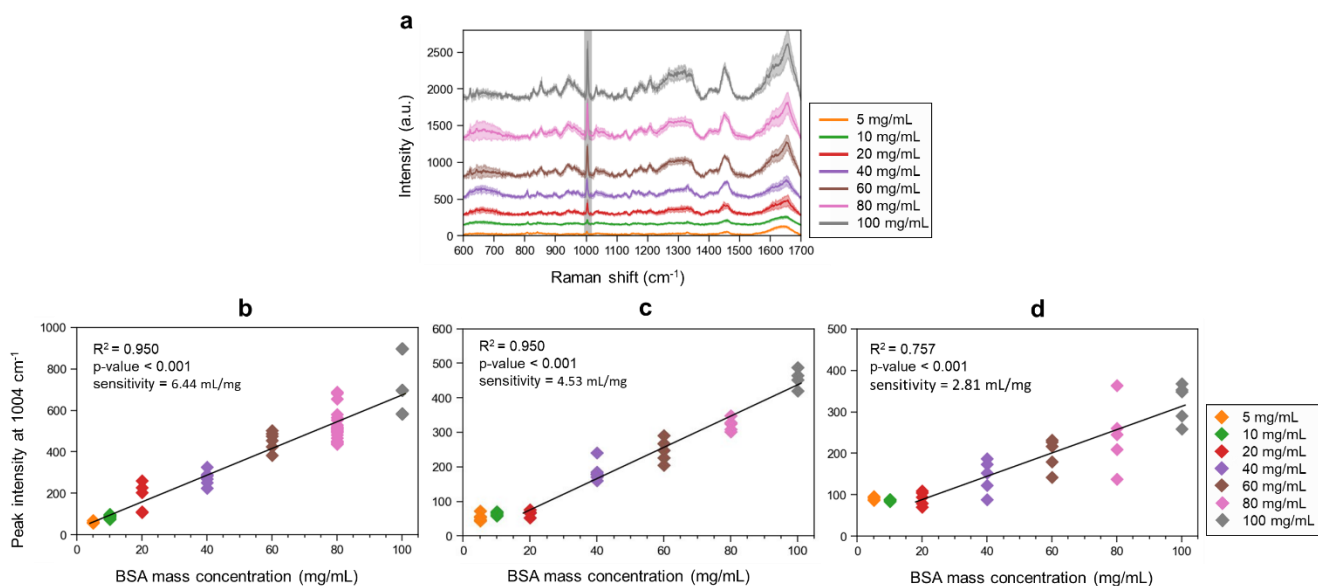
Figure 4-2. BSA monocomponent aquaeous solution Raman spectroscopy measurements: (a)Raman spectra measured in HC-MOW; (b-d) 1004 1/cm peak intensity dependencies on concentrations measured in: (b) in HC-MOW, (c) in a bulk solution, (d) in a drop on a planar substrate.

HSD (Honestly Significant Difference) showed that the null hypothesis could not be rejected when comparing the 5, 10, and 20 mg/mL concentrations, so the first two concentrations were not included in the linear fit. The obtained sensitivities for measurement in a bulk solution and in a drop on a planar substrate are 4.53 mL/mg and 2.81 mL/mg, respectively, demonstrating a higher sensitivity of Raman measurement in HC-MOW. Therefore, for these 2 ways of Raman measurements, only 20 mg/mL and higher concentrations are used to build linear fits.

As a result of building three linear fits (for points in Figure 4-2(b-d)) and their assessment, for all three line fittings, $p-value$ is less than 0.001, R^2 is 0.950 for HC-MOW and bulk solution, and R^2 is 0.757 for the drop. Thus, the Raman peak intensity linearly depends on concentration, analogously to RI dependence on concentration.As for the sensitivity of Raman peak intensity to concentration, which is determined by the line slope in Figure 4-2(b-d), it is 6.44, 4,53 and 2.81 for the measurements in HC-MOW, bulk BSA

solution and in a drop, respectively. Thus, the sensitivity achieved HC-MOW is 1.4x greater than in a bulk solution and 2.3x greater than in the drop.

Table 4-1. Raman peaks assignment for BSA monocomponent solution

Raman shift (cm^{-1})	Corresponding assignment	Reference
622	Phenylalanine phenyl ring breathing, Tyrosine C−S stretch	[177], [178], [180]
644	Tyrosine C−S stretch	[178,180]
830	Tyrosine, out−of−plane C−H bond motion	[177,180]
851	Tyrosine, in−plane ring breathing mode, Proline, C−C ring stretch	[177,180]
880	Tryptophan aromatic residue	[181]
942	C−C−N symmetric deformation, alpha−helical skeletal	[178,180]
1004	Phenylalanine, ring breathing mode	[178,180]
1030	Phenylalanine, CH_2−CH_3 bending, C−C vibration	[181]
1130	C−N stretch	[178,180], [182]
1210	Phenylalanine, Tyrosine: side chain (C_β−C_γ) stretch coupled with the in−phase motion of ($C_{\delta 1}$−$C_{\epsilon 1}$) stretch and ($C_{\delta 2}$−$C_{\epsilon 2}$) stretch	[178,180]
1240−1350	Amide III, peptide chain secondary structure, coupled C–N stretch and N–H bending vibrations of the peptide group	[177], [181]
1450	CH_2/CH_3 deformation	[178,180]
1656	Amide I, stretch vibration of C=O	[178,180]

4.3. Summary

Raman spectra of liquid analytes feature peaks of greater intensity when measured in a HC-MOW rather than in a 2 µL drop on a plain microscope glass slide. This is in agreement with the previously published works [16,183,184]. However, the enhancement in HC-MOW is different for different analytes. So, the enhancement up to 50 times (compared to a drop on a planar substrate) was demonstrated for R6G by introducing fiber enhancement, specifically using antiresonant HC-MOW as a cuvette. While for BSA just 2.3x enhancement was obtained. The difference may be explained by a number of factors, such as: the formation of BSA dried crust on the liquid (analyte)-air interface due to lengthy measurements; higher refractive index in the case of BSA solution (will be discussed further in the present thesis, in section 6.2) compared to R6G, which reduced the RI contrast between core and cladding, hence decreased reflection from the analyte-liquid interface on HC-MOW walls and finally ultimately reduced waveguiding efficiency.

However, HC-MOW demonstrated the ability for fiber enhancement, as expected. Compared to commonly used SERS, fiber enhancement is much lower (discussed in section 2.1.4),but still interesting for sensing as it hasn't SERS disadvantages of molecules distortion and very small vicinity of enhancement. Thus, using HC-MOW as a cuvette for Raman sensing is beneficial when a robust signal enhancement by several (dozens) times is desired. Therefore, the research on sensing in HC-MOW is continued, using Raman spectroscopy and combined it with other methods, as will be elaborated in further chapters.

Chapter 5. Investigating SERS substrates based on HC-MOW

The work described in this chapter aims at developing a novel approach for simplifying the preparation of SERS substrate inside HC-MOW. Firstly, a concept of the existing method of SERS substrate fabrication on glass slides was verified. The planar SERS substrates were fabricated by the author using a two-step UV-mediated chloroauric acid reduction on gold seeds and compared their SERS enhancement with the substrates made by one-step absorption of larger AuNPs. This comparison demonstrated the SERS scattering efficiency of the substrate produced with the developed two-step method. Then the technique was transferred to HC-MOWs. A method for SERS substrate deposition process control in HC-MOW was introduced, based on the change in its transmission spectra.

The results were published in **A.A. Merdalimova**, P.G. Rudakovskaya, T.I. Ermatov, A.S. Smirnov, S.S. Kosolobov, J.S.Skibina, P.A. Demina, B.N. Khlebtsov, A.M. Yashchenok, D.A. Gorin, SERS Platform Based on Hollow-Core Microstructured Optical Waveguide: Technology of UV-Mediated Gold Nanoparticle Growth. Biosensors, 2022, 12, 19. https://doi.org/10.3390/bios12010019 (IF=5.519, Q1). All surface modification, SERS measurements and data collection and processing were performed by the thesis author. [88]

5.1. SERS substrates on planar slides

5.1.1. Surface modification by plasmonic nanoparticles

Plasmonic nanoparticles for further SERS substrate fornation, namely gold nanoparticles, were fabricated as described in the subsection 3.5.2. TEM and DLS characterization of these two types of AuNPs are provided in Figure 5-1. According to DLS (Figure 5-1c), gold seeds have a mean diameter and standard deviation of 8.0 nm and 1.4 nm, respectively; the main fraction of AuNPs stabilized with citrate have a mean diameter and standard deviation of 33 nm and 11 nm, respectively. AuNPs stabilized with citrate also have a fraction with a size of around 1 nm, which is observed both on TEM and DLS.
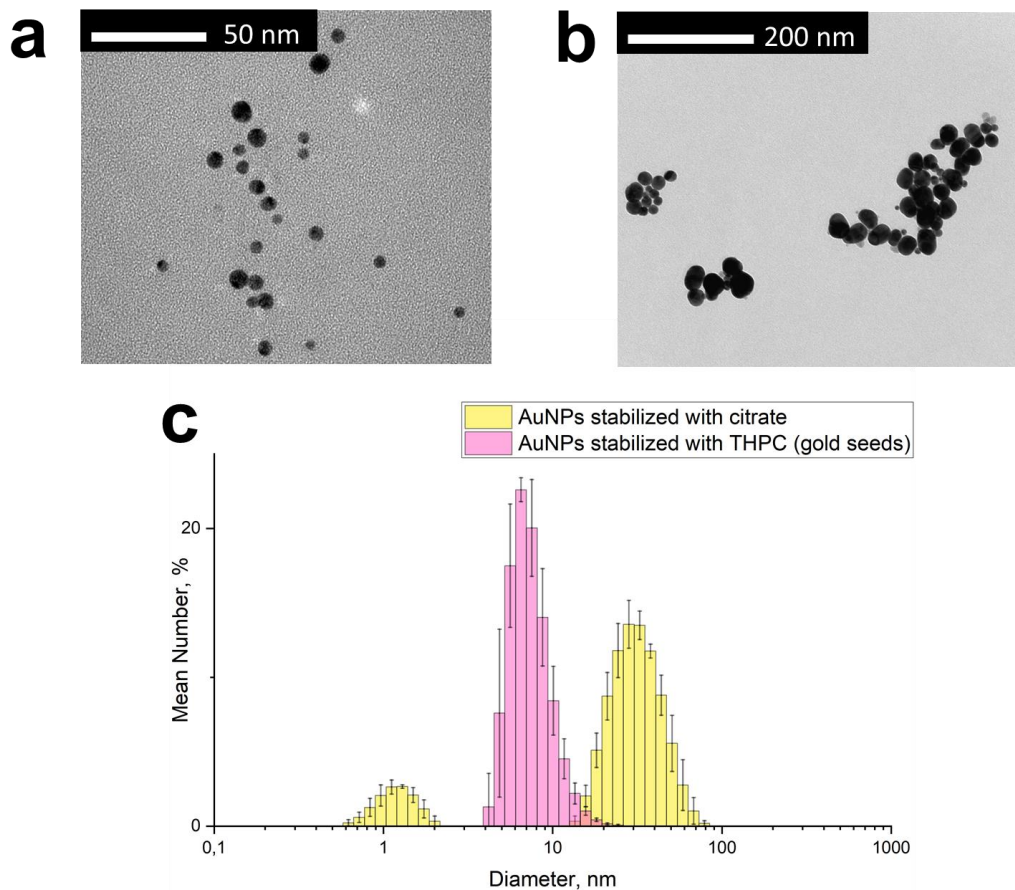
Figure 5-1. Characterization of AuNPs: (a) transmission electron microscopy (TEM) image of THPC gold seeds; (b) TEM image of AuNPs stabilized by citrate; (c) size distribution histogram of gold seeds stabilized by THPC (pink) and AuNPs stabilized with citrate (yellow), revealed by dynamic light scattering (DLS).

SERS substrates on planar microscope slides were fabricated as described in the subsection 3.5.4. As it can be noticed from SEM images incorporated into Figure 3-7, the sample Slide-Au-Seeds is covered with small AuNPs and in some places with their aggregates. The sample Slide-AuNP is covered with larger AuNPs with higher surface density, although gold mass concentration (mg/mL) is of the same order as in Slide-Au-Seeds. Meanwhile, taking into account particle sizes, the number concentration (1/mL) of the gold particles used is even less than for the sample Slide-Au-Seeds. After UV-mediated gold reduction, the obtained sample Slide-Au-UV exhibited a significant increase in the

size of gold nanostructures on its surface compared to the sample Slide-Au-Seeds before UV-mediated gold reduction.

The nanostructure dimensions should be in the subwavelength range, typically less than 100 nm. The best characteristics are expected for 30-50 nm structures. However, in the present, in Chapter 5, a coating of 30 nm particles provided much lower enhancement then the one made by a two-step process, with additional gold reduction on smaller (ac. 8 nm) seeds. Also, to maximize SERS, it is crucial to have plasmonic enhancing hotspots, which are typically located at the apex of nanostructures or where two nanoparticles are in close proximity to each other.

The next subsection provides the comparison of Raman and SERS spectra on the developed substrates by peak intensities and enhancement factor calculations.

5.1.2. SERS measurements on the SERS substrates on planar slides

R6G was used as a Raman reporter [185–187]: 2 µL of 0.2 mM R6G aqueous solution was placed by drop casting on the substrates described in the previous subsection.

The comparison between SERS peak intensities measured on these substrates and Raman peak intensities is provided via an analytical enhancement factor (EF) calculation [188]:

$$EF = \frac{\frac{I_{SERS}}{c_{SERS}}}{\frac{I_R}{c_R}}, \qquad (5\text{-}1)$$

where c_R and c_{SERS} are R6G concentrations during Raman (on a bare substrate) and SERS measurements, and I_R and I_{SERS} are peak intensities, respectively.

For a general EF estimation for the substrates, Raman modes at 1362 and 1509 cm^{-1} were used, as they correspond to benzene ring stretching and are the most prominent ones. The sample Slide-Au-Seeds didn't demonstrate any signal from 0.2 mM R6G. The sample Slide-AuNP demonstrated EF around $0.8*10^3$, while, the sample Slide-Au-UV demonstrated EF $= 1.3*10^4$.

Therefore, UV-mediated chloroauric acid reduction on gold seeds demonstrated its potential in improving SERS signal by 16 times, and this approach was adopted to HC-MOW, due to the ability of HC-MOW to additionally increase Raman signal [15,189,190].
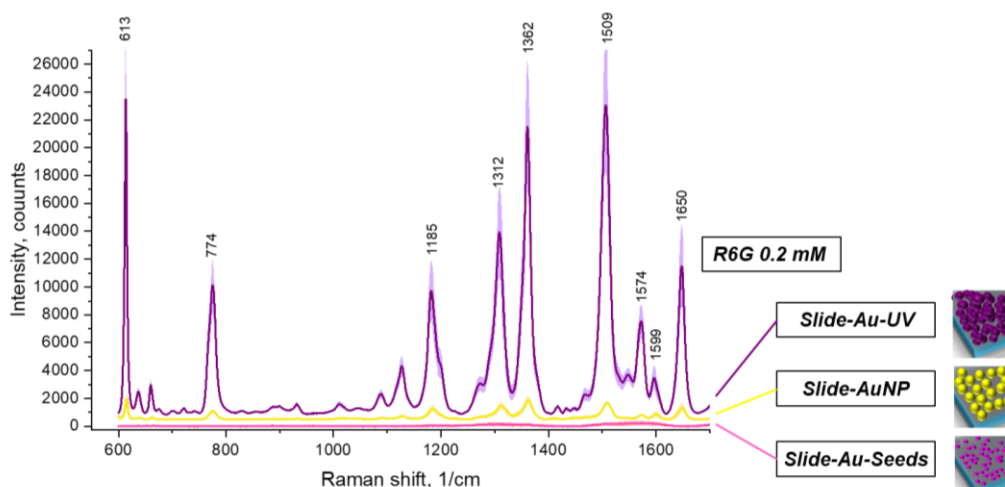
Figure 5-2. SERS of 0.2 mM Rhodamine 6G on planar plasmonic substrates.

5.2. SERS and layer deposition control in HC-MOW

The fabrication of SERS-active HC-MOW samples is described in subsection 3.5.5 and illustrated in Figure 3-8. SEM images of the HC-MOW tip at different steps of the functionalization incorporated into Figure 3-8 allow to see the step-by-step growth of the plasmonic substrate (further referred as coating) on HC-MOW walls**.**

While developing a novel technique for SERS substrate formation inside HC-MOW (compared to the known techniques of SERS substrate formation in HC-MOW), it is needed to evaluate coating performance. Layer deposition control using SEM images has several disadvantages. One image provides information about just one cross-section at the moment, on the examined waveguide tip. Thus, the SEM imaging of the tip is not representative and HC-MOW need to be broken up for coating control. Beside that, SEM equipment is expensive, its usage is laborious and requires special skills, and is not routinely available. Furthermore, since most of the commercial waveguides are made of silica or silica glasses, an extra deposition of metals required for the proper imaging

decreases the contrast between waveguide walls and functional coating and does not allow resolving nanometer-thin films [191]. The optical setup for transmission spectra measurement of HC-MOWs [14] solves this problem: spectral data provide integral (averaged on the waveguide length) information about HC-MOW geometry. Moreover, this optical setup is quite compact, can be quickly assembled using common optical components, and is simple to use. The spectral positions of antiresonances, i.e. the minimum transmission wavelength, depend on wall thickness and refractive index, as remonstrated in Equation 3-1. Thus, coating formation on HC-MOW inner walls provides spectral shifts in these minima positions.

Figure 5-3a demonstrates transmission spectra for a single HC-MOW at all stages of the surface functionalization. For quantitative analysis, the positions of minima min1...min4 were chosen in the 450-800 nm range, as the minima outside this range possess lower signal-to-noise ratios, which may affect the accuracy of determining the positions of the minima.
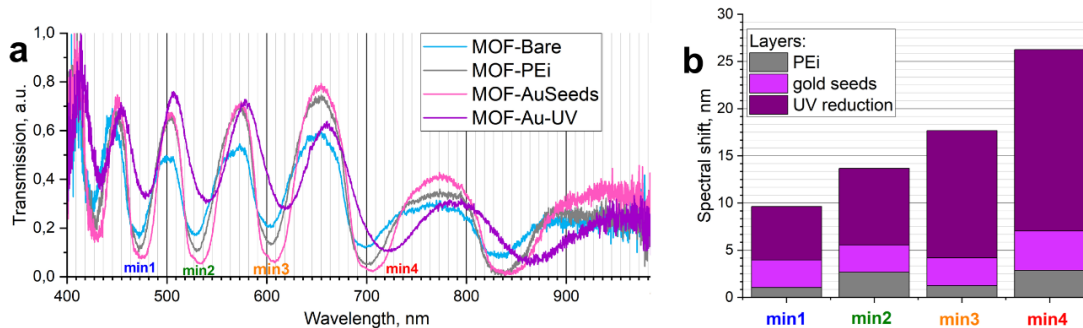
Figure 5-3. Shifts in transmission spectra induced by coatings: (a) transmission spectra of a single HC-MOW at all stages of layer deposition, with positions of minima selected for analysis labeled as min1...min4 ; (b) shifts in transmission spectra induced to 1 waveguide cumulatively by PEi, gold seeds, and UV-mediated chloroauric acid reduction.

In Figure 5-3b, the shifts in positions of transmission minima are presented for all stages of layer deposition. It is worth noting that these shifts depend on additional optical path lengths experienced by a divergent beam inside the HC-MOW, and the optical path

length depends both on refractive index and layer thickness. However, with wavelength increasing, the distance between minima becomes greater in a single spectrum, and the same optical path lengths lead to greater shifts in transmission spectra. This phenomenon compensates (and even overcompensates) the fact that the refractive index of gold in the visible range is mainly decreasing with increasing wavelength [192].

A Raman spectrum of R6G in a bare HC-MOW and a SERS spectrum in a functionalized HC-MOW (i.e., with the SERS substrate discussed in the subsection are presented in Figure 5-4. According to the Equation 5-1, the functionalized HC-MOW demonstrates SERS enhancement with an EF = 10. This value is lower than for the SERS substrate fabricated on planar slides using the same method. The main author's suggestion for this fact is that although the SERS substrate area exposed to laser irradiation in HC-MOW is greater than that of the planar substrate, the efficiency of scattering signal collection by an objective is lower in the case of HC-MOW. Nanostructured gold coating on inner waveguide walls does not only enhance Raman scattering signal but scatters
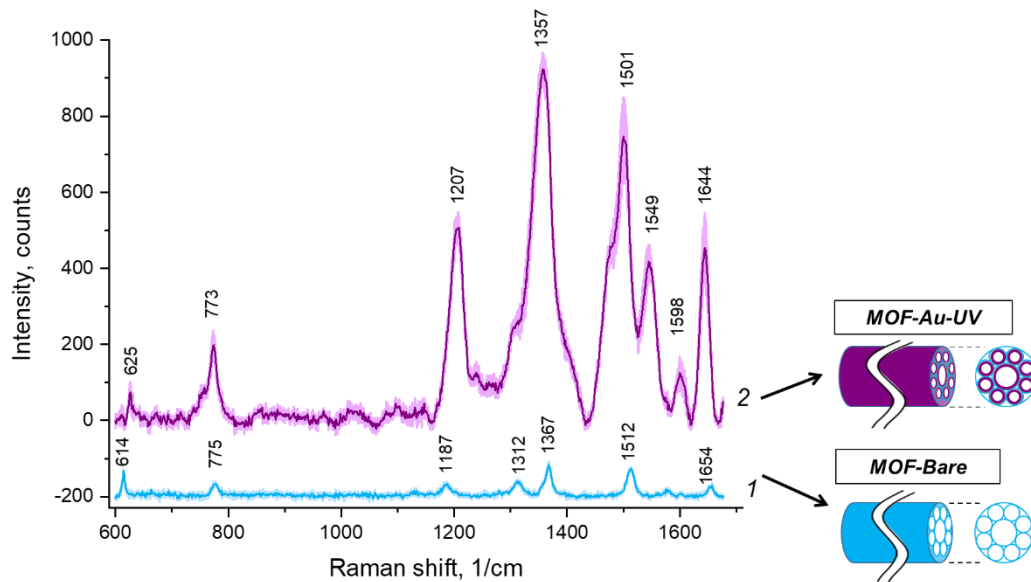
Figure 5-4. Raman and SERS of R6G in HC-MOW: 1 – bare HC-MOW; 2 – HC-MOW with UV-mediated chloroauric acid reduction on gold seeds.

incident radiation in multiple directions at the same time. Therefore, compared to the illumination of planar substrates, a smaller part of the generated Raman scattering signal from the liquid analyte is collected by the Raman spectrometer. This problem may be solved by placing a mirror on the waveguide end opposite to the illumination and signal collection side. Further improvement of the technique of gold deposition in HC-MOW is recommended. In particular, the developed UV-mediated gold reduction in HC-MOW could be combined with further annealing[193].

It is worth noting in Figure 5-4 that the Raman shifts of R6G are different with and without SERS substrates, and the enhancement factors for different peaks are different. Moreover, when SERS enhancement in HC-MOW (Figure 5-4) and SERS enhancement on a planar substrate is compared (Figure 5-2), it turns out that these two SERS substrates enhance different modes by different values. The way of R6G interaction with gold surfaces [194] matters: it is a complex process and may be influenced by a number of conditions such as the surface of the nanoparticles and the interaction of R6G molecules. Considering SERS enhancement of particular bonds related to R6G orientation, several factors should be taken into account:

1) According to surface selection rules, molecule vibrations with transition dipoles (and hence bonds) directed tangentially to the metal surface should have decreased amplitude; meanwhile, molecule vibrations with transition dipoles directed perpendicular to the metal surface should have augmented amplitude [195]. On both SERS substrates, the peak at 773 1/cm possesses relatively low SERS enhancement. This peak belongs to out-of-plane (the only one among the observed peaks) bending and methyl group [196]. R6G molecule contains nitrogen, and gold-nitrogen bonding is strong [197], thus the author assumes that the R6G molecule binds to gold surface via nitrogen in such a way that the methyl groups turn to be having a less angle with the gold surface than the xanthene plane.

2) From another point of view, the distance between the SERS surface and the certain enhanced bond is of crucial importance, as SERS intensity is proportional to the inverse fourth power of this distance. Thus, xanthene in-plane modes

86

(demonstrating high enhancement) may be located closer to the gold surface compared to the mentioned methyl groups. E.g., UV-mediated surface is hydrophilic, meanwhile CH3 groups on R6G are hydrophobic and therefore tend to run away from the surface, that may lead to decrease of corresponding peak (773 1/cm) enhancement compared to others. Also, stabilizing agents play a role.

3) Finally, before peak intensity assessment, polynomial background extraction is applied, which may adjust the values of peak intensities.

5.3. Summary

A method of a two-step fabrication of SERS substrates in HC-MOW using UV-mediated growth of gold nanoparticles and layer deposition control was verified. Due to HC-MOW spectral response in light transmission, the progress of nanostructure growing on HC-MOW inner walls may be monitored.

HC-MOW functionalized with gold nanostructures demonstrates SERS enhancement with EF around 10. It is lower than in the case of SERS-active substrate fabricated on planar microscope slides using the same method ($1.3*10^4$). The main author's suggestion for this fact is that although the SERS substrate area reached by laser irradiation in HC-MOW is greater than on planar substrate, the efficiency of collecting scattered light by an objective is lower in this case. Nanostructured gold coating on inner waveguide walls does not only enhance Raman scattering signal but in the same line scatters incident radiation in multiple directions. Therefore, compared to the illumination of planar substrates, a smaller fraction of the generated signal (only backscattered to objective aperture) is collected by the Raman spectrometer. This problem may be solved by placing a mirror on the HC-MOW end opposite to the illumination and signal collection side.

Furthermore, HC-MOW transmission spectra, with both SERS coating and the liquid analyte inside, may be taken into account, and optimal wall thickness found for maximization of Raman scattering collection. Also, further improvement of the developed technology of gold deposition to HC-MOW may be provided. In particular, the developed UV-mediated gold reduction in HC-MOW could be combined with further annealing[193].

87

However, it is worth noting that the UV gold reduction possesses stable adhesion on glass slides, meanwhile in HC-MOW the adhesion stability is poor. Therefore, further investigations should be made to gain a stable SERS substrate grow in HC-MOW.

Also, for further investigations is worth noting that transmission/absorption spectra of SERS substrates would provide valuable information on plasmonic resonances taking place in plasmonic nanostructures and thus proving that SERS effect takes place.

Chapter 6. Two-in-one sensing of refractive index and Raman scattering of colloids in HC-MOW

In this chapter, the methods of multispectral refractive index and Raman scattering sensing in HC-MOW are combined, and used not only for one-component homogeneous solutions, but also for colloidal solutions.

The results were presented in the paper A. Merdalimova, V. Vorobev, R. Barmin, A.Aleksandrov, D. Terentyeva, T. Estifeeva, S. German, V. Chernyshev, O. Maslov, Y. Skibina, P.Rudakovskaya, D. Gorin, Two-in-One Sensor of Refractive Index and Raman Scattering using Hollow−Core Microstructured Optical Fibers for Colloid Characterization. Colloids Surfaces B, 2023 (accepted, submission number COLSUB-D-23-02310). Raman and RI measurements, data collection and processing were performed were provided by the thesis author, with analytes synthesized by the team of T.Estifeeva, D.Terentyeva, O.Maslov headed by P.Rudakovskaya; the scripts for RI calculation were developed by the thesis author and V.Vorobev. [176]

6.1. Two-in-one measurement in HC-MOW

The combination of multispectral RI sensing and Raman spectroscopy in HC-MOW is depicted in Figure 6-1.

The RI of the solution inside the HC−MOW can be determined from the position of the minimum in the transmission spectrum of the filled waveguide, the thickness of the glass, its RI, and the capillary mode order. The setup for multispectral RI sensing is schematically presented in Figure 6-1a. Its work principle is described in detail in section 3.3. The right inset graph in Figure 6-1a highlights periodical transmission pattern of the HC−MOW for both substances but possessing different positions of transmission minima and different intensity patterns for these two substances.

The setup designed for Raman scattering is presented in Figure 6-1b and described in detail in subsection 3.4.4. In contrast to RI measurement, here the input spectrum is a

monochromatic high power density laser, and the output measures is Raman spectrum as a complex of new spectral components in scattering.
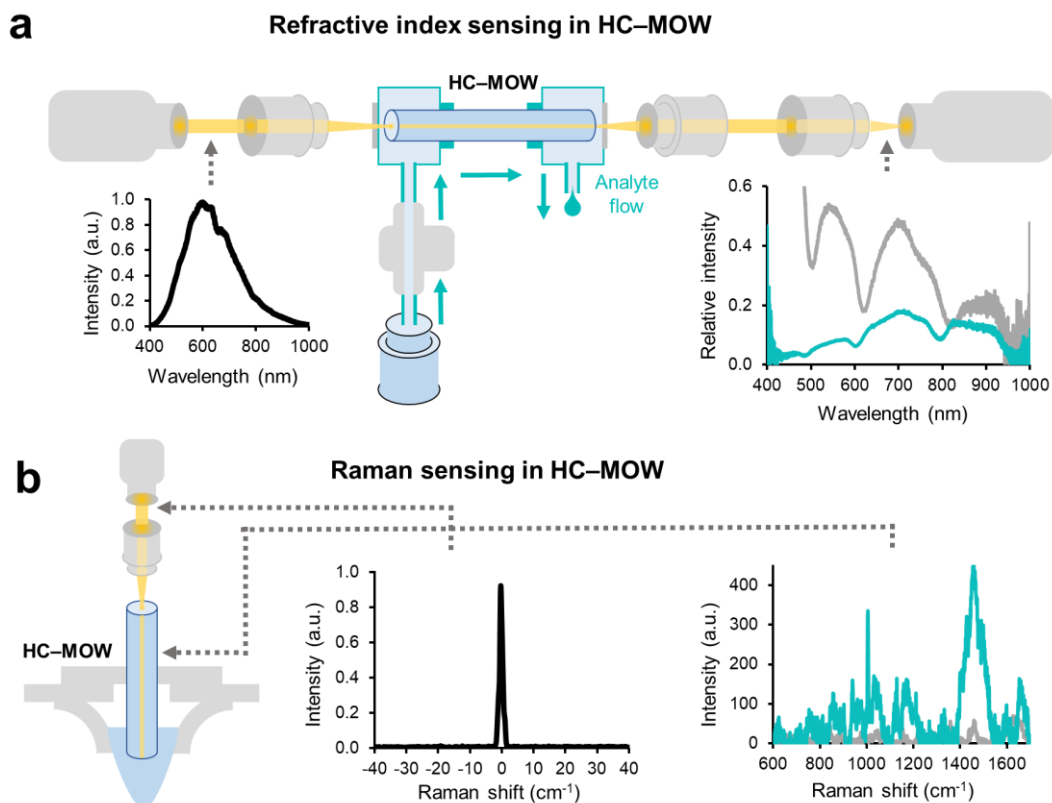
*Figure 6-1. Scheme of the HC−MOW setup for two−in−one refractive index and Raman scattering measurements of analytes. (**a**) A setup for transmission measurement and RI sensing in a HC−MOW. The left incorporated graph corresponds to light source spectrum, the right graph corresponds to light spectrum after the HC−MOW (grey line for aqueous solution and cyan line for BSA@P(VP−AA) [3:1] complex). (**b**) A setup for Raman scattering measurement in a HC−MOW. Initial narrow−band laser irradiation is depicted on the left plot, and Raman scattered signal is depicted on the right plot, grey line for aqueous solution and cyan line for BSA@P(VP−AA) [3:1] complex.*

Back to RI estimation, the experimental measurements conducted by the author in order to determine the wavelength of the minimum, revealed an approximate error of 2 nm

or less. According to Equation (3-3), this error translates to the minimum deviation of the RI value that can be detected using this method being approximately 0.001.

As for RI sensitivity, the calculations are made based on Equation (3-4), and Figure 6-2 illustrates RIS evaluations for a set of capillary mode orders $j = 5, 4, 3$, which correspond to wavelength minima positions further referred to as *min 1, min 2, min 3*. In the RI range used in the present work (450-800 nm), RIS value turns out to be around 2000 nm / RIU, which is consistent with optical RI sensors described in the literature[198,199]. Higher values, such as tens of hundreds of nm/RIU, are reported for waveguide SPR sensors, interferometer sensors and others setups[198], however, they are more expensive and involve additional complicated fabrication steps compared to the design described in the present work. While, the presented sensor based on HC−MOW is simple to design and inexpensive, yet the error of concentration measurement on it (as will be demonstrated in the further text) is less than ± 5 mg/mL, which is appropriate for certain non−demanding applications where the possibility of in−flow real-time measurement is in the first place.
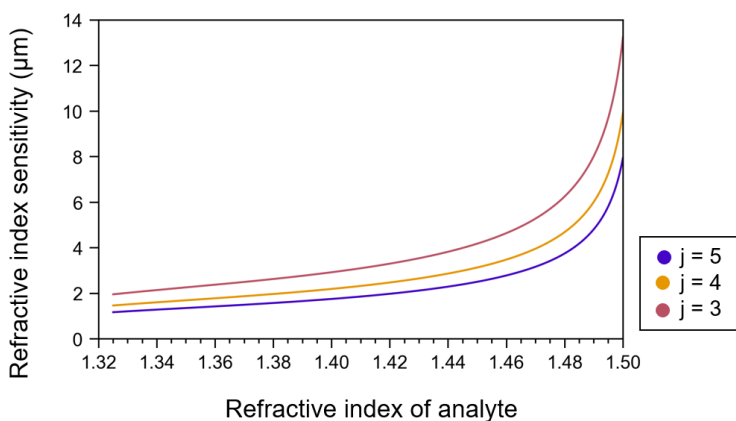
Figure 6-2. Refractive index sensitivity: analytical dependence of the wavelength derivative on the refractive index of analyte for a set of capillary mode orders j.

6.2. BSA and P(VP-AA) bulk solutions two-in-one measurement in HC-MOW

To assess the two−in−one RI and Raman sensing capabilities of the HC−MOW setup, refractive index and Raman spectra for BSA and P(VP−AA) monocomponent solutions

are measured for a number of different concentrations. The measurements presented below in this section are provided according to the concept demonstrated in Figure 6-3, combining the setups described in subsections 3.3.2 and 3.4.4.

6.2.1. BSA two-in-one measurement in HC-MOW

Figure 6-3a shows transmission spectrum of a bare HC-MOW. Figure 6-3b shows transmission spectra of BSA monocomponent solutions measured with the HC−MOW. To calculate RI values as described in subsection 3.3.3, firstly a transmission spectrum of an empty HC−MOW is used to estimate the particular wall thickness d for an individual waveguide. The obtained thickness values are $1.8 − 2$ μm, which is consistent with the estimation from scanning electron microscopy images. Furthermore, with the calculated precise value of the wall thickness, the same Equation (3-1) is used for RI estimation of liquid solutions introduced into the waveguide based on the transmission spectra. The obtained values are presented in Figure 6-3c. As the wavelength increases from *min* 1 to *min* 3, the RI values decrease, which is consistent with a typical dielectric dispersion curve in the visible optical region[200,201].

For each minimum, RI dependence on concentration is approximated using a linear regression. While it's a dielectric constant that is proportional to volume concentration[202], the Pearson correlation[203] coefficient between refractive index and concentration (0 - 60 mg/mL equals to volume fraction 0 - 0.106) is 0,99998928. Thus, with a linear fit, for all three minima R^2 values are 0.999 and *p−values* are less than 0.05 (with the highest value of 0.003) were obtained, so the RI dependence on concentration may be considered as linear and statistically significant for all three regions. Therefore, the present method is applicable for indirect concentration measurement: with RI of the unknown concentration measured, and with the calibration curve measured beforehand (like one demonstrated in Figure 6-3), one can extract the information about concentration.
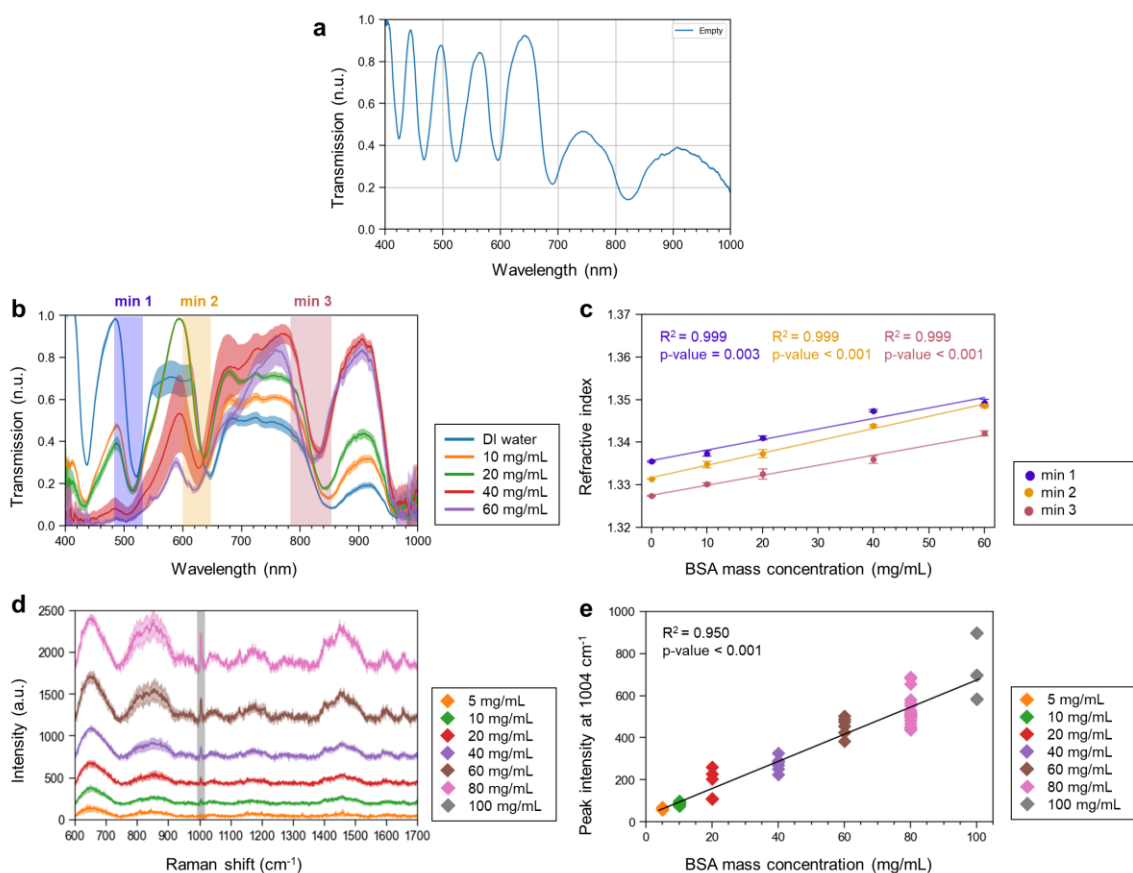
Figure 6-3. BSA monocomponent solution RI and Raman spectroscopy measurements. (a) Transmission spectrum of a bare HC-MOW. (b) Transmission spectra of HC−MOW with BSA aqueous solutions with concentrations of 10, 20, 40, and 60 mg/mL compared to DI water demonstrate 3 spectral regions (min 1, min 2, min 3) with anti−resonance minima positions, that can be used to extract RI values. (c) Linear dependence of the corresponding RI values of BSA aqueous solutions extracted from the 3 anti−resonance minima positions on the BSA mass concentration. (d) Raman spectra of HC−MOW with BSA aqueous. (e) Linear dependence of the corresponding Raman peak intensities at 1004 cm^{-1} Raman shift of BSA aqueous solutions.

According to the built linear regressions, the sensitivity of RI sensing to concentration may be found as a line slope for the built linear fits:

$$Sensitivity_{\lambda min_j} = \frac{\Delta n(\lambda_{min_j})}{\Delta c} \left[RIU \cdot \frac{mL}{mg} \right] \qquad (6\text{-}1)$$

where Δc is change in analyte concentration, and $\Delta n(\lambda_{min_j})$ is change in refractive indices on the wavelength minimum of *j*th order. Thus, the sensitivities to concentrations are $2.47 \cdot 10^{-4}$ RIU $\cdot$ mL/mg, $2.88 \cdot 10^{-4}$ RIU $\cdot$ mL/mg, and $2.35 \cdot 10^{-4}$ RIU $\cdot$ mL/mg for *min 1*, *min 2*, *min 3*, respectively.

As was mentioned earlier in this subsection, the minimum deviation of refractive index that can be detected is 0.001 RIU. Therefore, the Equation (6-1) now may be used to extract concentration change. Thus, maximum error of BSA concentration determination is 4.25 mg/mL. As was mentioned in subsection 6.1, this is not ultimately the best possible error, but still the present method has an advantage of in-flow real-time point-of-care measurement and the precision may be improved by using several waveguides with slightly shifted minima positions, as was demonstrated by Ermatov et al. [14]

Figure 6-3d demonstrates Raman spectra of BSA monocomponent solutions measured in the HC−MOW. Raman spectra peak assignments for BSA are presented in Table 4-1. Similarly to section 4.1, BSA Raman peak at 1004 cm^{-1} is chosen. The dependence of the peak intensity on the BSA concentration and its linear approximation is demonstrated in Figure 6-3e. For the line fitting, R^2 is 0.950 and *p−value* is less than 0.001, so the Raman peak intensity linearly depends on concentration, analogously to RI dependence on concentration. The slope of the fitted line corresponds to a sensitivity of 6.44 arb.u.·mL/mg for BSA in HC-MOW. However, based on points in Figure 6-3e, it is evident that Raman peak intensity deviations vary across different concentration points and do not fall below +- 10 mg/mL. Consequently, using the Raman "calibration curve" as a means of calibration is not recommended.

6.2.2. P(VP-AA) two-in-one measurement in HC-MOW

Similarly to BSA, RI and Raman spectroscopy measurements for P(VP−AA) are provided in Figure 6-4. Figure 6-4a shows transmission spectra of P(VP−AA) monocomponent solutions measured in the HC−MOW setup presented in Figure 6-1a. For RI extraction, wavelength positions corresponding to transmission minima are determined and named *min 1*, *min 2, min 3*, corresponding to wavelength ranges around 500, 600, 800

nm and capillary mode orders 5, 4, 3, respectively. RI for these wavelengths are calculated according to Equation (6-1) and presented in Figure 6-4b. For each minimum, RI dependence on concentration is approximated with a linear regression. For all three minima, R^2 values are 0.999 and $p-values$ are less than 0.001, so the RI dependence on concentration is linear and statistically significant for all three regions. Therefore, the present method is applicable for indirect P(VP−AA) concentration measurement.

Analogously to calculations for BSA, based on Equation (6-1), and according to the built linear regressions, the line slopes are 2.21×10^{-4} RIU × mL/mg, 2.08×10^{-4} RIU ×
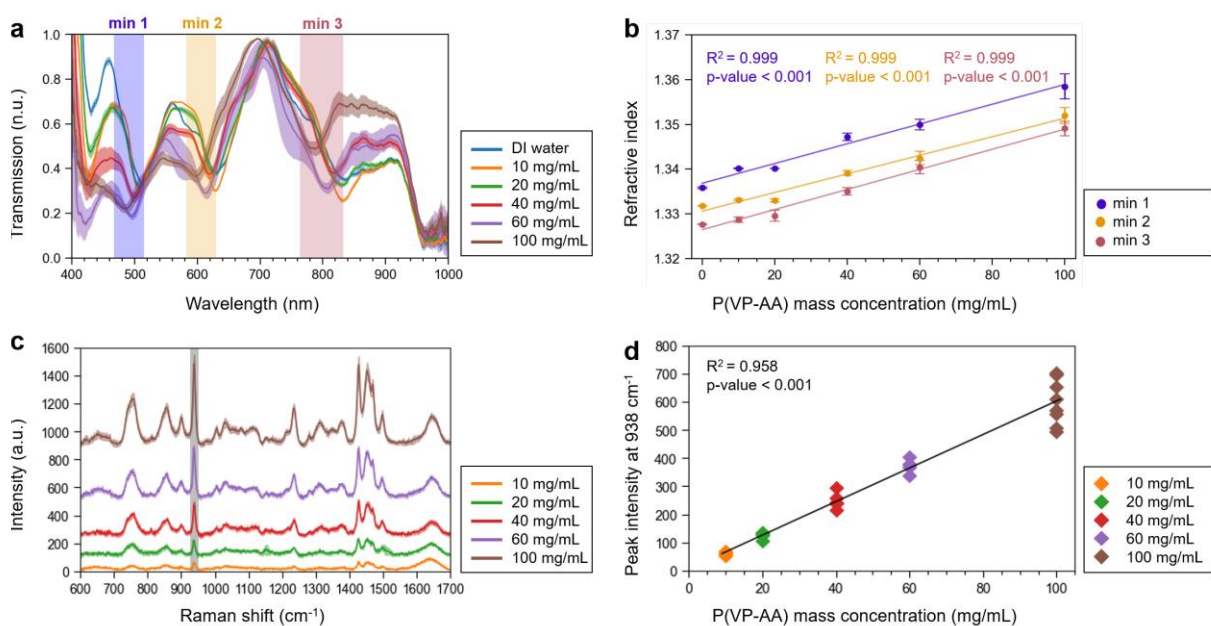
*Figure 6-4. P(VP−AA) monocomponent solution RI and Raman spectroscopy measurements. (**a**) Transmission spectra of HC−MOW with P(VP−AA) aqueous solutions with concentrations of 10, 20, 40, 60 and 100 mg/mL compared to DI water demonstrate 3 spectral regions with anti-resonant minima positions (min 1, min 2, min 3), that can be used to extract RI values. (**b**) Linear dependence of the corresponding RI values of P(VP−AA) aqueous solutions extracted from the 3 anti-resonant minima positions on the P(VP−AA) mass concentration. (**c**) Raman spectra of HC−MOW with P(VP−AA) aqueous solutions provide a set of characteristic Raman peaks. (**d**) Linear dependence of the corresponding Raman peak intensities at 938 cm⁻¹ Raman shift of P(VP−AA) aqueous solutions on the P(VP−AA) mass concentration.*

mL/mg, and 2.25×10^{-4} RIU × mL/mg for *min* 1, *min* 2, *min* 3, respectively, that corresponds to maximum 4.8 mg/mL deviation of concentration of P(VP−AA). Thereby, both BSA and P(VP−AA) demonstrated linear dependence of the measured refractive index on concentration, with deviation below 5 mg/mL.

Figure 6-4c demonstrates Raman spectra of P(VP−AA) monocomponent solutions measured in the HC−MOW presented in Figure 6-1b. A full table of peak assignments for P(VP−AA) is provided in Table 6-1.

The dependence of the peak intensity at 938 cm^{-1}, as the one most satisfying the criteria, on the P(VP−AA) concentration and its linear approximation is demonstrated in Figure 6-4d. For the line fitting, R^2 is 0.958 and *p−value* is less than 0.001, so in the measured range of concentration the Raman peak intensity linearly depends on concentration, similarly to RI dependence on concentration and to dependencies obtained for BSA. The slope of the fitted line corresponds to a sensitivity of 6.11 arb.u.·mL/mg for P(VP−AA) in HC-MOW.

Having information on both transmission spectrum of HC-MOW with the analyte and the analyte's Raman scattering in HC-MOW, the optimal transmission of HC-MOW for its application in Raman spectroscopy is an intriguing topic to explore. Here, a number of factors should be taken into account. Maxima in transmission spectra allow maximum length of light guidance. Meanwhile, with laser excitation at 633 nm, standard Raman range 600-1700 cm^{-1} corresponds to 657-709 nm wavelength range. Therefore, if the Raman range is around the maximum of HC-MOW transmission spectrum, then laser excitation is around the transmission minimum (which is exactly our case) and *vice versa*. This fact gives rise to an idea on further research in this two-in-one sensing, with numerical simulations and experiments on optimizing HC-MOW wall thickness for liquid analytes with given refractive indices.

Table 6-1. Raman peaks assignment for P(VP−AA) monocomponent solution.

Raman shift (cm^{-1})	Corresponding assignment	Reference
754	C−C stretch	[204], [205], [206]
856	C−C ring	[204], [207]
901	C−O vibration	[208]
938	C−C ring breathing; C−C stretch	[204], [206],[207]
1032	C−N stretch	[206], [208]
1234	C−H bending in the acrylic acid unit	[208], [209]
1310	C=O vibration	[208]
1428	Pyrrolidone ring (CH$_2$ scissor)	[204]
1455	In−plane OH bending	[204], [208]
1497	Pyrrolidone ring (CH$_2$ scissor)	[204], [210]
1642	C=O pyrrolidone stretching vibration	[210]

6.3. BSA@P(VP-AA) colloid structures

The next step of the research is two−in−one characterization of multicomponent colloid systems of BSA and P(VP−AA), highlighting the ability to extract RI values in a set of spectral regions and observe characteristic Raman peaks of each compound. RI values and considered Raman peaks have linear dependence on component concentration. Next, the capabilities of two−in−one characterization for BSA@P(VP−AA) nano−sized complexes and micron−sized MB (made of these complexes) are evaluated.

The process of BSA@P(VP−AA) complexes and MB synthesis is described in subsection 3.6. Briefly, all complexes and MB used in the present work are produced at the total mass concentration of 50 mg/mL as the optimal concentration for MB synthesis.

After the synthesis, [3:1] MB demonstrated a higher mean diameter of 4.7 μm, compared to moderate values of 3.2 μm for [5:1] MB and 3.0 μm for [10:1] MB. The MB concentration is ranging from $(2.0 \pm 0.5) \times 10^8$ MB/mL for [3:1] MB to $(1.0 \pm 0.4) \times 10^{10}$ MB/mL for [10:1] MB. Observed trends are consistent with the previous report[147].

Figure 6-5 demonstrates extinction spectra of BSA@P(VP−AA) complexes (Figure 6-5a-c) and MB made of them (Figure 6-5d-f). Extinction spectra of complexes demonstratr the absence of absorbance for the complex in the visible wavelength range. In contrast, a significant light scattering is observed for air−filled MB in the same spectral range, that can be analyzed by the Lorenz−Mie theory[211]. However, both spectra demonstrate that the BSA characteristic peak at 280 nm, confirming the presence of BSA in both systems[212,213]. Similar observations can be found for all produced complexes and MB with protein: copolymer ratios of [3:1], [5:1] and [10:1] at sets of different total mass concentrations, as presented in Figure 6-5.

Raman spectra of the obtained BSA@P(VP−AA) complexes and corresponding MB are presented in Figure 6-6. In Figure 6-6a, high concentrations are evaluated: 91 mg/mL for P(VP−AA) monocomponent solution, 250 mg/mL for BSA monocomponent solution, and 273 mg/mL: 91 mg/mL for BSA@P(VP−AA) [3:1] complex, respectively. Therefore, clear Raman peak designation is observed, and Raman fingerprint of BSA@P(VP−AA) in a 3:1 complex represents peaks from both BSA and P(VP−AA). In Figure 6-6b, all BSA@P(VP−AA) complexes and MB have total mass concentration of 50 mg/mL, leading to lower Raman signal intensities compared to Figure 6-6a, and reduced signal−to−noise ratios.

In all BSA@P(VP−AA) complexes and MB with total mass concentration of 50 mg/mL, a bright peak of phenylalanine in BSA at 1004 cm^{-1} can be clearly found, meanwhile the mentioned P(VP−AA) peaks at 938, 1234, 1428 cm^{-1} possess reduced intensity. This phenomenon can't be caused by a simple prevalence of BSA molecules
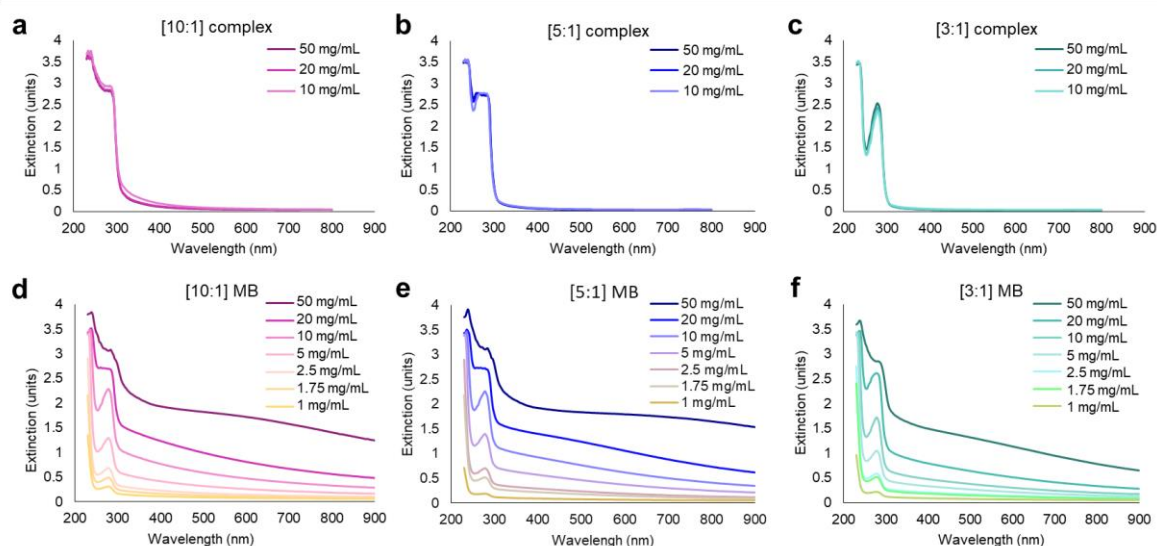
Figure 6-5. Extinction spectra for BSA@P(VP−AA) complexes and corresponding BSA@P(VP−AA) MB at sets of total mass concentrations. (a) BSA@P(VP−AA) [10:1] complex, (b) BSA@P(VP−AA) [5:1] complex, (c) BSA@P(VP−AA) [3:1] complex. All complex aqueous solutions are measured at a set of total component mass concentrations of 50, 20 and 10 mg/mL derived from the intact complex solution. (d) BSA@P(VP−AA) [10:1] MB, (e) BSA@P(VP−AA) [5:1] MB, (f) BSA@P(VP−AA) [3:1] MB.

presence on the surface, as the BSA and P(VP-AA) molecules are uniformly distributed in space. Therefore, this fact may be explained by a number of interaction factors. For peaks at 938 and 1428 cm^{-1}, related to pyrrolidone ring, this could be explained by steric complementarity and additional van der Waals bonds between P(VP−AA) and BSA[214]. It is worth noting that such P(VP−AA) peak intensity decrease is observed mainly at low mass percentages of P(VP-AA), that may indirectly indicate about less BSA and P(VP−AA) interaction at high concentrations. As for the Raman peak at 1234 cm^{-1} (related to C−H bending in acrylic acid unit), electrostatic interaction between BSA and P(VP−AA) takes place and hence influences the amplitude. Therefore, the preserved pattern of BSA and P(VP−AA) components in Raman sensing can assist in distinguishing between complex and monocomponent solutions, while the Raman fingerprint of the protein−copolymer complex can provide information on the nature and the intensity of interactions between BSA and P(VP−AA) that promote complex formation.
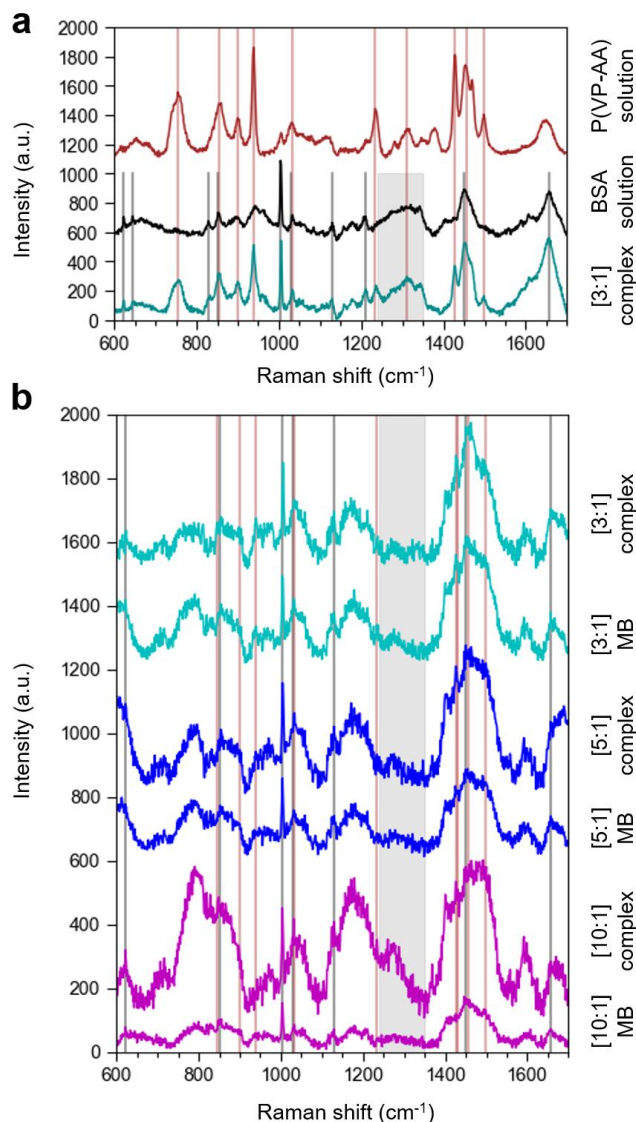
*Figure 6-6. Raman spectra of BSA@P(VP−AA) complexes and MB. (**a**) Measurements are made at high concentrations of PVP (91 mg/mL, brown line) and BSA (250 mg/mL, black line) monocomponent solutions, and BSA@P(VP−AA) [3:1] complex (with BSA and P(VP−AA) concentrations of 273 mg/mL and 91 mg/mL, respectively, represents the cyan line). (**b**) Measurements are made at the total mass concentration of 50 mg/mL for BSA@P(VP−AA) complexes and corresponding MB with the ratio of [3:1] (cyan lines), [5:1] (blue lines), and [10:1] (purple lines), respectively.*

It is worth noting that this feature of reduced P(VP-AA) intensity is not observed well at extremely high concentrations (Figure 6-6a). This is well explained by atomic molecular dynamics simulation model [215,216], which is going to be elaborated in the forthcoming paper of the author's colleagues. Briefly, the explanation is in that at extreme concentrations P(VP-AA) interacts with itself, producing an inert aggregate with reduced probability of interaction with BSA.

RI sensing of BSA@P(VP−AA) complexes and MB is demonstrated in Figure 6-7. As shown in Figure 6-7a, complexes synthesized with different protein: copolymer ratios provide linear dependence of the RI on the total mass concentration (R^2 values greater than 0.977) and *p−values* lower than 0.01. Meanwhile, for MB in Figure 6-7b, only [3:1] MB can provide linear dependence of RI on the total mass concentrations, [5:1] MB can be measured at the total mass concentrations up to 10 mg/mL, while [10:1] MB are able for RI measurements only on concentrations as low as 1.75 mg/mL. For [3:1] MB, the total mass concentration of 50 mg/mL corresponds to the MB concentration of 2.0×10^8 MB/mL. For [5:1] MB, the total mass concentration of 10 mg/mL corresponds to the MB concentration of 4.0×10^8 MB/mL, while higher concentrations (up to 2.0×10^9 MB/mL as total mass concentration of 50 mg/mL) cannot be measured. Similar trend is well pronounced for [10:1] MB sample, where the total mass concentration of 50 mg/mL corresponds to $(1.0 \pm 0.4) \times 10^{10}$ MB/mL. With a components total mass concentration 2.5 mg/mL and higher (corresponds to 5.0×10^8 MB/mL), quasi−sinusoidal pattern with minima in transmission spectrum for [10:1] MB doesn't exist, as illustrated in Figure 6-8, that leads to impossibility to extract RI values according to Equation (6-1). Hence, [3:1] MB could be measured at total mass concentrations of 1.75 mg/mL (that corresponds to the MB concentration of 4.0×10^8 MB/mL) and lower, where the required periodical pattern is preserved. As RI determination requires extracting wavelength minima positions from a periodical transmission spectrum, the upper detection limit for MB samples is 4.0×10^8 MB/mL regardless of MB mean diameters. Therefore, while RI sensing of BSA@P(VP−AA) protein−copolymer complexes can be done with linear dependence of

RI values on concentrations, RI sensing of corresponding BSA@P(VP−AA) MB is limited to the MB concentration of 4.0×10^8 MB/mL.
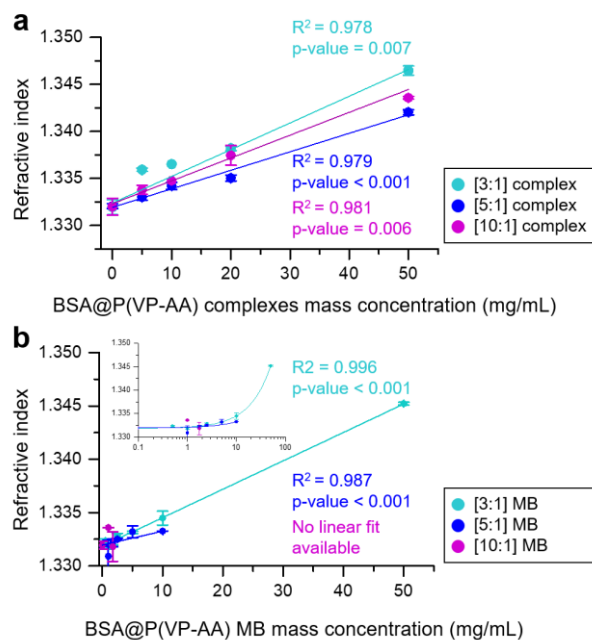
Figure 6-7. RI of BSA@P(VP−AA) complexes and corresponding MB. (a) complexes; (b) MB. The inset chart depicts the same plot in log scale to highlight values at low concentrations.
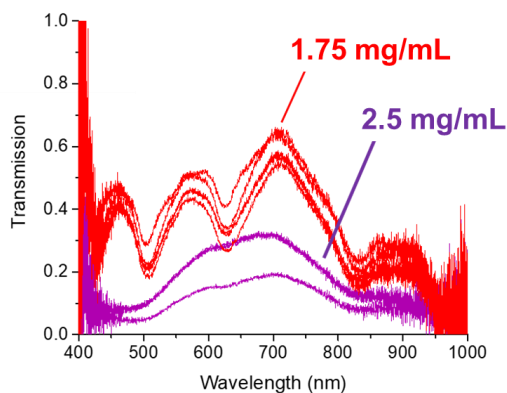
Figure 6-8. Transmission spectra of HC−MOW with BSA@P(VP−AA) [10:1] MB. Measurements are provided at the total mass concentration of 2.5 mg/mL (violet lines), and 1.75 mg/mL (red lines).

6.4. Summary

A 2-in-1 measurement strategy was utilized to analyze a high molecular weight compound, specifically BSA protein. The study obtained data on the dependencies of Raman signal intensity and refractive index on concentration, revealing linear relationships between concentration and both parameters. The sensitivity of the method was up to $2.9 \cdot 10^8$ RIU·mL/mg for RI, while for Raman it was 6.4 mL/mg. Measurements were conducted in a range of 5 to 100 mg/mL, which includes the physiological values of albumin concentration in human plasma (35-50 mg/mL), making the method reliable for medical diagnostics.

Regarding the universality of RI calibration, it should be noted that during analyte flow through HC-MOW, analyte adsorption in the walls may occur. Then, both the refractive index of the core and the wall thickness change, affecting the corresponding two parameters in equation (3-1) and ultimately making it impossible to extract the refractive index. However, the author suggests that analyte absorption wasn't the case for the measurements presented in the present work, because when water was introduced after any of the analytes used in the present work, the spectrum immediately shifted back to the same position as it was with water before any analyte.

The 2-in-1 measurement strategy was further utilized to examine protein-copolymer nanosized conjugates at various concentrations and component ratios (1:1.5, 1:1, 2:1 protein:copolymer molar ratios, that corresponds to 3:1, 5:1 and 10:1 mass ratios, repectively). The effective RI and Raman scattering of the mixture at different component ratios were obtained.

For the first time, the ability to measure the transmission spectra of HC-MOW filled with aqueous MB solutions is demonstrated. The HC-MOW transmission spectra have a dependence on microbubble concentration, with a critical concentration of microbubbles at $4 \cdot 10^8$ MB/mL. Beyond this concentration, the periodicity of the HC-MOW transmission spectrum deteriorates, which can be attributed to an augmented losses caused by light scattering on MB.

The obtained results demonstrated that HC-MOW is promising for multifaceted 2-in-1 characterization of complex solutions.

For further HC-MOW sensor optimization, research on registered Raman scattering amplitudes depending on wall thickness and analyte refractive index and extinction should be provided.

Chapter 7. Exploration of HC-MOW and Raman Spectroscopy Application for Isolation and Analysis of Extracellular vesicles

After the exploration of applicability of the developed two-in-one sensing for colloids systems on example of protein-copolymer structures in ==section== 6.3, this chapter explores the applicability of the present 2-in-1 sensor to extracellular vesicles (EV). But before proceeding to EV sensing, their isolation from cell culture medium or biological fluid is needed and therefore discussed. These results were published in:

a) M.A. Slyusarenko, N.S. Nikiforova, E. I. Sidina, I.V. Nazarova, V.V. Egorov, Y.P. Garmay, A.A. Merdalimova, N.P. Yevlampieva, D.A. Gorin, A.V. Malek, Formation and evaluation of a two-phase polymer system in human plasma as a method for extracellular nanovesicle isolation. Polymers (Basel), 2021, 13(3):1–16. https://doi.org/10.3390/polym13030458 (IF=3.426, Q1) [217]

b) V.Chernyshev, R.Chuprov-Netochin, E.Tsydenzhapova, E.Svirshchevskaya, R.Poltavtseva, A.Merdalimova, A.Yashchenok, A.Keshelava, K.Sorokin, V.Keshelava, G.Sukhikh, D.Gorin, S.Leonov, M.Skliar. Asymmetric depth-filtration: A versatile and scalable method forhigh-yield isolation of extracellular vesicles with low contamination. Journal of Extracellular Vesicles, 11, e12256. https://doi.org/10.1002/jev2.12256 (IF 17.3, Q1) [218]

7.1. Isolation

7.1.1. Asymmetric Depth Filtration

A novel asymmetric DF approach to isolate EV was developed by the author's colleague, lab research scientist V. Chernyshev and collaborators. The present method allows isolation from biological fluids that outperforms ultracentrifugation (that is a gold standatd for EV isolation) and size-exclusion chromatography in purity and yield of isolated EVs. By these metrics, a single-step DF matches or exceeds the performance of multistep protocols with dedicated purification procedures in the isolation of plasma EVs. The selective transit and capture of biological nanoparticles in asymmetric pores by size

and elasticity, low surface binding to the filtration medium, and the ability to cleanse EVs held by the filter before their recovery with the reversed flow all contribute to the achieved purity and yield of preparations were demonstrated. Furthermore, the method's versatility by applying it to isolate EVs from different biofluids (plasma, urine, and cell culture growthmedium) was demonstrated. The DF workflow is simple, fast, and inexpensive. Only standard laboratory equipment is required for its implementation, making DF suitable for low-resource and point-of-use locations. The method may be used for EV isolation from small biological samples in diagnostic and treatment guidance applications. It can also be scaled up to harvest therapeutic EVs from large volumes of cell culture medium.

The asymmetric depth filtration features and protocol are demonstrated in Figure 7-1 and described in subsection 3.7.1. Briefly, the developed method immobilizes EVs on the surface and within the depth of porous medium and then recovers them by reversing the carrier flow through the filter. In a single step, it isolates EVs from complex biological fluids, such as plasma, with high yield and purity.

The author's part of work was to use Raman spectroscopy to compare Raman spectra of proteins and EV. As EV in fact consist of lipids and proteins, their Raman spectra should be enriched compared to bulk protein.

The Raman analysis of plasma EV was performed as described in subsection 3.4.3, with Raman spectra of the clean area of quartz glass and the dried solution of human serum albumin (0.4 g/ml; Octapharma Pharmazeutika Produktionsgesellschaft m.b.H., Austria) as controls.

Raman spectrum of plasma EVs isolated by DF (Figure 7-2) agrees with previous reports [217,219] and contains the expected peaks identified inTable 7-1. Specifically, the peak at 1004 cm^{-1} corresponds to aromatic ring stretching in Phenylalanine. The spectral region between 1200 and 1300 cm^{-1} corresponds to amide III bands, and the peak at 832 cm^{-1} is due to out-of-plane ring breathing in Tyrosine. The presence of cholesterol (peak near 704 cm^{-1}) and lipids (peak at 1440 cm^{-1}, corresponding to CH_2 bending in lipids and cholesterol) reveals membrane constituents of EVs.
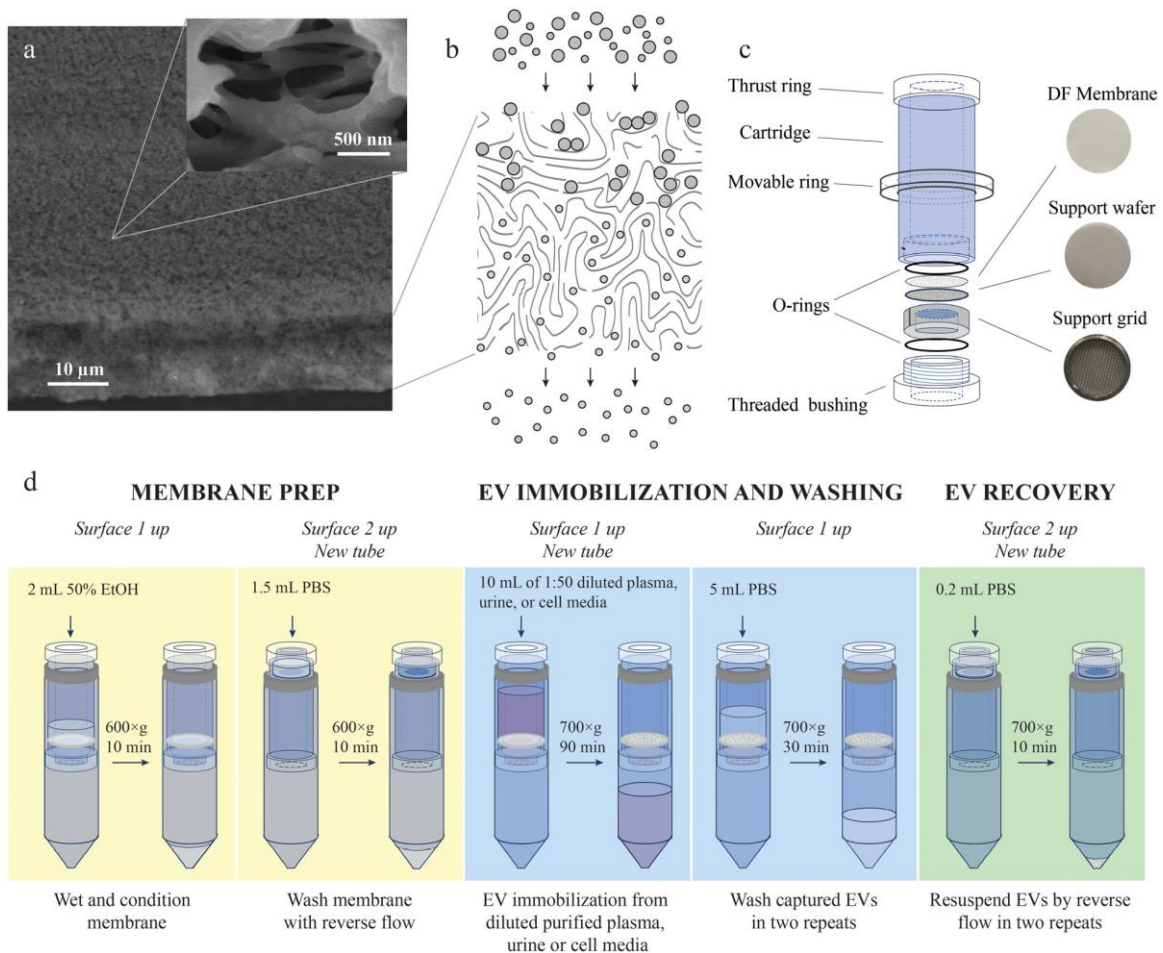
Figure 7-1. Depth-filtration medium, cartridge, and the protocol for DF isolation of EVs from blood plasma, urine, and cell culture media. (a) SEM image of the depth-filtration membrane showing its edge and the entrance surface (Surface 1). Higher magnification (inset) of inlet pores in Surface 1 shows apertures much larger than the size of EVs. As a result, the flow drags vesicles inside the pores until they become immobilized within the depth of the filter. (b) Illustration of the depth filtration process showing two populations of particles of different sizes. Larger particles are retained within the volume of the filtration medium, while smaller particles are eluted. (c) DF cartridge. Photographs of the membrane and its support (porous wafer and stainless-steel grid on which it rests) are shown on the right. (d) Summary of the depth-filtration workflow to isolate EVs from blood plasma, urine, and cell culture media. Reproduced from [218]. Licensed under CC BY-NC-ND 4.0.
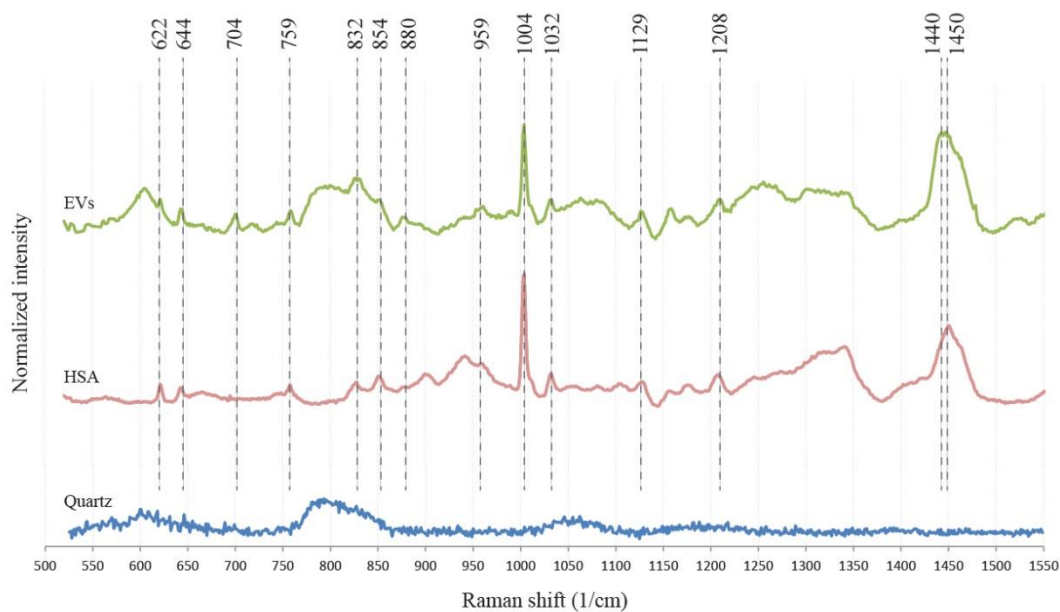
Figure 7-2. Raman spectrum of plasma EVs isolated by depth-filtration is compared with spectra of human serum albumin (HSA) and fused quartz substrate.

Table 7-1. Raman peaks in EV spectra

Raman shift, cm^{-1}	Assumed assignment	Reference
622	Phenylalanine (phenyl ring breathing)	[177]
644	Tyrosine (C–C twisting)	[220]
704	Cholesterol and cholesterol esters	[221,222]
759	Tryptophan	[223]
832	Tyrosine (out of plane ring breathing)	[220,223]
854	Tyrosine (ring breathing mode); proline (C-C ring stretch)	[223]
880	Tryptophan; in-plane rocking (CH_2), e.g., protein	[128,220]
959	Cholesterol	[220,223]
1004	Phenylalanine, C-C aromatic ring stretching	[177,221]

1032	CH$_2$CH$_3$ bending (e.g., phospholipid); C-C vibration (e.g., polysaccharide)	[128]
1129	Lipids and proteins	[221]
1208	Phenylalanine, tryptophan (C-C$_6$H$_5$ stretching)	[223], [224]
1200-1300	Amide III in proteins	[221]
1440-1450	Lipids CH$_2$ deformation at 1437; lipids and proteins CH$_2$/CH$_3$ deformation at 1443; protein CH$_2$ bending mode at 1446	[220], [223], [128]

7.1.2. Two-phase polymer system

The optimized method of a two-phase polymer system in human plasma (PTPS) for EV isolation was developed by the author's colleagues in N.N. Petrov National Medical Research Center of Oncology and Oncosystem Ltd. The aim of the study was to explore the polyethylene glycol–dextran two-phase polymer system formed in human plasma to isolate the exosome-enriched fraction of plasma extracellular nanovesicles. The isolation protocol is described in subsection 3.7.2.

Raman spectroscopy, that is the author's part, was applied to explore the chemical compositions of the phases by evaluation of their characteristic spectra. Figure 7-3 shows the Raman spectra of "pure" PTPS components: dextran, PEG, and UC-isolated ENVs dissolved in PBS and four phases of PTPS (UP1, LP1, UP2, and LP2). Characteristic peaks of "pure" PTPS components and their likely assignments reported previously are listed in Table 7-2 with references.
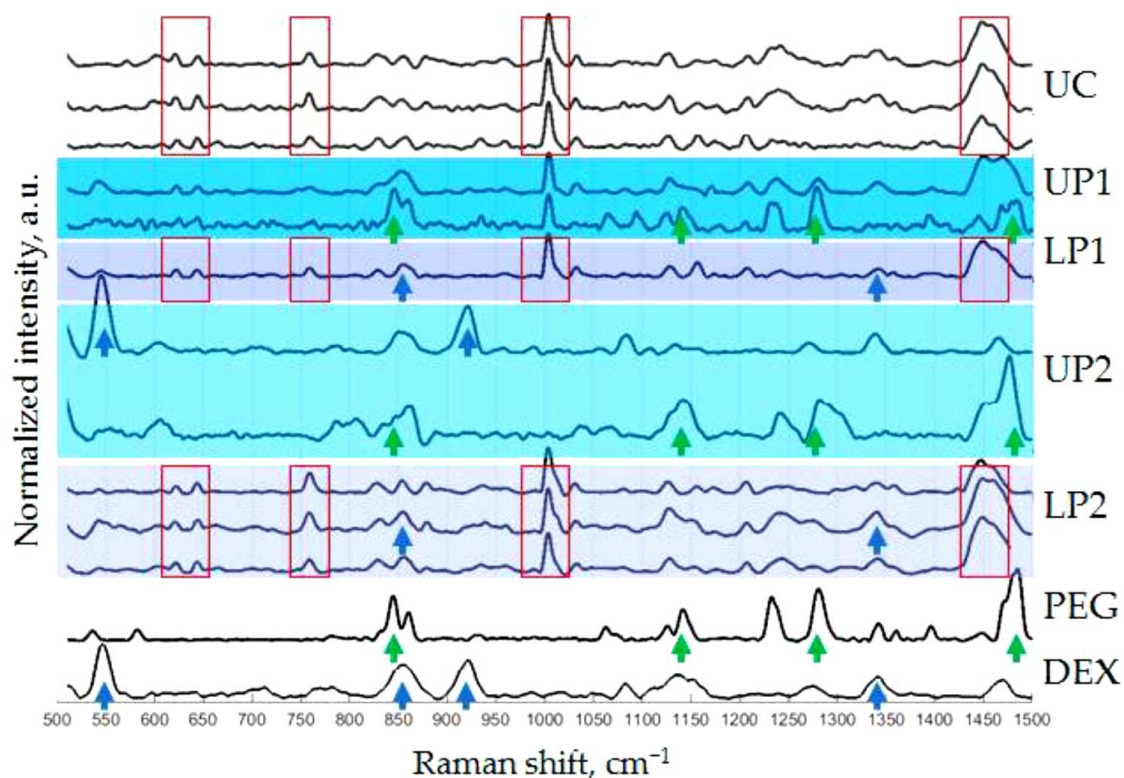
Figure 7-3. Raman spectra of PTPS phases and pure components. Measurements were repeated for samples that were supposed to be not homogeneous enough—these results are shown by multiple curves.

For example, UC-EV-specific peak at 1004 cm^{-1} may reflect the presence of an essential -amino acid phenylalanine, however enrichment of this compound in plasma EV compared to total plasma was not detected. The composition of tested solution included various plasma components and was too complex for precise assigning. Without identifying specific peaks, it is important to note that several characteristic peaks can be observed in spectra of UC-ENV and they are repeated in spectra of lower phases after first (LP1) and second (LP2) separation (red frame). This observation can support the phenomena of the concentration of the plasma vesicles into the dextran-formed lower phase of PTPS.

Table 7-2. Raman peaks in EV and polymers spectra

Sample	Raman shift, cm^{-1}	Likely assignment	Ref.
UC-ENV	622	Phenylalanine (phenyl ring breathing)	[177]
	644	Tyrosine (C–C twisting)	[220]
	758	Tryptophan	[220,223]
	1004	Phenylalanine (phenyl ring breathing)	[177]
	1208	Phenylalanine, tyrosine (C-C$_6$H$_5$ stretching)	[177] [220]
	1230, 1237-1241	Amide III bonds (rand coils and beta-sheet, respectively)	[224]
	1340	Tryptophan, lipids (CH$_2$ deformation)	[225–227]
	1360	Tryptophan (Fermi resonance doublet with 1340 cm^{-1})	[227]
	1449	Lipids and proteins (CH$_2$/CH$_3$ deformation)	[128,224,228]
PEG	844, 860	CH$_2$ rocking	[229,230]
	1141	CO stretch	
	1232	CH$_2$ twist	
	1281	CH$_2$ twist	
	1484	CH$_2$ bending	
Dextran	546	C3C4, C4C5 deformation	[231]
	855	C-1-H bending	[232]
	922	COH deformation	
	1342	CCH deformation, OCH deformation, CO vibration	

As shown by two bottom two lines in the bottom in Figure 7-3, Raman spectra of pure dextran and PEG had also several characteristic peaks. As expected, the profiles of both the LP1 and LP2 phases had similarities to the dextran profile (marked by blue arrows in Figure 7-3), and these results were well reproducible. However, multiple analyses of the

upper phases revealed different results, resembling either dextran or PEG profiles (marked by blue and green arrows in Figure 7-3). It became especially visible after the second phase separation. Two types of spectra, PEG-like with characteristic peaks shown in Figure 7-3 by green arrows and DEX-like with characteristic peaks shown by blue arrows in Figure 7-3, were detected in UP2. It is worth noting here that limit of detection for these two bulk polymers by Raman spectroscopy with the same measurement conditions was estimated to be 1.50 mg/dL for DEX and 7 mg/dL for PEG.

To determine the nature of this observation, samples dried on the surface of quartz glass were visualized before Raman spectroscopy. The dried UP2 phase revealed a bubble-like texture, as shown in Figure 7-4. Raman spectra taken inside of these "bubbles" showed a PEG-like profile, while spectra measured outside of "bubbles" were similar to dextran spectra. This result revealed the presence of both polymers in upper phases and their tendency to segregate within them. Incomplete partitioning of the plasma two-phase polymer system during the applied procedure might influence the efficacy of plasma component separation.
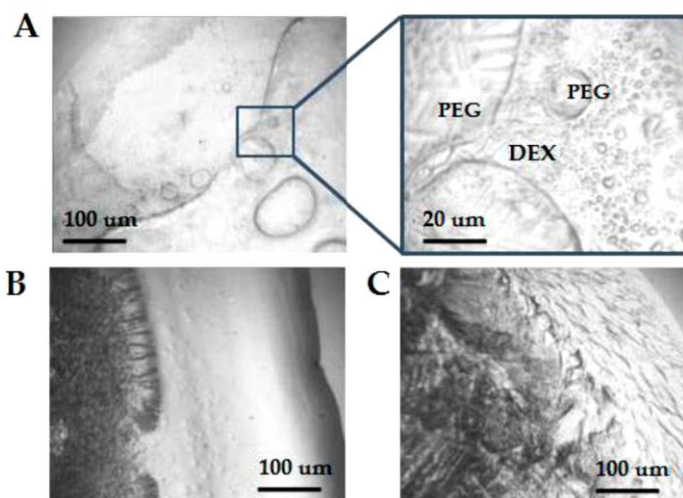
Figure 7-4. Area of dried drops of polymer mixtures and pure solutions visualized by
light microscopy before Raman spectrometry.
(A) Upper phase 2 UP2; (B) Dextran; (C) PEG.

Raman spectroscopy confirmed NTA results [217], namely the phenomena of phase separation in plasma solutions of PEG (20 kDa) 3.5% and dextran (450–650 kDa) 1.5%. Particles of exosomal size are concentrated in the lower phase, and their Raman spectra are similar to the spectra of UC-isolated plasma ENVs. Repeated phase separation did not considerably change the nanoparticle content (NTA) or chemical composition (RS) of the lower phase; however, it resulted in the appearance of nanoparticles of different sizes in the upper phase. It is interesting to note that the second round of phase separation resulted in an appearance of differently-sized particles in the upper phase and DEX-characteristic peaks 546 and 922 cm^{-1} in its Raman spectra, and that both were not detected in UP1. However, the currently available data are not sufficient to explain this coincidence.

7.2. Two-in-one sensing of EV in HC-MOW

The idea of two-in-one EV sensing implies that firstly EV presence may be detected by refractive index sensing in HC-MOW, and the Raman sensing in HC-MOW would help to distinguish target EV.

7.2.1. Characterization

The exosome-like fraction of EV was used, e.g. with size 50-200 nm, obtained from two cell lines: 22rv1 and skov3. To estimate their size distribution and concentration, nanoparticle tracking analysis (NTA) was used. The results are demonstrated in Figure 7-5: the median sizes are almost the same, but concentrations differ by one order: approximately 6 x 10^{11} 1/mL for 22rv1 and 6 x 10^{10} 1/mL for skov3, respectively.

7.2.2. Refractive index sensing

Similar to BSA, the transmission spectrum of exosomes 22rv1 and skov3 was measured in HC-MOW. The results are shown in Figure 7-6.
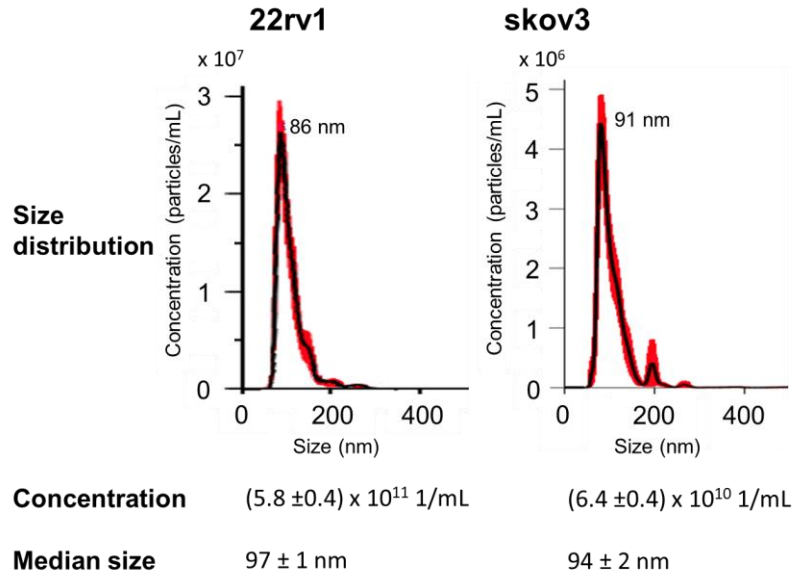
Figure 7-5. Characterization of extracellular vesicles (EV): size distribution and concentration.
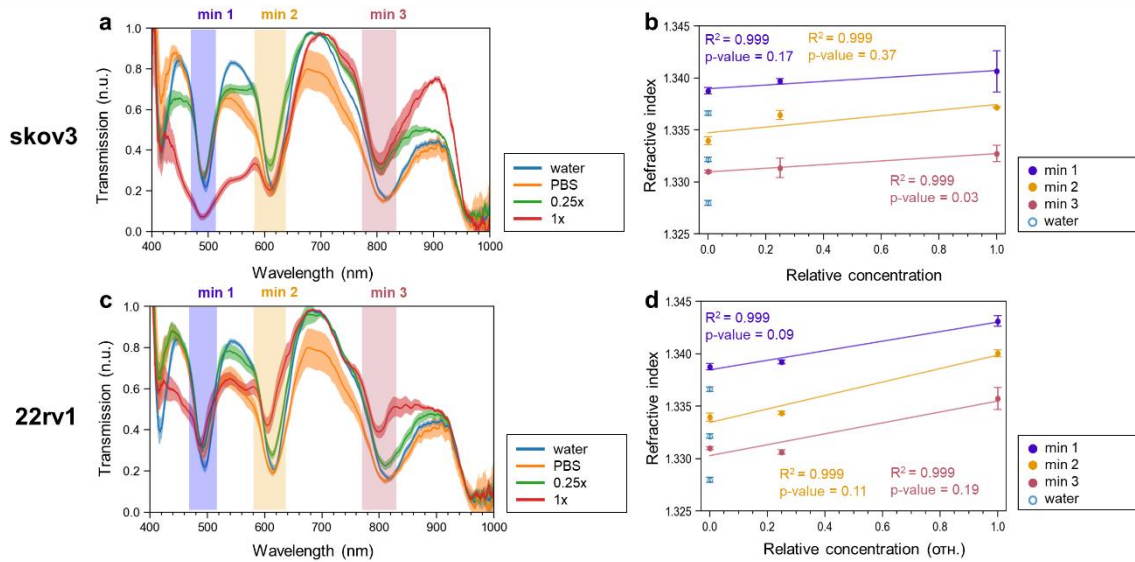
Figure 7-6. Measurement of the refractive index of EV in a waveguide. (a) Transmission spectra of skov3 vesicles; (b) refractive index versus relative concentration for skov3; (c) transmission spectra of 22rv1 vesicles; (d) refractive index versus concentration for 22rv1. The concentrations used were: 0 = PBS; 0.25 = initial EV diluted by a factor of 4; 1 = initial EV concentration.

114

As the buffer for the exosomes is PBS and not water, the direct approximations were made through the points for PBS as the zero concentration of the exosomes. That is, in Figure 7-6b,d the points for water are not involved in the approximation by straight line, and are shown only for comparison. On the plotted approximation lines it can be observed that R^2 is still close to unity, however the p-value in most cases does not pass the barrier of 0.05 (i.e. greater than it). However, instead of analysing three points (relative concentrations of 0, 0.25 and 1), only 2 points may be compared, PBS and exosomes at their original concentration, using the t-test and the mean and RMS values of the refractive index. The results are shown in Figure 7-7 - both solutions with EV used showed a statistically significant difference to PBS in their refractive index.
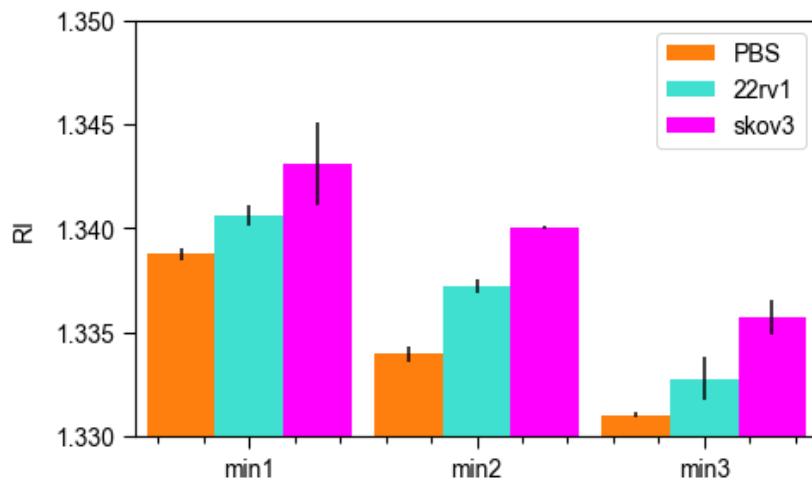
Figure 7-7. Comparison of the refractive index of EV solutions and the control (PBS) for the initial EV concentrations.

7.2.3. Raman spectroscopy

Finally, Raman scattering of EV (described in the previous two subsections) and controls were measured in HC-MOW. The results are demonstrated in Figure 7-8, with two representative instances for every cell line: the first two (1-2) spectra belong to EV solutions from 22rv1 cell line, the next two (3-4) belong to EV solutions from skov3 cell line, with all these samples measured in HC-MOW; all lines below are controls, such as PBS (5) and water (6) in HC-MOW, and water in a drop in a silica substrate (7). It can be

115

noted that Raman spectra from EV solutions from both cell lines may be either without any significant peaks (2, 4) or exhibit the same peaks as control water and PBS solutions in water. These Raman peaks are enumerated in Table 7-3. The overall Raman spectrum is characteristic for polypropylene [233] rather than for proteins and lipids, as could be expected for EV [218,221] and was enlisted in Table 7-1. Polypropylene is the material of the 0.5 mL eppendorf tube used in the measurement and surrounding the HC-MOW bottom end, as illustrated in Figure 3-5.

Thus, despite the long signal acquisition time (90 or 120 s), the Raman spectrum of EV was not observed, which is a negative outcome. But meanwhile the obtained spectra (1, 3, 5, 6) demonstrate that light does indeed travel along the entire fiber, reaches the bottom, and in the opposite direction Raman scattering from there reaches the objective.
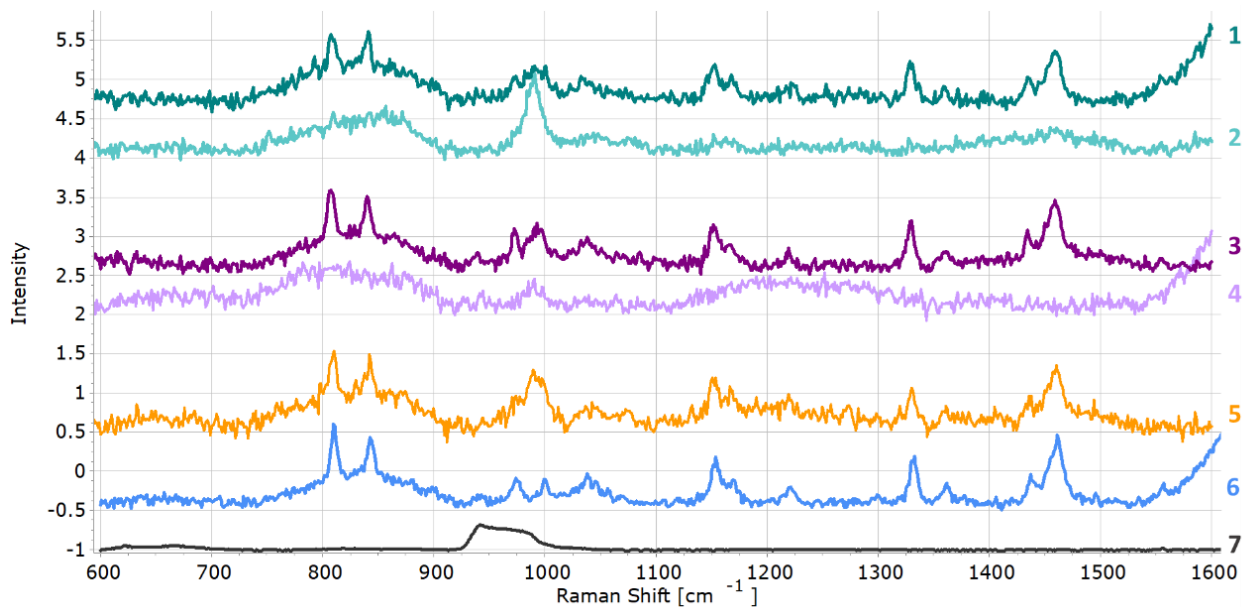
Figure 7-8. Raman spectra of EV solutions and controls.
1-2: 22rv1 in HC-MOW; 3-4: skov3 in HC-MOW; 5: PBS control in HC-MOW;
6: water in HC-MOW; 7: water in a drop on a silicon substrate.

Table 7-3. Raman peaks observed in the measured EV solutions

Raman shift, cm^{-1}	Likely assignment	Ref.
808	CH$_2$ rocking, C-C stretching	[233,234]
841	CH$_2$ rocking	[233,234]
972	CH$_3$ rocking, C-C stretching	[233,234]
998	CH$_3$ rocking	[233,234]
1151	C-C stretching, CH bending	[233,234]
1168	C-C stretching, CH$_3$ rocking, C-C wagging	[233,234]
1220	CH$_2$ twisting, CH wagging, C-C stretching	[233,234]
1435	CH$_2$ bending	[233,234]
1458	CH$_2$ bending	[233,234]

The EV concentration used in the present experiment in HC-MOW is $5 \cdot 10^{11}$ 1/mL, which corresponds to total protein concentration around 52 µg/mL. Meanwhile, in section 4.2, Figure 4.2b we demonstrated performance of HC-MOW sensor for a BSA protein. With noise level at Raman measurements 26 arb.u. (as was experimentally determined by the author), it is evident that protein concentration 52 µg/mL is far below the possible detection limit.

As for overcoming the problem of lacking EV spectra, potential solutions may involve increasing concentration or implementing Raman tags or plasmonic particles to boost the Raman signal [80,88].

7.3. Summary

It is shown that Raman spectroscopy can be used to demonstrate the process of phase separation of two high-molecular-weight components of the solution used for extracellular nanovesicle isolation.

Raman spectroscopy of lipid and protein characteristic bands allowed the approval of asymmetric depth filtration for extracellular vesicles isolation. The findings are in good accordance with the Western blotting and mass spectrometric data.

At the concentrations of EV used in the investigation (from $1.5 \cdot 10^{10}$ 1/mL to $5 \cdot 10^{11}$ 1/mL), a statistically significant difference in refractive index from the control sample was detected. Thus, the applicability of HC-MOW for EV detection by refractive index was demonstrated, which makes HC-MOW promising for medical diagnostics.

No characteristic Raman peaks were observed in the EV Raman scattering spectra, suggesting the need for higher concentrations or the use of Raman tags or plasmonic particles to enhance the Raman signal. However, the obtained spectra demonstrate that the laser light travels all the way through the provided HC-MOW (2.5 cm), reaching the bottom, and Raman scattering from that point travels in the HC-MOW in the opposite direction, ultimately reaching the objective.

Chapter 8. Conclusion

8.1. Summary on research

The present work is aimed at developing sensors based on HC-MOW. Raman scattering, multi-wavelength RI, and layer thickness are the physical properties that can be measured in HC-MOW and used for sensing. The goal of the work has been achieved. In conclusion, we would like to formulate the most important results.

It was shown that the use of a 2.5 cm long HC-MOW allows the increase of the intensity of the observed Raman scattering in contrast to measuring a larger volume drop on a planar substrate. It was found that the enhancement factor for the low molecular weight compound (R6G was taken) is 50, and for the high molecular weight compound (BSA) it is 2.3x. The difference in the enhancement factor between the high molecular weight and low molecular weight compound is explained by the difference in the effective refractive index part.

A 2-in-1 sensing in HC-MOW, combining multi-wavelength refractometry and improved Raman spectroscopy, was utilized to analyze a high molecular weight compound, specifically BSA protein. The study obtained data on the dependencies of Raman signal intensity and refractive index on concentration, revealing linear relationships between concentration and both parameters. The sensitivity of the method was up to $2.9 \cdot 10^8$ RIU·mL/mg for RI, while for Raman it was 6.4 mL/mg. Measurements were conducted in a range of 5 to 100 mg/mL, which includes the physiological values of albumin concentration in human plasma (35-50 mg/mL), making the method reliable for medical diagnostics. Furthermore, the 2-in-1 measurement strategy was utilized to examine protein-copolymer nanosized conjugates at various concentrations and component ratios (1:1.5, 1:1, 2.3:1 protein:copolymer molar ratios). The effective RI and Raman scattering of the mixture at different component ratios were obtained.

The ability to measure the transmission spectra of HC-MOW filled with aqueous microbubble (MB) solutions was demonstrated. The HC-MOW transmission spectra shifts exhibited a dependence on microbubble concentration, with a maximum detection

threshold concentration of microbubbles at $4 \cdot 10^8$ 1/mL. Above this concentration, the quality of the HC-MOW transmission spectrum deteriorates, which can be attributed to increased light propagation losses caused by light scattering on MB.

Furthermore, Raman spectroscopy was used for two protocols of extracellular vesicles (EV) isolation, with EV concentrations ac. $3 \cdot 10^{11}$ 1/mL. It was shown that Raman spectroscopy can be used to demonstrate the result of phase separation of two high-molecular-weight components (PEG, dextran) of the solution used for extracellular nanovesicle isolation in aspect of purity of obtained fractions. Also, Raman spectroscopy of lipid and protein characteristic bands enabled the approval of asymmetric depth filtration for extracellular vesicles isolation. These findings are in good accordance with the Western blotting and mass spectrometric data.

8.2. Future directions and applications

The developed sensing methods show promise for real-time in-flow detection of small quantities of biological markers, such as EV or proteins, making them valuable for rapid diagnostics. However, robust characterization of EV by their Raman scattering has not been achieved. To overcome this drawback, several further steps can be initiated, as described below.

In subsections 7.1.1 and 7.1.2, Raman spectra of EV solutions in the form of a 2 µL drop were detected. These EV were isolated from human plasma. Meanwhile, in subsection 7.2.3, the same EV concentration was used in HC-MOW, which should enhance Raman signal, but EV weren't seen there. The drawback is that in each of these three subsections only one method of EV detection was used (2 µL drop or HC-MOW), and all three isolation methods were different. Therefore, it is recommended to use the identical EV solutions in both ways for more thorough comparison to determine the possibility of fiber enhancement of Raman scattering in HC-MOW, similar to its enhancement for R6G and BSA studied in Chapter 4.

After the experiments proposed in the previous paragraph, the need for higher concentrations of EV is expected to be found. Alternatively, the use of Raman tags or plasmonic particles to enhance the Raman signal can be considered.

Another approach for targeted EV detection in HC-MOW may be as follows: the inner walls are functionalized with targeting ligands for specific proteins of interest, allowing targeted capture of EV which are released by particular cell type (e.g., we are interested in cancer ones for early diagnosis). The presence of the targeted EV is then detected as a change in the thickness of the inner wall, similar to what was done in section 5.2.

SERS structures grown in HC-MOW can also be improved by annealing and/or repeated multistep protocol. Changing from UV-induced reduction to other catalysts can be considered, since the HC-MOW structure hinders irradiation of the liquid inside.

Finally, the model of the light propagation and thus the transmission spectrum in HC-MOW should be developed, aiming to achieve full agreement with the experimental spectra.

The author believes that the proposed solutions will enable achieving the planned use of the HC-MOW for the analysis of extracellular vesicles.

Bibliography

1.   Nazarenko, I. Extracellular Vesicles: Recent Developments in Technology and Perspectives for Cancer Liquid Biopsy. **2020**, doi:10.1007/978-3-030-26439-0_17.

2.   Li, G.; Tang, W.; Yang, F. Cancer Liquid Biopsy Using Integrated Microfluidic Exosome Analysis Platforms. *Biotechnol. J.* **2020**, *1900225*, 1–10, doi:10.1002/biot.201900225.

3.   Tenchov, R.; Sasso, J.M.; Wang, X.; Liaw, W.-S.; Chen, C.-A.; Zhou, Q.A. Exosomes─Nature's Lipid Nanoparticles, a Rising Star in Drug Delivery and Diagnostics. *ACS Nano* **2022**, *16*, 17802–17846, doi:10.1021/acsnano.2c08774.

4.   Rondelli, V.; Helmy, S.; Passignani, G.; Parisse, P.; Di Silvestre, D. Integrated Strategies for a Holistic View of Extracellular Vesicles. *ACS Omega* **2022**, *7*, 19058–19069, doi:10.1021/acsomega.2c01003.

5.   Kalluri, R.; LeBleu, V.S. The Biology, Function, and Biomedical Applications of Exosomes. *Science* **2020**, *367*, doi:10.1126/science.aau6977.

6.   Tai, Y.L.; Chen, K.C.; Hsieh, J.T.; Shen, T.L. Exosomes in Cancer Development and Clinical Applications. *Cancer Sci.* **2018**, *109*, 2364–2374, doi:10.1111/cas.13697.

7.   He, M.; Zeng, Y. Microfluidic Exosome Analysis toward Liquid Biopsy for Cancer. *J. Lab. Autom.* **2016**, *21*, 599–608, doi:10.1177/2211068216651035.

8.   Lucchetti, D.; Fattorossi, A.; Sgambato, A. Extracellular Vesicles in Oncology: Progress and Pitfalls in the Methods of Isolation and Analysis. *Biotechnol. J.* **2018**, *14*, doi:10.1002/biot.201700716.

9.   Rupert, D.L.M.; Claudio, V.; Lässer, C.; Bally, M. Methods for the Physical Characterization and Quantification of Extracellular Vesicles in Biological Samples. *Biochim. Biophys. Acta BBA - Gen. Subj.* **2017**, *1861*, 3164–3179, doi:10.1016/j.bbagen.2016.07.028.

10.   Perevoschikov, S.; Kaydanov, N.; Ermatov, T.; Bibikova, O.; Usenov, I.; Sakharova, T.; Bocharnikov, A.; Skibina, J.; Artyushenko, V.; Gorin, D. Light

Guidance up to 6.5 Mm in Borosilicate Soft Glass Hollow-Core Microstructured Optical Waveguides. *Opt. Express* **2020**, *28*, 27940, doi:10.1364/oe.399410.

11. Debord, B.; Amrani, F.; Vincetti, L.; Gérôme, F.; Benabid, F. Hollow-Core Fiber Technology: The Rising of "Gas Photonics." *Fibers* **2019**, *7*, doi:10.3390/FIB7020016.

12. Ding, W.; Wang, Y.Y.; Gao, S.F.; Wang, M.L.; Wang, P. Recent Progress in Low-Loss Hollow-Core Anti-Resonant Fibers and Their Applications. *IEEE J. Sel. Top. Quantum Electron.* **2020**, *26*, doi:10.1109/JSTQE.2019.2957445.

13. A. M Zheltikov Colors of Thin Films, Antiresonant Phenomena in Optical Systems, and the Limiting Loss of Modes in Hollow Optical Waveguides. *Uspekhi Fiz. Nauk* **2008**, *178*, 619–629, doi:10.3367/ufnr.0178.200806d.0619.

14. Ermatov, T.; Noskov, R.E.; Machnev, A.A.; Gnusov, I.; Atkin, V.; Lazareva, E.N.; German, S.V.; Kosolobov, S.S.; Zatsepin, T.S.; Sergeeva, O.V.; et al. Multispectral Sensing of Biological Liquids with Hollow-Core Microstructured Optical Fibres. *Light Sci. Appl.* **2020**, *9*, doi:10.1038/s41377-020-00410-8.

15. Bratashov, D.N.; Burmistrova, N.A.; Bondarenko, S.D.; Khlebtsov, B.N.; Atkin, V.S.; Shuvalov, A.A.; Zanishevskaya, A.A.; Skibina, Y.S.; Goryacheva, I.Y. Microstructured Waveguides with Polyelectrolyte-Stabilized Gold Nanostars for SERS Sensing of Dissolved Analytes. *Materials* **2018**, *11*, doi:10.3390/ma11050734.

16. Yan, D.; Popp, J.; Pletz, M.W.; Frosch, T. Highly Sensitive Broadband Raman Sensing of Antibiotics in Step-Index Hollow-Core Photonic Crystal Fibers. *ACS Photonics* **2017**, *4*, 138–145, doi:10.1021/acsphotonics.6b00688.

17. Ding, H.; Hu, D.J.J.; Yu, X.; Liu, X.; Zhu, Y.; Wang, G. Review on All-Fiber Online Raman Sensor with Hollow Core Microstructured Optical Fiber. *Photonics* **2022**, *9*, doi:10.3390/photonics9030134.

18. Markin, A.V.; Markina, N.E.; Goryacheva, I.Y. Raman Spectroscopy Based Analysis inside Photonic-Crystal Fibers. *TrAC - Trends Anal. Chem.* **2017**, *88*, 185–197, doi:10.1016/j.trac.2017.01.003.

19. Mu, Y.; Liu, M.; Li, J.; Zhang, X. Plasmonic Hollow Fibers with Distributed Inner-Wall Hotspots for Direct SERS Detection of Flowing Liquids. *Opt. Lett.* **2021**, *46*, 1369, doi:10.1364/ol.415733.

20. Khetani, A.; Momenpour, A.; Alarcon, E.I.; Anis, H. Hollow Core Photonic Crystal Fiber for Monitoring Leukemia Cells Using Surface Enhanced Raman Scattering (SERS). *Biomed. Opt. Express* **2015**, *6*, 4599, doi:10.1364/BOE.6.004599.

21. Ni, W.; Yang, C.; Luo, Y.; Xia, R.; Lu, P.; Hu, D.J.J.; Danto, S.; Shum, P.P.; Wei, L. Recent Advancement of Anti-Resonant Hollow-Core Fibers for Sensing Applications. *Photonics* **2021**, *8*, doi:10.3390/photonics8040128.

22. Bufetov, I.A.; Kosolapov, A.F.; Pryamikov, A.D.; Gladyshev, A.V.; Kolyadin, A.N.; Krylov, A.A.; Yatsenko, Y.P.; Biryukov, A.S. Hollow-Core Revolver Fibers (Properties, Design and Fabrication, Applications). *Photonics Russ.* **2019**, *13*, 426–443, doi:10.22184/FRos.2019.13.5.426.443.

23. Zanishevskaya, A.A.; Malinin, A.V.; Tuchin, V.V.; Skibina, Y.S.; Silokhin, I.Y. Photonic Crystal Waveguide Biosensor. *J. Innov. Opt. Health Sci.* **2013**, *6*, 1–6, doi:10.1142/S1793545813500089.

24. Liu, Z.; Zhang, W.; Zhang, X.; Wang, S.; Xia, Z.; Guo, X.; Zhao, Y.; Wang, P.; Wang, X.H. Microstructured Optical Fiber-Enhanced Light-Matter Interaction Enables Highly Sensitive Exosome-Based Liquid Biopsy of Breast Cancer. *Anal. Chem.* **2023**, *95*, 1095–1105, doi:10.1021/acs.analchem.2c03794.

25. Merdalimova, Anastasiia A. Vorobev, V.; Aleksandrov, A.; Barmin, R.; Terentyeva, D.; Estifeeva, T.M.; German, S.; Chernyshev, V.; Maslov, O.; Skibina, Y.S.; Rudakovskaya, P.; et al. Two-in-One Sensor of Refractive Index and Raman Scattering Using Hollow−Core Microstructured Optical Fibers for Colloid Characterization. *Adv. Opt. Mater.* **2023**, *submitted*.

26. Lægsgaard, J.; Bjarklev, A.; Monro, T. Microstructured Optical Fibers. *Handb. Optoelectron. Second Ed. Concepts Devices Tech.* **2017**, *1*, 711–740, doi:10.1201/9781315157009.

27. Debord, B.; Amrani, F.; Vincetti, L.; Gérôme, F.; Benabid, F. Hollow-Core Fiber Technology: The Rising of "Gas Photonics." *Fibers* **2019**, *7*, doi:10.3390/FIB7020016.

28. Skibina, J.S.; Iliew, R.; Bethge, J.; Bock, M.; Fischer, D.; Beloglasov, V.I.; Wedell, R.; Steinmeyer, G. A Chirped Photonic-Crystal Fibre. *Nat. Photonics* **2008**, *2*, 679–683, doi:10.1038/nphoton.2008.203.

29. Skibina, Y.S.; Tuchin, V.V.; Beloglazov, V.I.; Shteinmaeer, G.; Betge, I.L.; Wedell, R.; Langhoff, N. Photonic Crystal Fibres in Biomedical Investigations. *Quantum Electron.* **2011**, *41*, 284–301, doi:10.1070/qe2011v041n04abeh014536.

30. Russell, P.S.J. Photonic Crystal Fibers. *Science* **2003**, *299*, doi:10.1126/science.1079280.

31. Pryamikov, A.D.; Biriukov, A.S.; Kosolapov, A.F.; Plotnichenko, V.G.; Semjonov, S.L.; Dianov, E.M. Demonstration of a Waveguide Regime for a Silica Hollow - Core Microstructured Optical Fiber with a Negative Curvature of the Core Boundary in the Spectral Region > 35 Mm. *Opt. Express* **2011**, *19*, 1441, doi:10.1364/oe.19.001441.

32. Antonopoulos, G.; Benabid, F.; Birks, T.A.; Bird, D.M.; Knight, J.C.; St Russell, P.J.; Cregan, R.F.; Mangan, B.J.; Roberts, P.J.; Allan, D.C. Experimental Demonstration of the Frequency Shift of Bandgaps in Photonic Crystal Fibers Due to Refractive Index Scaling. *Opt. Express Vol 14 Issue 7 Pp 3000-3006* **2006**, *14*, 3000–3006, doi:10.1364/OE.14.003000.

33. *Handbook of Optical Fibers*; Peng, G.-D., Ed.; Springer Singapore: Singapore, 2019; ISBN 978-981-10-7085-3.

34. Ermatov, T.; Skibina, J.S.; Tuchin, V.V.; Gorin, D.A. Functionalized Microstructured Optical Fibers: Materials Methods Applications. *Materials* **2020**, *13*, doi:10.3390/ma13040921.

35. Li, J.; Ebendorff-Heidepriem, H.; Gibson, B.C.; Greentree, A.D.; Hutchinson, M.R.; Jia, P.; Kostecki, R.; Liu, G.; Orth, A.; Ploschner, M.; et al. Perspective: Biomedical Sensing and Imaging with Optical Fibers - Innovation through

Convergence of Science Disciplines. *APL Photonics* **2018**, *3*, doi:10.1063/1.5040861.

36. Calcerrada, M.; García-Ruiz, C.; González-Herráez, M. Chemical and Biochemical Sensing Applications of Microstructured Optical Fiber-Based Systems. *Laser Photonics Rev.* **2015**, *9*, 604–627, doi:10.1002/lpor.201500045.

37. Schartner, E.P.; Tsiminis, G.; François, A.; Kostecki, R.; Warren-Smith, S.C.; Nguyen, L.V.; Heng, S.; Reynolds, T.; Klantsataya, E.; Rowland, K.J.; et al. Taming the Light in Microstructured Optical Fibers for Sensing. *Int. J. Appl. Glass Sci.* **2015**, *6*, 229–239, doi:10.1111/ijag.12128.

38. Ferreira, M.F.S.; Castro-Camus, E.; Ottaway, D.J.; López-Higuera, J.M.; Feng, X.; Jin, W.; Jeong, Y.; Picqué, N.; Tong, L.; Reinhard, B.M.; et al. Roadmap on Optical Sensors. *J. Opt. U. K.* **2017**, *19*, doi:10.1088/2040-8986/aa7419.

39. Candiani, A.; Cucinotta, A. Functionalized Microstructured Optical Fibers for Specific Nucleic Acid Detection. In *Optofluidics, Sensors and Actuators in Microstructured Optical Fibers*; Elsevier, 2015; pp. 229–246 ISBN 978-1-78242-329-4.

40. Caucheteur, C.; Guo, T.; Albert, J. Review of Plasmonic Fiber Optic Biochemical Sensors: Improving the Limit of Detection. *Anal. Bioanal. Chem.* **2015**, *407*, 3883–3897, doi:10.1007/s00216-014-8411-6.

41. Decher, G.; Hong, J.D.; Schmitt, J. *Thin Solid Films, 210/21 I*; 1992; pp. 831–835;.

42. Ermatov, T.; Petrov, Y.V.; German, S.V.; Zanishevskaya, A.A.; Shuvalov, A.A.; Atkin, V.; Zakharevich, A.; Khlebtsov, B.N.; Skibina, J.S.; Ginzburg, P.; et al. Microstructured Optical Waveguide-Based Endoscopic Probe Coated with Silica Submicron Particles. *Materials* **2019**, *12*, doi:10.3390/ma12091424.

43. Noskov, R.E.; Zanishevskaya, A.A.; Shuvalov, A.A.; German, S.V.; Inozemtseva, O.A.; Kochergin, T.P.; Lazareva, E.N.; Tuchin, V.V.; Ginzburg, P.; Skibina, J.S.; et al. Enabling Magnetic Resonance Imaging of Hollow-Core Microstructured Optical Fibers via Nanocomposite Coating. *Opt. Express* **2019**, *27*, 9868, doi:10.1364/oe.27.009868.

44. Lopez-Torres, D.; Elosua, C.; Villatoro, J.; Zubia, J.; Rothhardt, M.; Schuster, K.; Arregui, F.J. Photonic Crystal Fiber Interferometer Coated with a PAH/PAA Nanolayer as Humidity Sensor. *Sens. Actuators B Chem.* **2017**, *242*, 1065–1072, doi:10.1016/j.snb.2016.09.144.

45. Kostecki, R.; Ebendorff-Heidepriem, H.; Afshar V., S.; McAdam, G.; Davis, C.; Monro, T.M. Novel Polymer Functionalization Method for Exposed-Core Optical Fiber. *Opt. Mater. Express* **2014**, *4*, 1515, doi:10.1364/OME.4.001515.

46. Sciacca, B.; François, A.; Klingler-Hoffmann, M.; Brazzatti, J.; Penno, M.; Hoffmann, P.; Monro, T.M. Radiative-Surface Plasmon Resonance for the Detection of Apolipoprotein E in Medical Diagnostics Applications. *Nanomedicine Nanotechnol. Biol. Med.* **2013**, *9*, 550–557, doi:10.1016/j.nano.2012.10.007.

47. François, A.; Reynolds, T.; Monro, T. A Fiber-Tip Label-Free Biological Sensing Platform: A Practical Approach toward In-Vivo Sensing. *Sensors* **2015**, *15*, 1168–1181, doi:10.3390/s150101168.

48. Nguyen, L.V.; Warren-Smith, S.C.; Cooper, A.; Monro, T.M. Molecular Beacons Immobilized within Suspended Core Optical Fiber for Specific DNA Detection. *Opt. Express* **2012**, *20*, 29378, doi:10.1364/OE.20.029378.

49. Csaki, A.; Jahn, F.; Latka, I.; Henkel, T.; Malsch, D.; Schneider, T.; Schröder, K.; Schuster, K.; Schwuchow, A.; Spittel, R.; et al. Nanoparticle Layer Deposition for Plasmonic Tuning of Microstructured Optical Fibers. *Small* **2010**, *6*, 2584–2589, doi:10.1002/smll.201001071.

50. Younus, M.H.; Ali, G.Ghazi.; Salih, H.A. The Reinforced Optical Fiber Sensing with Bilayer AuNPs/SiC for Pressure Measurement: Characterization and Optimization. *J. Phys. Conf. Ser.* **2021**, *1795*, 012002, doi:10.1088/1742-6596/1795/1/012002.

51. Wu, J.; Li, Y.; Song, B.; Zhang, C.; Wang, Q.; Gao, X.; Huang, K. *Microstructured Optical Fiber Based on Surface Plasmon Resonance for Dual-Optofluidic-Channel Sensing*; In Review, 2022;

52. Arghir, I.; Delport, F.; Spasic, D.; Lammertyn, J. Smart Design of Fiber Optic Surfaces for Improved Plasmonic Biosensing. *New Biotechnol.* **2015**, *32*, 473–484, doi:10.1016/j.nbt.2015.03.012.

53. Kumar, S.; Singh, R.; Kaushik, B.K.; Chen, N.K.; Yang, Q.S.; Zhang, X. Lspr-Based Cholesterol Biosensor Using Hollow Core Fiber Structure. *IEEE Sens. J.* **2019**, *19*, 7399–7406, doi:10.1109/JSEN.2019.2916818.

54. Schroder, K.; Csaki, A.; Schwuchow, A.; Jahn, F.; Strelau, K.; Latka, I.; Henkel, T.; Malsch, D.; Schuster, K.; Weber, K.; et al. Functionalization of Microstructured Optical Fibers by Internal Nanoparticle Mono-Layers for Plasmonic Biosensor Applications. *IEEE Sens. J.* **2012**, *12*, 218–224, doi:10.1109/JSEN.2011.2144580.

55. Candiani, A.; Giannetti, S.; Sozzi, M.; Coscelli, E.; Poli, F.; Cucinotta, A.; Bertucci, A.; Corradini, R.; Konstantaki, M.; Margulis, W.; et al. Microstructured Optical Fiber Bragg Grating Sensor for DNA Detection.; Gannot, I., Ed.; San Francisco, California, USA, March 20 2013; p. 85760E.

56. Bratashov, D.N.; Burmistrova, N.A.; Bondarenko, S.D.; Khlebtsov, B.N.; Atkin, V.S.; Shuvalov, A.A.; Zanishevskaya, A.A.; Skibina, Y.S.; Goryacheva, I.Y. Microstructured Waveguides with Polyelectrolyte-Stabilized Gold Nanostars for SERS Sensing of Dissolved Analytes. *Materials* **2018**, *11*, doi:10.3390/ma11050734.

57. Ermatov, T.; Noskov, R.E.; Machnev, A.A.; Gnusov, I.; Atkin, V.; Lazareva, E.N.; German, S.V.; Kosolobov, S.S.; Zatsepin, T.S.; Sergeeva, O.V.; et al. Multispectral Sensing of Biological Liquids with Hollow-Core Microstructured Optical Fibres. *Light Sci. Appl.* **2020**, *9*, 173, doi:10.1038/s41377-020-00410-8.

58. Bertucci, A.; Manicardi, A.; Candiani, A.; Giannetti, S.; Cucinotta, A.; Spoto, G.; Konstantaki, M.; Pissadakis, S.; Selleri, S.; Corradini, R. Detection of Unamplified Genomic DNA by a PNA-Based Microstructured Optical Fiber (MOF) Bragg-Grating Optofluidic System. *Biosens. Bioelectron.* **2015**, *63*, 248–254, doi:10.1016/j.bios.2014.07.047.

59. Warren-Smith, S.C.; Kostecki, R.; Nguyen, L.V.; Monro, T.M. Fabrication, Splicing, Bragg Grating Writing, and Polyelectrolyte Functionalization of Exposed-Core Microstructured Optical Fibers. *Opt. Express* **2014**, *22*, 29493, doi:10.1364/oe.22.029493.

60. Schwuchow, A.; Zobel, M.; Csaki, A.; Schröder, K.; Kobelke, J.; Fritzsche, W.; Schuster, K.; Benabid, F.; Bouwmans, G.; Knight, J.C.; et al. *Photonic-Crystal Fibers*; 2006; Vol. 24, pp. 4729–4749;.

61. Khozeymeh, F.; Melli, F.; Capodaglio, S.; Corradini, R.; Benabid, F.; Vincetti, L.; Cucinotta, A. Hollow-Core Fiber-Based Biosensor: A Platform for Lab-in-Fiber Optical Biosensors for DNA Detection. *Sensors* **2022**, *22*, doi:10.3390/s22145144.

62. Pidenko, P.; Vakh, C.; Shishov, A.; Skibina, J.; Burmistrova, N.; Bulatov, A. Microstructured Optical Fibers Sensor Modified by Deep Eutectic Solvent: Liquid-Phase Microextraction and Detection in One Analytical Device. *Talanta* **2021**, *232*, doi:10.1016/j.talanta.2021.122305.

63. Shao, L.; Liu, Z.; Hu, J.; Gunawardena, D.; Tam, H.Y. Optofluidics in Microstructured Optical Fibers. *Micromachines* **2018**, *9*, doi:10.3390/mi9040145.

64. Nguyen, L.V.; Hill, K.; Warren-Smith, S.; Monro, T. Interferometric-Type Optical Biosensor Based on Exposed Core Microstructured Optical Fiber. *Sens. Actuators B Chem.* **2015**, *221*, 320–327, doi:10.1016/j.snb.2015.06.068.

65. Ermatov, T.; Petrov, Y.V.; German, S.V.; Zanishevskaya, A.A.; Shuvalov, A.A.; Atkin, V.; Zakharevich, A.; Khlebtsov, B.N.; Skibina, J.S.; Ginzburg, P.; et al. Microstructured Optical Waveguide-Based Endoscopic Probe Coated with Silica Submicron Particles. *Materials* **2019**, *12*, doi:10.3390/ma12091424.

66. Liu, X.; Ding, W.; Wang, Y.; Gao, S.; Cao, L.; Feng, X.; Wang, P. Characterization of a Liquid-Filled Nodeless Anti-Resonant Fiber for Biochemical Sensing. *Opt. Lett.* **2017**, *42*, 863, doi:10.1364/ol.42.000863.

67. Ni, W.; Yang, C.; Luo, Y.; Xia, R.; Lu, P.; Hu, D.J.J.; Danto, S.; Shum, P.P.; Wei, L. Recent Advancement of Anti-Resonant Hollow-Core Fibers for Sensing Applications. *Photonics* **2021**, *8*, doi:10.3390/photonics8040128.

68. Heck, J.R.; Miele, E.; Mouthaan, R.; Frosz, M.H.; Knowles, T.P.J.; Euser, T.G. Label-Free Monitoring of Proteins in Optofluidic Hollow-Core Photonic Crystal Fibres. *Methods Appl. Fluoresc.* **2022**, *10*, doi:10.1088/2050-6120/ac9113.

69. Shukla, S.K.; Kushwaha, C.S.; Guner, T.; Demir, M.M. Chemically Modified Optical Fibers in Advanced Technology: An Overview. *Opt. Laser Technol.* **2019**, *115*, 404–432, doi:10.1016/j.optlastec.2019.02.025.

70. Li, L.; Zhang, Y. nan; Zhou, Y.; Zheng, W.; Sun, Y.; Ma, G.; Zhao, Y. Optical Fiber Optofluidic Bio-Chemical Sensors: A Review. *Laser Photonics Rev.* **2021**, *15*, doi:10.1002/lpor.202000526.

71. Zhang, N.; Li, K.; Cui, Y.; Wu, Z.; Shum, P.P.; Auguste, J.L.; Dinh, X.Q.; Humbert, G.; Wei, L. Ultra-Sensitive Chemical and Biological Analysis: Via Specialty Fibers with Built-in Microstructured Optofluidic Channels. *Lab. Chip* **2018**, *18*, 655–661, doi:10.1039/c7lc01247k.

72. Wang, Y.; Gao, R.; Xin, X. Hollow-Core Fiber Refractive Index Sensor with High Sensitivity and Large Dynamic Range Based on a Multiple Mode Transmission Mechanism. *Opt Express* **2021**, *29*, 19703–19714, doi:10.1364/OE.426705.

73. Chen, L.; Su, Q.; Liu, S.; Li, L. Infiltrated Hollow Core Fiber Interferometer for High Sensitive Temperature and Refractive Index Sensing. *Optik* **2021**, *243*, 167336, doi:https://doi.org/10.1016/j.ijleo.2021.167336.

74. Zhao, Y.; Li, X.-G.; Cai, L.; Zhang, Y.-N. Measurement of RI and Temperature Using Composite Interferometer With Hollow-Core Fiber and Photonic Crystal Fiber. *IEEE Trans. Instrum. Meas.* **2016**, *65*, 2631–2636, doi:10.1109/TIM.2016.2584390.

75. Liu, X.; WANG, Q.; WANG, D.N. Ultra Compact and Sensitive Optical Fiber Interferometric Refractive Index Sensor. *Optik* **2022**, *254*, 168642, doi:https://doi.org/10.1016/j.ijleo.2022.168642.

76. Zheng, K.; Shang, L. High-Linearity Refractive Index Sensor Based on Analyte-Filled Defect Hollow Core Bragg Fiber. *IEEE Photonics Technol. Lett.* **2017**, *29*, 1391–1394, doi:10.1109/LPT.2017.2723519.

77. Alam, M.K.; Vadivel, K.; Natesan, A.; Sghaireen, M.G.; Ganji, K.K.; Srivastava, K.C.; Nashwan, S.; Khader, Y. Design of Highly Sensitive Biosensors Using Hollow-Core Microstructured Fibers for Plasma Sensing in Aids with Human Metabolism. *Opt. Quantum Electron.* **2023**, *55*, 188, doi:10.1007/s11082-022-04514-w.

78. Gao, R.; Lu, D.; Cheng, J.; Qi, Z. Fiber Optic Refractive Index Sensor Using Optofluidic Anti-Resonant Reflecting Guidance. In Proceedings of the AOPC 2017: Fiber Optic Sensing and Optical Communications; Zhao, Z.-S., Wei, L., Liao, Y., Zhang, W., Jiang, D., Wang, W., Grattan, K.T.V., Eds.; SPIE, 2017; Vol. 10464, p. 104640N.

79. *Practical Raman Spectroscopy*; Gardiner, D.J., Graves, P.R., Eds.; Springer Berlin Heidelberg: Berlin, Heidelberg, 1989; ISBN 978-3-540-50254-8.

80. Cialla-May, D.; Krafft, C.; Rösch, P.; Deckert-Gaudig, T.; Frosch, T.; Jahn, I.J.; Pahlow, S.; Stiebing, C.; Meyer-Zedler, T.; Bocklitz, T.; et al. Raman Spectroscopy and Imaging in Bioanalytics. *Anal. Chem.* **2022**, *94*, 86–119, doi:10.1021/acs.analchem.1c03235.

81. Lawson, E.E.; Barry, B.W.; Williams, A.C.; Edwards, H.G.M. Biomedical Applications of Raman Spectroscopy. *J. Raman Spectrosc.* **1997**, *28*, 111–117, doi:10.1002/(SICI)1097-4555(199702)28:2/3<111::AID-JRS87>3.0.CO;2-Z.

82. Ferraro, J.R.; Nakamoto, K.; Brown, C.W. *Introductory Raman Spectroscopy*; 2nd ed.; Academic Press: Amsterdam ; Boston, 2003; ISBN 978-0-12-254105-6.

83. Knebl, A.; Yan, D.; Popp, J.; Frosch, T. Fiber Enhanced Raman Gas Spectroscopy. *TrAC - Trends Anal. Chem.* **2018**, *103*, 230–238, doi:10.1016/j.trac.2017.12.001.

84. Markin, A.V.; Markina, N.E.; Goryacheva, I.Y. Raman Spectroscopy Based Analysis inside Photonic-Crystal Fibers. *TrAC - Trends Anal. Chem.* **2017**, *88*, 185–197, doi:10.1016/j.trac.2017.01.003.

85. Yan, D.; Popp, J.; Pletz, M.W.; Frosch, T. Highly Sensitive Broadband Raman Sensing of Antibiotics in Step-Index Hollow-Core Photonic Crystal Fibers. *ACS Photonics* **2017**, *4*, 138–145, doi:10.1021/acsphotonics.6b00688.

86. Yang, X.; Zhang, A.Y.; Wheeler, D.A.; Bond, T.C.; Gu, C.; Li, Y. Direct Molecule-Specific Glucose Detection by Raman Spectroscopy Based on Photonic Crystal Fiber. *Anal. Bioanal. Chem.* **2012**, *402*, 687–691, doi:10.1007/s00216-011-5575-1.

87. Khetani, A.; Riordon, J.; Tiwari, V.; Momenpour, A.; Godin, M.; Anis, H. Hollow Core Photonic Crystal Fiber as a Reusable Raman Biosensor. *Opt. Express* **2013**, *21*, 12340, doi:10.1364/oe.21.012340.

88. Merdalimova, A.A.; Rudakovskaya, P.G.; Ermatov, T.I.; Smirnov, A.S.; Kosolobov, S.S.; Skibina, J.S.; Demina, P.A.; Khlebtsov, B.N.; Yashchenok, A.M.; Gorin, D.A. SERS Platform Based on Hollow-Core Microstructured Optical Fiber: Technology of UV-Mediated Gold Nanoparticle Growth. *Biosensors* **2022**, *12*, doi:10.3390/bios12010019.

89. Shi, C.; Zhang, Y.; Gu, C.; Seballos, L.; Zhang, J.Z. Low Concentration Biomolecular Detection Using Liquid Core Photonic Crystal Fiber (LCPCF) SERS Sensor. In Proceedings of the Optical Fibers and Sensors for Medical Diagnostics and Treatment Applications VIII; SPIE, February 7 2008; Vol. 6852, p. 685204.

90. Hanf, S.; Bögözi, T.; Keiner, R.; Frosch, T.; Popp, J. Fast and Highly Sensitive Fiber-Enhanced Raman Spectroscopic Monitoring of Molecular H_2 and CH_4 for Point-of-Care Diagnosis of Malabsorption Disorders in Exhaled Human Breath. *Anal. Chem.* **2015**, *87*, 982–988, doi:10.1021/ac503450y.

91. Hanf, S.; Keiner, R.; Yan, D.; Popp, J.; Frosch, T. Fiber-Enhanced Raman Multigas Spectroscopy: A Versatile Tool for Environmental Gas Sensing and Breath Analysis. *Anal. Chem.* **2014**, *86*, 5278–5285, doi:10.1021/ac404162w.

92. Langer, J.; Jimenez De Aberasturi, D.; Aizpurua, J.; Alvarez-Puebla, R.A.; Auguié, B.; Baumberg, J.J.; Bazan, G.C.; Bell, S.E.J.; Boisen, A.; Brolo, A.G.; et al. Present and Future of Surface-Enhanced Raman Scattering. *ACS Nano* **2020**, *14*, 28–117, doi:10.1021/acsnano.9b04224.

93. Cox, F.M.; Argyros, A.; Large, M.C.J.; Kalluri, S. Surface Enhanced Raman Scattering in a Hollow Core Microstructured Optical Fiber. *Opt. Express* **2007**, *15*, 13675, doi:10.1364/OE.15.013675.

94. Yang, X.; Shi, C.; Wheeler, D.; Newhouse, R.; Chen, B.; Zhang, J.Z.; Gu, C. High-Sensitivity Molecular Sensing Using Hollow-Core Photonic Crystal Fiber and Surface-Enhanced Raman Scattering. *J. Opt. Soc. Am. A* **2010**, *27*, 977, doi:10.1364/JOSAA.27.000977.

95. Hunter, R.; Sohi, A.N.; Khatoon, Z.; Berthiaume, V.R.; Alarcon, E.I.; Godin, M.; Anis, H. Optofluidic Label-Free SERS Platform for Rapid Bacteria Detection in Serum. *Sens. Actuators B Chem.* **2019**, *300*, doi:10.1016/j.snb.2019.126907.

96. Sun, Z.; Kang, C.; Fang, X.; Liu, H.; Guo, J.; Zhang, X. A SERS-Active Capillary for Direct Molecular Trace Detection in Liquids. *Nanoscale Adv.* **2021**, *3*, 2617–2622, doi:10.1039/d1na00082a.

97. Zhang, Y.; Shi, C.; Gu, C.; Seballos, L.; Zhang, J.Z. Liquid Core Photonic Crystal Fiber Sensor Based on Surface Enhanced Raman Scattering. *Appl. Phys. Lett.* **2007**, *90*, 193504, doi:10.1063/1.2738185.

98. Eftekhari, F.; Lee, A.; Kumacheva, E.; Helmy, A.S. Examining Metal Nanoparticle Surface Chemistry Using Hollow-Core, Photonic-Crystal, Fiber-Assisted SERS. *Opt. Lett.* **2012**, *37*, 680, doi:10.1364/OL.37.000680.

99. Khetani, A.; Tiwari, V.S.; Momenpour, A.; Anis, H. Monitoring of Adenosine within Hollow Core Photonic Crystal Fiber by Surface Enhanced Raman Scattering (SERS). In Proceedings of the 2011 11th IEEE International Conference on Nanotechnology; IEEE: Portland, OR, USA, August 2011; pp. 973–977.

100. Tiwari, V.S.; Khetani, A.; Naji, M.; Anis, H. Study of Surface Enhanced Raman Scattering (SERS) within Hollow Core Photonic Crystal Fiber. In Proceedings of the 2009 IEEE Sensors; IEEE: Christchurch, New Zealand, October 2009; pp. 367–370.

101. Yang, X.; Gu, C.; Qian, F.; Li, Y.; Zhang, J.Z. Highly Sensitive Detection of Proteins and Bacteria in Aqueous Solution Using Surface-Enhanced Raman

Scattering and Optical Fibers. *Anal. Chem.* **2011**, *83*, 5888–5894, doi:10.1021/ac200707t.

102. Dinish, U.S.; Fu, C.Y.; Soh, K.S.; Ramaswamy, B.; Kumar, A.; Olivo, M. Highly Sensitive SERS Detection of Cancer Proteins in Low Sample Volume Using Hollow Core Photonic Crystal Fiber. *Biosens. Bioelectron.* **2012**, *33*, 293–298, doi:10.1016/j.bios.2011.12.056.

103. Dinish, U.S.; Balasundaram, G.; Chang, Y.T.; Olivo, M. Sensitive Multiplex Detection of Serological Liver Cancer Biomarkers Using SERS-Active Photonic Crystal Fiber Probe. *J. Biophotonics* **2014**, *7*, 956–965, doi:10.1002/jbio.201300084.

104. Kahraman, M.; Mullen, E.R.; Korkmaz, A.; Wachsmann-Hogiu, S. Fundamentals and Applications of SERS-Based Bioanalytical Sensing. *Nanophotonics* **2017**, *6*, 831–852, doi:10.1515/nanoph-2016-0174.

105. Geng, Y.; Xu, Y.; Tan, X.; Wang, L.; Li, X.; Du, Y.; Hong, X. A Simplified Hollow-Core Photonic Crystal Fiber SERS Probe with a Fully Filled Photoreduction Silver Nanoprism. *Sensors* **2018**, *18*, 1726, doi:10.3390/s18061726.

106. Li, P.; Long, F.; Chen, W.; Chen, J.; Chu, P.K.; Wang, H. Fundamentals and Applications of Surface-Enhanced Raman Spectroscopy–Based Biosensors. *Curr. Opin. Biomed. Eng.* **2020**, *13*, 51–59, doi:10.1016/j.cobme.2019.08.008.

107. Schøler, L.V.; Reinert, T.; Ørntoft, M.-B.W.; Kassentoft, C.G.; Árnadóttir, S.S.; Vang, S.; Nordentoft, I.; Knudsen, M.; Lamy, P.; Andreasen, D.; et al. Clinical Implications of Monitoring Circulating Tumor DNA in Patients with Colorectal Cancer. *Clin. Cancer Res.* **2017**, *23*, 5437–5445, doi:10.1158/1078-0432.CCR-17-0510.

108. Cheng, F.; Su, L.; Qian, C. Circulating Tumor DNA: A Promising Biomarker in the Liquid Biopsy of Cancer. *Oncotarget* **2016**, *7*, 48832–48841, doi:10.18632/oncotarget.9453.

109. Johann, D.J.; Steliga, M.; Shin, I.J.; Yoon, D.; Arnaoutakis, K.; Hutchins, L.; Liu, M.; Liem, J.; Walker, K.; Pereira, A.; et al. Liquid Biopsy and Its Role in an Advanced Clinical Trial for Lung Cancer. *Exp. Biol. Med.* **2018**, *243*, 262–271, doi:10.1177/1535370217750087.

110. Gale, D.; Lawson, A.R.J.; Howarth, K.; Madi, M.; Durham, B.; Smalley, S.; Calaway, J.; Blais, S.; Jones, G.; Clark, J.; et al. Development of a Highly Sensitive Liquid Biopsy Platform to Detect Clinically-Relevant Cancer Mutations at Low Allele Fractions in Cell-Free DNA. *PLOS ONE* **2018**, *13*, e0194630, doi:10.1371/journal.pone.0194630.

111. Zhao, Z.; Wijerathne, H.; Godwin, A.K.; Soper, S.A. Isolation and Analysis Methods of Extracellular Vesicles (EVs). *Extracell. Vesicles Circ. Nucleic Acids* **2021**, doi:10.20517/evcna.2021.07.

112. Théry, C.; Witwer, K.W.; Aikawa, E.; Alcaraz, M.J.; Anderson, J.D.; Andriantsitohaina, R.; Antoniou, A.; Arab, T.; Archer, F.; Atkin-Smith, G.K.; et al. Minimal Information for Studies of Extracellular Vesicles 2018 (MISEV2018): A Position Statement of the International Society for Extracellular Vesicles and Update of the MISEV2014 Guidelines. *J. Extracell. Vesicles* **2018**, *7*, doi:10.1080/20013078.2018.1535750.

113. Tkach, M.; Théry, C. Communication by Extracellular Vesicles: Where We Are and Where We Need to Go. *Cell* **2016**, *164*, 1226–1232, doi:10.1016/j.cell.2016.01.043.

114. Tkach, M.; Kowal, J.; Théry, C. Why the Need and How to Approach the Functional Diversity of Extracellular Vesicles. *Philos. Trans. R. Soc. B Biol. Sci.* **2017**, *373*, 20160479, doi:10.1098/rstb.2016.0479.

115. Serrano-Pertierra, E.; Oliveira-Rodríguez, M.; Rivas, M.; Oliva, P.; Villafani, J.; Navarro, A.; Blanco-López, M.C.; Cernuda-Morollón, E. Characterization of Plasma-Derived Extracellular Vesicles Isolated by Different Methods: A Comparison Study. *Bioeng. Basel Switz.* **2019**, *6*, doi:10.3390/BIOENGINEERING6010008.

116. Tian, Y.; Gong, M.; Hu, Y.; Liu, H.; Zhang, W.; Zhang, M.; Hu, X.; Aubert, D.; Zhu, S.; Wu, L.; et al. Quality and Efficiency Assessment of Six Extracellular Vesicle Isolation Methods by Nano-Flow Cytometry. *J. Extracell. Vesicles* **2020**, *9*, 1697028, doi:10.1080/20013078.2019.1697028.

117. Kang, H.; Kim, J.; Park, J. Methods to Isolate Extracellular Vesicles for Diagnosis. *Micro Nano Syst. Lett.* **2017**, *5*, 1–11, doi:10.1186/S40486-017-0049-7/FIGURES/7.

118. Konoshenko, M.Y.; Lekchnov, E.A.; Vlassov, A. V.; Laktionov, P.P. Isolation of Extracellular Vesicles: General Methodologies and Latest Trends. *BioMed Res. Int.* **2018**, *2018*, doi:10.1155/2018/8545347.

119. Théry, C.; Amigorena, S.; Raposo, G.; Clayton, A. Isolation and Characterization of Exosomes from Cell Culture Supernatants and Biological Fluids. *Curr. Protoc. Cell Biol.* **2006**, *30*, 3.22.1-3.22.29, doi:10.1002/0471143030.CB0322S30.

120. Busatto, S.; Vilanilam, G.; Ticer, T.; Lin, W.L.; Dickson, D.W.; Shapiro, S.; Bergese, P.; Wolfram, J. Tangential Flow Filtration for Highly Efficient Concentration of Extracellular Vesicles from Large Volumes of Fluid. *Cells 2018 Vol 7 Page 273* **2018**, *7*, 273, doi:10.3390/CELLS7120273.

121. Zhang, K.; Yue, Y.; Wu, S.; Liu, W.; Shi, J.; Zhang, Z. Rapid Capture and Nondestructive Release of Extracellular Vesicles Using Aptamer-Based Magnetic Isolation. *ACS Sens.* **2019**, *4*, 1245–1251, doi:10.1021/ACSSENSORS.9B00060.

122. Zabegina, L.; Nazarova, I.; Knyazeva, M.; Nikiforova, N.; Slyusarenko, M.; Titov, S.; Vasilyev, D.; Sleptsov, I.; Malek, A. MiRNA Let-7 from TPO(+) Extracellular Vesicles Is a Potential Marker for a Differential Diagnosis of Follicular Thyroid Nodules. *Cells 2020 Vol 9 Page 1917* **2020**, *9*, 1917, doi:10.3390/CELLS9081917.

123. Zheng, H.; Ding, Q.; Li, C.; Chen, W.; Chen, X.; Lin, Q.; Wang, D.; Weng, Y.; Lin, D. Recent Progress in Surface-Enhanced Raman Spectroscopy-Based Biosensors for the Detection of Extracellular Vesicles. *Anal. Methods* **2022**, *14*, 4161–4173, doi:10.1039/D2AY01339H.

124. Dong, S.; Wang, Y.; Liu, Z.; Zhang, W.; Yi, K.; Zhang, X.; Zhang, X.; Jiang, C.; Yang, S.; Wang, F.; et al. Beehive-Inspired Macroporous SERS Probe for Cancer Detection through Capturing and Analyzing Exosomes in Plasma. *ACS Appl. Mater. Interfaces* **2020**, *12*, 5136–5146, doi:10.1021/acsami.9b21333.

125. Russo, M.; Tirinato, L.; Scionti, F.; Coluccio, M.L.; Perozziello, G.; Riillo, C.; Mollace, V.; Gratteri, S.; Malara, N.; Di Martino, M.T.; et al. Raman Spectroscopic Stratification of Multiple Myeloma Patients Based on Exosome Profiling. *ACS Omega* **2020**, *5*, 30436–30443, doi:10.1021/acsomega.0c03813.

126. Liu, Y.; Zhang, W.; Phan, T.H.; Chrzanowski, W.; Rodger, A.; Wang, Y. Positively Charged Gold–Silver Nanostar Enabled Molecular Characterization of Cancer Associated Extracellular Vesicles. *Anal. Methods* **2020**, *12*, 5908–5915, doi:10.1039/D0AY01770A.

127. Carmicheal, J.; Hayashi, C.; Huang, X.; Liu, L.; Lu, Y.; Krasnoslobodtsev, A.; Lushnikov, A.; Kshirsagar, P.G.; Patel, A.; Jain, M.; et al. Label-Free Characterization of Exosome via Surface Enhanced Raman Spectroscopy for the Early Detection of Pancreatic Cancer. *Nanomedicine Nanotechnol. Biol. Med.* **2019**, *16*, 88–96, doi:10.1016/j.nano.2018.11.008.

128. Stremersch, S.; Marro, M.; Pinchasik, B.E.; Baatsen, P.; Hendrix, A.; De Smedt, S.C.; Loza-Alvarez, P.; Skirtach, A.G.; Raemdonck, K.; Braeckmans, K. Identification of Individual Exosome-like Vesicles by Surface Enhanced Raman Spectroscopy. *Small* **2016**, *12*, 3292–3301, doi:10.1002/smll.201600393.

129. Shin, H.; Oh, S.; Hong, S.; Kang, M.; Kang, D.; Ji, Y.; Choi, B.H.; Kang, K.-W.; Jeong, H.; Park, Y.; et al. Early-Stage Lung Cancer Diagnosis by Deep Learning-Based Spectroscopic Analysis of Circulating Exosomes. *ACS Nano* **2020**, *14*, 5435–5444, doi:10.1021/acsnano.9b09119.

130. Lee, W.; Lenferink, A.T.M.; Otto, C.; Offerhaus, H.L. Classifying Raman Spectra of Extracellular Vesicles Based on Convolutional Neural Networks for Prostate Cancer Detection. *J. Raman Spectrosc.* **2020**, *51*, 293–300, doi:10.1002/jrs.5770.

131. Wang, J.; Kao, Y.; Zhou, Q.; Wuethrich, A.; Stark, M.S.; Schaider, H.; Soyer, H.P.; Lin, L.L.; Trau, M. An Integrated Microfluidic-SERS Platform Enables Sensitive Phenotyping of Serum Extracellular Vesicles in Early Stage Melanomas. *Adv. Funct. Mater.* **2022**, *32*, 2010296, doi:10.1002/adfm.202010296.

132. Wang, J.; Wuethrich, A.; Sina, A.A.I.; Lane, R.E.; Lin, L.L.; Wang, Y.; Cebon, J.; Behren, A.; Trau, M. Tracking Extracellular Vesicle Phenotypic Changes Enables Treatment Monitoring in Melanoma. *Sci. Adv.* **2020**, *6*, eaax3223, doi:10.1126/sciadv.aax3223.

133. Zong, S.; Wang, L.; Chen, C.; Lu, J.; Zhu, D.; Zhang, Y.; Wang, Z.; Cui, Y. Facile Detection of Tumor-Derived Exosomes Using Magnetic Nanobeads and SERS Nanoprobes. *Anal. Methods* **2016**, *8*, 5001–5008, doi:10.1039/c6ay00406g.

134. Tian, Y.F.; Ning, C.F.; He, F.; Yin, B.C.; Ye, B.C. Highly Sensitive Detection of Exosomes by SERS Using Gold nanostar@Raman Reporter@nanoshell Structures Modified with a Bivalent Cholesterol-Labeled DNA Anchor. *Analyst* **2018**, *143*, 4915–4922, doi:10.1039/c8an01041b.

135. Weng, Z.; Zong, S.; Wang, Y.; Li, N.; Li, L.; Lu, J.; Wang, Z.; Chen, B.; Cui, Y. Screening and Multiple Detection of Cancer Exosomes Using an SERS-Based Method. *Nanoscale* **2018**, *10*, 9053–9062, doi:10.1039/c7nr09162a.

136. Li, T.D.; Zhang, R.; Chen, H.; Huang, Z.P.; Ye, X.; Wang, H.; Deng, A.M.; Kong, J.L. An Ultrasensitive Polydopamine Bi-Functionalized SERS Immunoassay for Exosome-Based Diagnosis and Classification of Pancreatic Cancer. *Chem. Sci.* **2018**, *9*, 5372–5382, doi:10.1039/c8sc01611a.

137. Mitragotri, S. Healing Sound: The Use of Ultrasound in Drug Delivery and Other Therapeutic Applications. *Nat. Rev. Drug Discov.* **2005**, *4*, 255–260, doi:10.1038/nrd1662.

138. Wells, P.N.T. Ultrasound Imaging. *Phys. Med. Biol.* **2006**, *51*, R83–R98, doi:10.1088/0031-9155/51/13/R06.

139. Cosgrove, D. Ultrasound Contrast Agents: An Overview. *Eur. J. Radiol.* **2006**, *60*, 324–330, doi:10.1016/j.ejrad.2006.06.022.

140. Aldrich, J.E. Basic Physics of Ultrasound Imaging: *Crit. Care Med.* **2007**, *35*, S131–S137, doi:10.1097/01.CCM.0000260624.99430.22.

141. Paefgen, V.; Doleschel, D.; Kiessling, F. Evolution of Contrast Agents for Ultrasound Imaging and Ultrasound-Mediated Drug Delivery. *Front. Pharmacol.* **2015**, *6*, doi:10.3389/fphar.2015.00197.

142. Kooiman, K.; Vos, H.J.; Versluis, M.; De Jong, N. Acoustic Behavior of Microbubbles and Implications for Drug Delivery. *Adv. Drug Deliv. Rev.* **2014**, *72*, 28–48, doi:10.1016/j.addr.2014.03.003.

143. Rudakovskaya, P.G.; Barmin, R.A.; Kuzmin, P.S.; Fedotkina, E.P.; Sencha, A.N.; Gorin, D.A. Microbubbles Stabilized by Protein Shell: From Pioneering Ultrasound Contrast Agents to Advanced Theranostic Systems. *Pharmaceutics* **2022**, *14*, 1236, doi:10.3390/pharmaceutics14061236.

144. Rudakovskaya, P.G.; Barmin, R.A.; Kuzmin, P.S.; Fedotkina, E.P.; Sencha, A.N.; Gorin, D.A. Microbubbles Stabilized by Protein Shell: From Pioneering Ultrasound Contrast Agents to Advanced Theranostic Systems. *Pharmaceutics* **2022**, *14*, doi:10.3390/pharmaceutics14061236.

145. Mujtaba, J.; Liu, J.; Dey, K.K.; Li, T.; Chakraborty, R.; Xu, K.; Makarov, D.; Barmin, R.A.; Gorin, D.A.; Tolstoy, V.P.; et al. Micro-Bio-Chemo-Mechanical-Systems: Micromotors, Microfluidics, and Nanozymes for Biomedical Applications. *Adv. Mater.* **2021**, *33*, 2007465, doi:10.1002/adma.202007465.

146. *Micro- and Nanobubbles: Fundamentals and Applications*; Tsuge, H., Ed.; Pan Stanford Publishing: Singapore, 2014; ISBN 978-981-4463-10-2.

147. Estifeeva, T.M.; Barmin, R.A.; Rudakovskaya, P.G.; Nechaeva, A.M.; Luss, A.L.; Mezhuev, Y.O.; Chernyshev, V.S.; Krivoborodov, E.G.; Klimenko, O.A.; Sindeeva, O.A.; et al. Hybrid (Bovine Serum Albumin)/Poly(N-Vinyl-2-Pyrrolidone- Co-Acrylic Acid)-Shelled Microbubbles as Advanced Ultrasound Contrast Agents. *ACS Appl. Bio Mater.* **2022**, *5*, 3338–3348, doi:10.1021/acsabm.2c00331.

148. An, F.-F.; Zhang, X.-H. Strategies for Preparing Albumin-Based Nanoparticles for Multifunctional Bioimaging and Drug Delivery. *Theranostics* **2017**, *7*, 3667–3689, doi:10.7150/thno.19365.

149. Kudarha, R.R.; Sawant, K.K. Albumin Based Versatile Multifunctional Nanocarriers for Cancer Therapy: Fabrication, Surface Modification, Multimodal Therapeutics and Imaging Approaches. *Mater. Sci. Eng. C* **2017**, *81*, 607–626, doi:10.1016/j.msec.2017.08.004.

150. Robinson, B.V.; Sullivan, F.M.; Borzelleca, J.F.; Schwartz, S.L. *PVP: A Critical Review of the Kinetics and Toxicology of Polyvinylpyrrolidone (Povidone)*; 1st ed.; Routledge, 2018; ISBN 978-0-203-74167-2.

151. Pound, G.; McKenzie, J.M.; Lange, R.F.M.; Klumperman, B. Polymer–Protein Conjugates from ω-Aldehyde Endfunctional Poly(N-Vinylpyrrolidone) Synthesised via Xanthate-Mediated Living Radical Polymerisation. *Chem. Commun.* **2008**, 3193, doi:10.1039/b803952f.

152. Ullah, M.; Kodam, S.P.; Mu, Q.; Akbar, A. Microbubbles versus Extracellular Vesicles as Therapeutic Cargo for Targeting Drug Delivery. *ACS Nano* **2021**, *15*, 3612–3620, doi:10.1021/acsnano.0c10689.

153. Kiessling, F.; Gaetjens, J.; Palmowski, M. Application of Molecular Ultrasound for Imaging Integrin Expression. *Theranostics* **2011**, *1*, 127–134, doi:10.7150/thno/v01p0127.

154. Aw, M.S.; Paniwnyk, L.; Losic, D. The Progressive Role of Acoustic Cavitation for Non-Invasive Therapies, Contrast Imaging and Blood-Tumor Permeability Enhancement. *Expert Opin. Drug Deliv.* **2016**, *13*, 1383–1396, doi:10.1080/17425247.2016.1192123.

155. Liu, Y.; Gong, Y.; Xie, W.; Huang, A.; Yuan, X.; Zhou, H.; Zhu, X.; Chen, X.; Liu, J.; Liu, J.; et al. Microbubbles in Combination with Focused Ultrasound for the Delivery of Quercetin-Modified Sulfur Nanoparticles through the Blood Brain Barrier into the Brain Parenchyma and Relief of Endoplasmic Reticulum Stress to

Treat Alzheimer's Disease. *Nanoscale* **2020**, *12*, 6498–6511, doi:10.1039/C9NR09713A.

156. Liu, X.; Naomi, S.S.M.; Sharon, W.L.; Russell, E.J. The Applications of Focused Ultrasound (FUS) in Alzheimer's Disease Treatment: A Systematic Review on Both Animal and Human Studies. *Aging Dis.* **2021**, *12*, 1977, doi:10.14336/AD.2021.0510.

157. Wang, Y.; Gao, R.; Xin, X. Hollow-Core Fiber Refractive Index Sensor with High Sensitivity and Large Dynamic Range Based on a Multiple Mode Transmission Mechanism. *Opt. Express* **2021**, *29*, 19703, doi:10.1364/oe.426705.

158. Zeisberger, M.; Schmidt, M.A. Analytic Model for the Complex Effective Index of the Leaky Modes of Tube-Type Anti-Resonant Hollow Core Fibers. *Sci. Rep.* **2017**, *7*, 11761, doi:10.1038/s41598-017-12234-5.

159. Snyder, A.W.; Love, J.D. *Optical Waveguide Theory*; Springer US: Boston, MA, 1984; ISBN 978-0-412-24250-2.

160. Hu, J.; Menyuk, C.R. Understanding Leaky Modes: Slab Waveguide Revisited. *Adv. Opt. Photonics* **2009**, *1*, 58, doi:10.1364/AOP.1.000058.

161. Kolyadin, A.N.; Kosolapov, A.F.; Pryamikov, A.D.; Biriukov, A.S.; Plotnichenko, V.G.; Dianov, E.M. Light Transmission in Negative Curvature Hollow Core Fiber in Extremely High Material Loss Region. *Opt. Express* **2013**, *21*, 9514, doi:10.1364/OE.21.009514.

162. Xie, S.; Pennetta, R.; Russell, P.St.J. Self-Alignment of Glass Fiber Nanospike by Optomechanical Back-Action in Hollow-Core Photonic Crystal Fiber. *Optica* **2016**, *3*, 277, doi:10.1364/OPTICA.3.000277.

163. Noskov, R.E.; Zanishevskaya, A.A.; Shuvalov, A.A.; German, S.V.; Inozemtseva, O.A.; Kochergin, T.P.; Lazareva, E.N.; Tuchin, V.V.; Ginzburg, P.; Skibina, J.S.; et al. Enabling Magnetic Resonance Imaging of Hollow-Core Microstructured Optical Fibers via Nanocomposite Coating. *Opt. Express* **2019**, *27*, 9868, doi:10.1364/oe.27.009868.

164. Le Ru, E.C.; Etchegoin, P.G. *Principles of Surface-Enhanced Raman Spectroscopy*; 2009; ISBN 978-0-444-52779-0.

165. Murray, W.A.; Barnes, W.L. Plasmonic Materials. *Adv. Mater.* **2007**, *19*, 3771–3782, doi:10.1002/adma.200700678.

166. Gray, S.K. Theory and Modeling of Plasmonic Structures. *J. Phys. Chem. C* **2013**, *117*, 1983–1994, doi:10.1021/jp309664c.

167. Duff, D.G.; Baiker, A.; Edwards, P.P. A New Hydrosol of Gold Clusters. 1. Formation and Particle Size Variation. *Langmuir* **1993**, *9*, 2301–2309.

168. Turkevich, J.; Stevenson, P.C.; Hillier, J. A Study of the Nucleation and Growth Processes in the Synthesis of Colloidal Gold. *Discuss. Faraday Soc.* **1951**, *11*, 55–75, doi:10.1039/DF9511100055.

169. Nechaeva, A.M.; Artyukhov, A.A.; Luss, A.L.; Shtilman, M.I.; Svistunova, A.Y.; Motyakin, M.V.; Levina, I.I.; Krivoborodov, E.G.; Toropygin, I.Y.; Chistyakov, E.M.; et al. The Synthesis and Properties of a New Carrier for Paclitaxel and Doxorubicin Based on the Amphiphilic Copolymer of N-Vinyl-2-Pyrrolidone and Acrylic Acid. *Macromol. Chem. Phys.* **2022**, *223*, 2200081, doi:10.1002/MACP.202200081.

170. Artyukhov, A.A.; Nechaeva, A.M.; Shtilman, M.I.; Chistyakov, E.M.; Svistunova, A.Y.; Bagrov, D.V.; Kuskov, A.N.; Docea, A.O.; Tsatsakis, A.M.; Gurevich, L. Nanoaggregates of Biphilic Carboxyl-Containing Copolymers as Carriers for Ionically Bound Doxorubicin. *Materials* **2022**, *15*, 7136.

171. Upadhyay, A.; Dalvi, S.V. Microbubble Formulations: Synthesis, Stability, Modeling and Biomedical Applications. *Ultrasound Med. Biol.* **2019**, *45*, 301–343, doi:https://doi.org/10.1016/j.ultrasmedbio.2018.09.022.

172. Sossna, M.; Hollas, M.; Schaper, J.; Scheper, T. Structural Development of Asymmetric Cellulose Acetate Microfiltration Membranes Prepared by a Single-Layer Dry-Casting Method. *J. Membr. Sci.* **2007**, *289*, 7–14, doi:10.1016/j.memsci.2006.11.024.

173. Kuzin, A.; Chernyshev, V.; Kovalyuk, V.; An, P.; Golikov, A.; Svyatodukh, S.; Perevoschikov, S.; Florya, I.; Schulga, A.; Deyev, S.; et al. Real-Time Surface Functionalization of a Nanophotonic Sensor for Liquid Biopsy. *Appl. Phys. Lett.* **2023**, *123*, 193702, doi:10.1063/5.0167631.

174. Obeed, H.H.; Tahir, K.J.; Ridha, N.J.; Alosfur, F.K.M.; Madlol, R. Linear and Nonlinear Optical Properties of Rhodamine 6G. *IOP Conf. Ser. Mater. Sci. Eng.* **2020**, *928*, 072024, doi:10.1088/1757-899X/928/7/072024.

175. Hirayama, K.; Akashi, S.; Furuya, M.; Fukuhara, K. Rapid Confirmation and Revision of the Primary Structure of Bovine Serum Albumin by ESIMS and Frit-FAB LC/MS. *Biochem. Biophys. Res. Commun.* **1990**, *173*, 639–646, doi:10.1016/S0006-291X(05)80083-X.

176. Merdalimova, A.; Barmin, R.; Vorobev, V.; Terentyeva, D.; German, S.; Chernyshev, V.; Maslov, O.; Skibina, Y. Two − in − One Sensor of Refractive Index and Raman Scattering Using Hollow − Core Microstructured Optical Fibers for Colloid Characterization. *Colloids and Surfaces B: Biointerfaces*.

177. Hernández, B.; Pflüger, F.; Kruglik, S.G.; Ghomi, M. Characteristic Raman Lines of Phenylalanine Analyzed by a Multiconformational Approach. *J. Raman Spectrosc.* **2013**, *44*, 827–833, doi:10.1002/jrs.4290.

178. Lin, V.J.C.; Koenig, J.L. Raman Studies of Bovine Serum Albumin. *Biopolymers* **1976**, *15*, 203–218, doi:10.1002/bip.1976.360150114.

179. Lee, K.S.; Landry, Z.; Pereira, F.C.; Wagner, M.; Berry, D.; Huang, W.E.; Taylor, G.T.; Kneipp, J.; Popp, J.; Zhang, M.; et al. Raman Microspectroscopy for Microbiology. *Nat. Rev. Methods Primer* **2021**, *1*, 80, doi:10.1038/s43586-021-00075-6.

180. Szekeres, G.P.; Kneipp, J. SERS Probing of Proteins in Gold Nanoparticle Agglomerates. *Front. Chem.* **2019**, *7*, 1–10, doi:10.3389/fchem.2019.00030.

181. Rygula, A.; Majzner, K.; Marzec, K.M.; Kaczor, A.; Pilarczyk, M.; Baranska, M. Raman Spectroscopy of Proteins: A Review. *J. Raman Spectrosc.* **2013**, *44*, 1061–1076, doi:10.1002/jrs.4335.

182. Nemecek, D.; Stepanek, J.; Thomas, G.J. *Raman Spectroscopy of Proteins and Nucleoproteins*; 2013; ISBN 0-471-14086-4.

183. Yang, X.; Zhang, A.Y.; Wheeler, D.A.; Bond, T.C.; Gu, C.; Li, Y. Direct Molecule-Specific Glucose Detection by Raman Spectroscopy Based on Photonic Crystal Fiber. *Anal. Bioanal. Chem.* **2012**, *402*, 687–691, doi:10.1007/s00216-011-5575-1.

184. Khetani, A.; Riordon, J.; Tiwari, V.; Momenpour, A.; Godin, M.; Anis, H. Hollow Core Photonic Crystal Fiber as a Reusable Raman Biosensor. *Opt. Express* **2013**, *21*, 12340, doi:10.1364/oe.21.012340.

185. Chiang, C.Y.; Liu, T.Y.; Su, Y.A.; Wu, C.H.; Cheng, Y.W.; Cheng, H.W.; Jeng, R.J. Au Nanoparticles Immobilized on Honeycomb-like Polymeric Films for Surface-Enhanced Raman Scattering (SERS) Detection. *Polymers* **2017**, *9*, doi:10.3390/polym9030093.

186. Wu, C.; Chen, E.; Wei, J. Surface Enhanced Raman Spectroscopy of Rhodamine 6G on Agglomerates of Different-Sized Silver Truncated Nanotriangles. *Colloids Surf. Physicochem. Eng. Asp.* **2016**, *506*, 450–456, doi:10.1016/j.colsurfa.2016.07.020.

187. He, X.N.; Gao, Y.; Mahjouri-Samani, M.; Black, P.N.; Allen, J.; Mitchell, M.; Xiong, W.; Zhou, Y.S.; Jiang, L.; Lu, Y.F. Surface-Enhanced Raman Spectroscopy Using Gold-Coated Horizontally Aligned Carbon Nanotubes. *Nanotechnology* **2012**, *23*, doi:10.1088/0957-4484/23/20/205702.

188. Le Ru, E.C.; Etchegoin, P.G. SERS Enhancement Factors and Related Topics. In *Principles of Surface-Enhanced Raman Spectroscopy*; 2009; pp. 185–264.

189. Dinish, U.S.; Fu, C.Y.; Soh, K.S.; Ramaswamy, B.; Kumar, A.; Olivo, M. Highly Sensitive SERS Detection of Cancer Proteins in Low Sample Volume Using Hollow Core Photonic Crystal Fiber. *Biosens. Bioelectron.* **2012**, *33*, 293–298, doi:10.1016/j.bios.2011.12.056.

190. White, D.J.; Stoddart, P.R. Nanostructured Optical Fiber with Surface-Enhanced Raman Scattering Functionality. *Opt. Lett. Vol 30 Issue 6 Pp 598-600* **2005**, *30*, 598–600, doi:10.1364/OL.30.000598.

191. Ermatov, T.; Gnusov, I.; Skibina, J.; Noskov, R.E.; Gorin, D. Noncontact Characterization of Microstructured Optical Fibers Coating in Real Time. *Opt. Lett. Vol 46 Issue 19 Pp 4793-4796* **2021**, *46*, 4793–4796, doi:10.1364/OL.433208.

192. Johnson, P.B.; Christy, R.W. Optical Constants of the Noble Metals. *Phys. Rev. B* **1972**, *6*, 4370, doi:10.1103/PhysRevB.6.4370.

193. Mu, Y.; Liu, M.; Li, J.; Zhang, X. Plasmonic Hollow Fibers with Distributed Inner-Wall Hotspots for Direct SERS Detection of Flowing Liquids. *Opt. Lett.* **2021**, *46*, 1369, doi:10.1364/ol.415733.

194. Futamata, M.; Yu, Y.-Y.; Yanatori, T.; Kokubun, T. Closely Adjacent Ag Nanoparticles Formed by Cationic Dyes in Solution Generating Enormous SERS Enhancement. *J. Phys. Chem. C* **2010**, *114*, 7502–7508, doi:10.1021/jp9113877.

195. Moskovits, M. Surface Selection Rules. *J. Chem. Phys.* **1982**, *77*, 4408–4416, doi:10.1063/1.444442.

196. Watanabe, H.; Hayazawa, N.; Inouye, Y.; Kawata, S. DFT Vibrational Calculations of Rhodamine 6G Adsorbed on Silver: Analysis of Tip-Enhanced Raman Spectroscopy. *J. Phys. Chem. B* **2005**, *109*, 5012–5020, doi:10.1021/jp045771u.

197. Grohmann, A.; Riede, J.; Schmidbaur, H. Electron-Deficient Bonding at Pentacoordinate Nitrogen. *Nature* **1990**, *345*, 140–142, doi:10.1038/345140a0.

198. Xu, Y.; Bai, P.; Zhou, X.; Akimov, Y.; Png, C.E.; Ang, L.-K.; Knoll, W.; Wu, L.; Xu, Y.; Bai, P.; et al. Optical Refractive Index Sensors with Plasmonic and Photonic Structures: Promising and Inconvenient Truth. *Adv. Opt. Mater.* **2019**, *7*, 1801433, doi:10.1002/adom.201801433.

199. Hassan, J.Z.; Raza, A.; Ud, Z.; Babar, D.; Qumar, U.; Kaner, N.T.; Cassinese, A.; Hassan, † J Z; Raza, A.; Babar, Z.U.D. Open Access Article. **2023**, doi:10.1039/d2ta07653e.

200. Perlmann, G.E.; Longsworth, L.G. The Specific Refractive Increment of Some Purified Proteins. *J. Am. Chem. Soc.* **1948**, *70*, 2719–2724, doi:10.1021/ja01188a027.

201. Andersen, M.; Painter, L.R.; Nir, S. Dispersion Equation and Polarizability of Bovine Serum Albumin from Measurements of Refractive Indices. *Biopolymers* **1974**, *13*, 1261–1267, doi:10.1002/BIP.1974.360130616.

202. Sihvola, A.H. *Electromagnetic Mixing Formulas and Applications*; IEE electromagnetic waves series; Repr. with new cover.; Institution of Electrical Engineers: London, 2008; ISBN 978-0-85296-772-0.

203. Gmurman, V.E. *Teorija verojatnostej i matematičeskaja statistika*; Izd. 9., stereotip.; Vysšaja škola: Moskva, 2003; ISBN 978-5-06-004214-6.

204. Taylor, L.S.; Langkilde, F.W.; Zografi, G. Fourier Transform Raman Spectroscopic Study of the Interaction of Water Vapor with Amorphous Polymers. *J. Pharm. Sci.* **2001**, *90*, 888–901, doi:10.1002/jps.1041.

205. Hosseini-Beheshti, E.; Pham, S.; Adomat, H.; Li, N.; Tomlinson Guns, E.S. Exosomes as Biomarker Enriched Microvesicles: Characterization of Exosomal Proteins Derived from a Panel of Prostate Cell Lines with Distinct AR Phenotypes. *Mol. Cell. Proteomics* **2012**, *11*, 863–885, doi:10.1074/mcp.M111.014845.

206. McDermott, D.P. Vibrational Assignments and Normal-Coordinate Analyses of γ-Butyrolactone and 2-Pyrrolidinones. *J. Phys. Chem.* **1986**, *90*, 2569–2574, doi:10.1021/j100403a006.

207. Borodko, Y.; Habas, S.E.; Koebel, M.; Yang, P.; Frei, H.; Somorjai, G.A. Probing the Interaction of Poly(Vinylpyrrolidone) with Platinum Nanocrystals by UV - Raman and FTIR. *J. Phys. Chem. B* **2006**, *110*, 23052–23059, doi:10.1021/jp063338.

208. Sánchez-Márquez, J.A.; Fuentes-Ramírez, R.; Cano-Rodríguez, I.; Gamiño-Arroyo, Z.; Rubio-Rosas, E.; Kenny, J.M.; Rescignano, N. Membrane Made of Cellulose Acetate with Polyacrylic Acid Reinforced with Carbon Nanotubes and

Its Applicability for Chromium Removal. *Int. J. Polym. Sci.* **2015**, *2015*, doi:10.1155/2015/320631.

209. Murli, C.; Song, Y. Pressure-Induced Polymerization of Acrylic Acid: A Raman Spectroscopic Study. *J. Phys. Chem. B* **2010**, *114*, 9744–9750, doi:10.1021/jp1034757.

210. Behera, M.; Ram, S. Mechanism of Solubilizing Fullerene C60 in Presence of Poly(Vinyl Pyrrolidone) Molecules in Water. *Fuller. Nanotub. Carbon Nanostructures* **2015**, *23*, 906–916, doi:10.1080/1536383X.2015.1041109.

211. Kuriakose, M.; Borden, M.A. Microbubbles and Nanodrops for Photoacoustic Tomography. *Curr. Opin. Colloid Interface Sci.* **2021**, *55*, 101464, doi:https://doi.org/10.1016/j.cocis.2021.101464.

212. Chakraborty, B.; Basu, S. Interaction of BSA with Proflavin: A Spectroscopic Approach. *J. Lumin.* **2009**, *129*, 34–39, doi:https://doi.org/10.1016/j.jlumin.2008.07.012.

213. Barik, A.; Priyadarsini, K.I.; Mohan, H. Photophysical Studies on Binding of Curcumin to Bovine Serum Albumin¶. *Photochem. Photobiol.* **2003**, *77*, 597–603.

214. Laborde, B.; Moine-Ledoux, V.; Richard, T.; Saucier, C.; Dubourdieu, D.; Monti, J.P. PVPP−Polyphenol Complexes: A Molecular Approach. *J. Agric. Food Chem.* **2006**, *54*, 4383–4389, doi:10.1021/JF060427A.

215. Majorek, K.A.; Porebski, P.J.; Dayal, A.; Zimmerman, M.D.; Jablonska, K.; Stewart, A.J.; Chruszcz, M.; Minor, W. Structural and Immunologic Characterization of Bovine, Horse, and Rabbit Serum Albumins. *Mol. Immunol.* **2012**, *52*, 174–182, doi:https://doi.org/10.1016/j.molimm.2012.05.011.

216. Kaminski, G.A.; Friesner, R.A.; Tirado-Rives, J.; Jorgensen, W.L. Evaluation and Reparametrization of the OPLS-AA Force Field for Proteins via Comparison with Accurate Quantum Chemical Calculations on Peptides. *J. Phys. Chem. B* **2001**, *105*, 6474–6487, doi:10.1021/jp003919d.

217. Slyusarenko, M.; Nikiforova, N.; Sidina, E.; Nazarova, I.; Egorov, V.; Garmay, Y.; Merdalimova, A.; Yevlampieva, N.; Gorin, D.; Malek, A. Formation and

Evaluation of a Two-Phase Polymer System in Human Plasma as a Method for Extracellular Nanovesicle Isolation. *Polymers* **2021**, *13*, 1–16, doi:10.3390/polym13030458.

218. Chernyshev, V.S.; Chuprov-Netochin, R.N.; Tsydenzhapova, E.; Svirshchevskaya, E.V.; Poltavtseva, R.A.; Merdalimova, A.; Yashchenok, A.; Keshelava, A.; Sorokin, K.; Keshelava, V.; et al. Asymmetric Depth-Filtration: A Versatile and Scalable Method for High-Yield Isolation of Extracellular Vesicles with Low Contamination. *J. Extracell. Vesicles* **2022**, *11*, doi:10.1002/jev2.12256.

219. Krafft, C.; Wilhelm, K.; Eremin, A.; Nestel, S.; von Bubnoff, N.; Schultze-Seemann, W.; Popp, J.; Nazarenko, I. A Specific Spectral Signature of Serum and Plasma-Derived Extracellular Vesicles for Cancer Screening. *Nanomedicine Nanotechnol. Biol. Med.* **2017**, *13*, 835–841, doi:10.1016/j.nano.2016.11.016.

220. Lee, C.; Carney, R.P.; Hazari, S.; Smith, Z.J.; Knudson, A.; Robertson, C.S.; Lam, K.S.; Wachsmann-Hogiu, S. 3D Plasmonic Nanobowl Platform for the Study of Exosomes in Solution. *Nanoscale* **2015**, *7*, 9290–9297, doi:10.1039/c5nr01333j.

221. Gualerzi, A.; Kooijmans, S.A.A.; Niada, S.; Picciolini, S.; Brini, A.T.; Camussi, G.; Bedoni, M. Raman Spectroscopy as a Quick Tool to Assess Purity of Extracellular Vesicle Preparations and Predict Their Functionality. *J. Extracell. Vesicles* **2019**, *8*, doi:10.1080/20013078.2019.1568780.

222. Czamara, K.; Majzner, K.; Pacia, M.Z.; Kochan, K.; Kaczor, A.; Baranska, M. Raman Spectroscopy of Lipids: A Review. *J. Raman Spectrosc.* **2015**, *46*, 4–20, doi:10.1002/jrs.4607.

223. Stone, N.; Kendall, C.; Smith, J.; Crow, P.; Barr, H. Raman Spectroscopy for Identification of Epithelial Cancers. *Faraday Discuss.* **2004**, *126*, 141–157, doi:10.1039/b304992b.

224. Notingher, I.; Verrier, S.; Haque, S.; Polak, J.M.; Hench, L.L. Spectroscopic Study of Human Lung Epithelial Cells (A549) in Culture: Living Cells versus Dead Cells. *Biopolymers* **2003**, *72*, 230–240, doi:10.1002/bip.10378.

225. Richter, M.; Hedegaard, M.; Deckert-Gaudig, T.; Lampen, P.; Deckert, V. Laterally Resolved and Direct Spectroscopic Evidence of Nanometer-Sized Lipid and Protein Domains on a Single Cell. *Small* **2011**, *7*, 209–214, doi:10.1002/smll.201001503.

226. Takeuchi, H. Raman Structural Markers of Tryptophan and Histidine Side Chains in Proteins. *Biopolym. - Biospectroscopy Sect.* **2003**, *72*, 305–317, doi:10.1002/bip.10440.

227. Harada, I.; Miura, T.; Takeuchi, H. Origin of the Doublet at 1360 and 1340 Cm-1 in the Raman Spectra of Tryptophan and Related Compounds. *Spectrochim. Acta Part Mol. Spectrosc.* **1986**, *42*, 307–312, doi:10.1016/0584-8539(86)80193-3.

228. Enciso-Martinez, A.; Van Der Pol, E.; Hau, C.M.; Nieuwland, R.; Van Leeuwen, T.G.; Terstappen, L.W.M.M.; Otto, C. Label-Free Identification and Chemical Characterisation of Single Extracellular Vesicles and Lipoproteins by Synchronous Rayleigh and Raman Scattering. *J. Extracell. Vesicles* **2020**, *9*, doi:10.1080/20013078.2020.1730134.

229. Mohammadi, M.R.; Malkovskiy, A.V.; Jothimuthu, P.; Kim, K.M.; Parekh, M.; Inayathullah, M.; Zhuge, Y.; Rajadas, J. PEG/Dextran Double Layer Influences Fe Ion Release and Colloidal Stability of Iron Oxide Nanoparticles. *Sci. Rep.* **2018**, *8*, 1–11, doi:10.1038/s41598-018-22644-8.

230. Koenig, L.; Angood, A.C. Spectra of Poly(Ethy1ene Glycols) in Solution. *J. Polym. Sci. Part -2* **1970**, *8*, 1787–1796.

231. Zhbankov, R.G.; Andrianov, V.M.; Marchewka, M.K. Fourier Transform IR and Raman Spectroscopy and Structure of Carbohydrates. *J. Mol. Struct.* **1997**, *436–437*, 637–654, doi:10.1016/S0022-2860(97)00141-5.

232. Siew, D.C.W.; Cooney, R.P.; Taylor, M.J.; Wiggins, P.M. Vibrational Spectroscopic Studies of Aqueous Dextran Sulphate. *J. Raman Spectrosc.* **1994**, *25*, 727–733, doi:10.1002/jrs.1250250737.

233. Nielsen, A.S.; Batchelder, D.N.; Pyrz, R. Estimation of Crystallinity of Isotactic Polypropylene Using Raman Spectroscopy. *Polymer* **2002**, *43*, 2671–2676, doi:10.1016/S0032-3861(02)00053-8.

234. Tadokoro, H.; Kobayashi, M.; Ukita, M.; Yasufuku, K.; Murahashi, S.; Torii, T. Normal Vibrations of the Polymer Molecules of Helical Conformation. V. Isotactic Polypropylene and Its Deuteroderivatives. *J. Chem. Phys.* **1965**, *42*, 1432–1449, doi:10.1063/1.1696134.